W URSAE MAJORIS VARIABLES FROM THE NORTHERN SKY VARIABILITY SURVEY

A THESIS

SUBMITTED TO THE GRADUATE SCHOOL

IN PARTIAL FULFILLMENT OF THE REQUIREMENTS

FOR THE DEGREE

MASTER OF SCIENCE

BY

ALAN A. GAVEL II

ADVISOR: DR. ROBERT C. BERRINGTON

BALL STATE UNIVERSITY

MUNCIE, INDIANA

DECEMBER 2018

For

Sidney and Lucy

with love

Contents

List of Figures

List of Tables

Acknowledgments

I would like to thank the Indiana Space Grant Consortium for awarding me a grant in support of this investigation.

This thesis makes use of the data from the Northern Sky Variability Survey created jointly by the Los Alamos National Laboratory and University of Michigan. The NSVS was funded by the Department of Energy, the National Aeronautics and Space Administration, and the National Science Foundation.

This research has made use of the SIMBAD database, operated at CDS, Strasbourg, France.

IRAF is distributed by the National Optical Astronomy Observatories, which are operated by the Association of Universities for Research in Astronomy, Inc., under cooperative agreement with the National Science Foundation.

I would like to thank Dr. Cecilia Barnbaum for her continued advice and support. Without it, my rewarding experience at Ball State University would not have transpired.

I would like to thank Dr. Thomas Jordan for giving me the opportunity to succeed at Ball State University and for granting me a Graduate Teaching Assistanceship.

I would like to thank Dr. Robert C. Berrington for investing extraordinary time and effort into my development and success as an astronomer.

I would like to thank Jessy and Krista Watson for their generous hospitality and friendship during my stay in Muncie, Indiana.

I would like to thank my father, Alan A. Gavel, for his continued support.

Abstract

This study presents the investigation and modeling of two W Ursae Majoris binary systems: NSVS 3971593 and NSVS 7680691. Both were selected from the Northern Sky Variability Survey. Observations in three band-pass filters, Johnson B, Johnson V and Cousins R were completed using the 0.4 meter and 0.5 meter telescopes at the Cooper Science Observatory located on the Ball State University campus in Muncie, Indiana. The Image Reduction and Analysis Facility (IRAF) software was used to reduce photometric data and to perform differential aperture photometry. Light curves generated by IRAF were analyzed by the PERANSO software and by the PDM task in IRAF to determine the orbital period of each binary system. Finally, other orbital parameters of the binary systems were established using the PHOEBE software which implements the Wilson-Devinney code.

Chapter 1

Introduction

1.1 Binary Star Systems

Binary stars are the most excellent naturally occurring astronomy experiments. They are a major source of our fundamental knowledge of stars. A binary star is a system of two stars that orbit about a mutual center of mass. It is estimated that over half of the stars in the sky belong to binary systems or multiple star systems. Most of these systems are wide binaries, the separation between the stars is such that besides being gravitationally bound, the stars have little influence on each other. Close binary systems are those in which the separation between the stars is comparable to their size. Because of the wealth of astrophysics involved in the study of the interaction between stellar components of these systems, they are of particular interest. In close binary systems, the outer layers of a star can be deformed by the gravity of its companion. In some cases, stellar material is transferred from one star to the other which can complicate the stellar evolution of the pair. If their separation is sufficiently small, the elongated stars of a close binary system may be in contact with each other, that is, they may share a common envelope. I have selected two such binary systems from the Northern Sky Variability Survey (NSVS) (Woźniak 2004) for investigation: NSVS 3971593 and NSVS 7680691. The selected binary systems are not visual binaries; the

individual stellar components are too close together to be resolved independently. Instead, each binary system is observed as a singular point of light. Orbital parameters of the binary systems are established from computational analysis of optical variability data obtained in three band-pass filters, Johnson B, Johnson V and Cousins R (R_C).

1.1.1 Orbital Parameters

The stellar components of a binary system, M_1 and M_2 are treated as point masses orbiting about their mutual center of mass. Their motion is confined to the orbital plane. The angle that the rotation axis makes with the line of sight to the earth is i, the *inclination* (see Figure 1.1). If the distance between M_1 and M_2 and the period of their orbit are known, the total mass of the system can be determined directly via Kepler's Harmonic law

$$P^2 = \frac{4\pi^2}{G(M_1 + M_2)} a^3, \tag{1.1}$$

where P is the orbital period, a is the semi-major axis (the component separation) and G is the gravitational constant (Carroll & Ostlie 2007). The brightness of a star or binary system is measured in terms of radiant flux. It is dependent on the star's distance from Earth and the rate at which it radiates energy. A star's *luminosity* L is the amount of energy it radiates every second. The *effective surface temperature* T_{eff} and the *surface flux* F_{surf} of a star is defined by a star's luminosity (Carroll & Ostlie 2007).

$$L = A\sigma T_{\text{eff}}^4 = AF_{\text{surf}}, \tag{1.2}$$

where A is the surface area of the star and σ is the Stephan-Boltzmann constant.

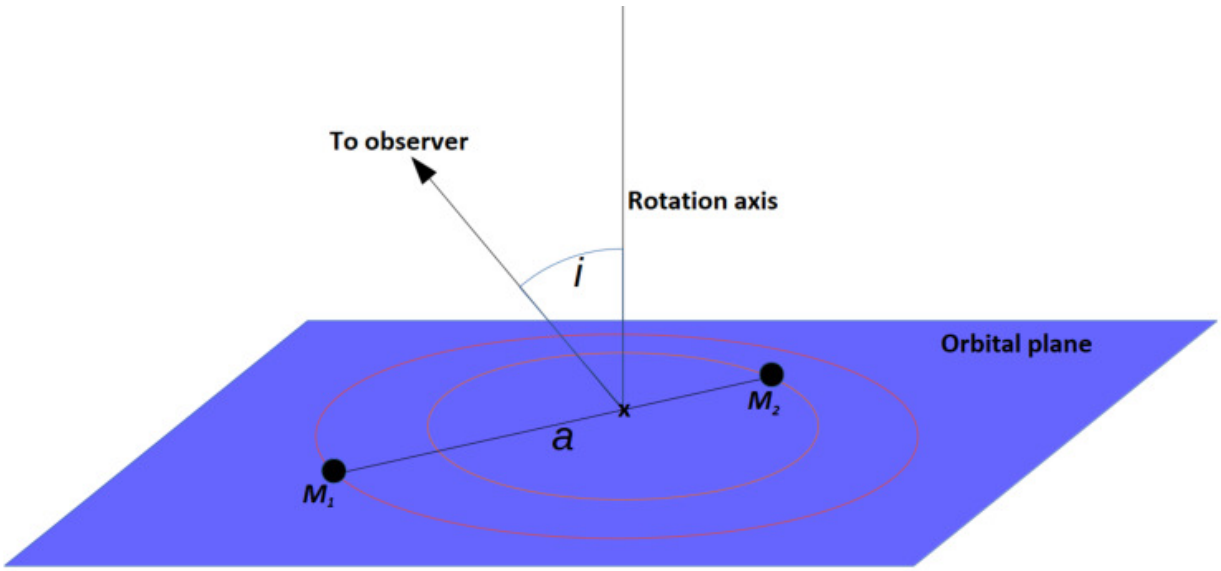

Figure 1.1: Point masses M_1 and M_2 orbit in the orbital plane about their mutual center of mass (marked with an 'x'). The angle the rotation axis makes with the line of sight to the observer is the inclination i. The distance between the two point masses is the semi-major axis a.

1.2 Eclipsing Binary Systems

For binary systems that have orbital planes oriented approximately along the line of sight of the observer, one star may periodically pass in front of the other, blocking the light of the eclipsed component (Carroll & Ostlie 2007). An inclination of $i = 90°$ describes a binary star configuration in which the center of one star passes directly in front of the center of the other star during an eclipse. Eclipses cause variability in the apparent brightness of the system. Stars that display a change in apparent brightness over a period of time are known as variable stars. Classification of variable stars is based on the type of mechanism causing the variability. Classically, variable stars are grouped into three categories: eruptive, pulsating and geometric. The modern arrangement is dyadic; variable stars are either intrinsic or extrinsic. Eruptive stars and pulsating stars are considered intrinsic because the variability observed in these systems is caused by some physical behavior on the inside or surface of the star. Geometric variables are extrinsic. They are either an eclipsing binary system (EB) or a rotating variable star. An extrinsic variable varies because the viewable portion of the

star changes with time (Kallrath & Milone 2009).

1.2.1 Light Curves

Observations on variable stars are made by measuring their brightness as a time-dependent flux. The plot of a star's brightness versus time is known as a *light curve*. Phenomenological classification of variable stars is based on the shape of the light curve observed. Each class is defined by observations of a variable star prototype. There are three major categories of EBs. The prototypes are Algol, β Lyrae and W Ursae Majoris and according to some schemes, the light curve classes are known as EA, EB and EW, respectively. Light curves generated from close binary systems are periodic; the cycle of variation repeats relatively reliably (Kallrath & Milone 2009). This cycle corresponds to the orbital period of the binary system. The fractional part of the period through which time has advanced is known as the *orbital phase* (see Figure 4.3). It is advantageous to represent a light curve as a function of brightness versus orbital phase rather than as a function of brightness versus time. Orbital phase indicates the relative position of the component stars; repeated positions have the same orbital phase. There are two eclipses for each orbital period and each eclipse corresponds to a particular minimum in the observed light curve of the binary system. The *Primary Eclipse* occurs when the hotter of the two stars is being blocked from view. The *Secondary Eclipse* occurs when the hotter star eclipses the other. The difference in brightness between the two stars is proportional to the difference in depth between the two minima. The Primary Eclipse has the deeper minimum. The orbital phase is measured from the primary eclipse. Its value ranges from zero to one.

Binary systems that have EA type light curves are characterized by the star β Persei, also known as Algol. The duration of the primary and secondary eclipse is short compared to the orbital period; the flux observed from these systems is relatively constant. Thus, the light curves are nearly flat on top. Figure 1.3 shows a synthetic EA type light curve. The light curve may rise near the secondary minimum, indicating a *reflection effect*, actually a

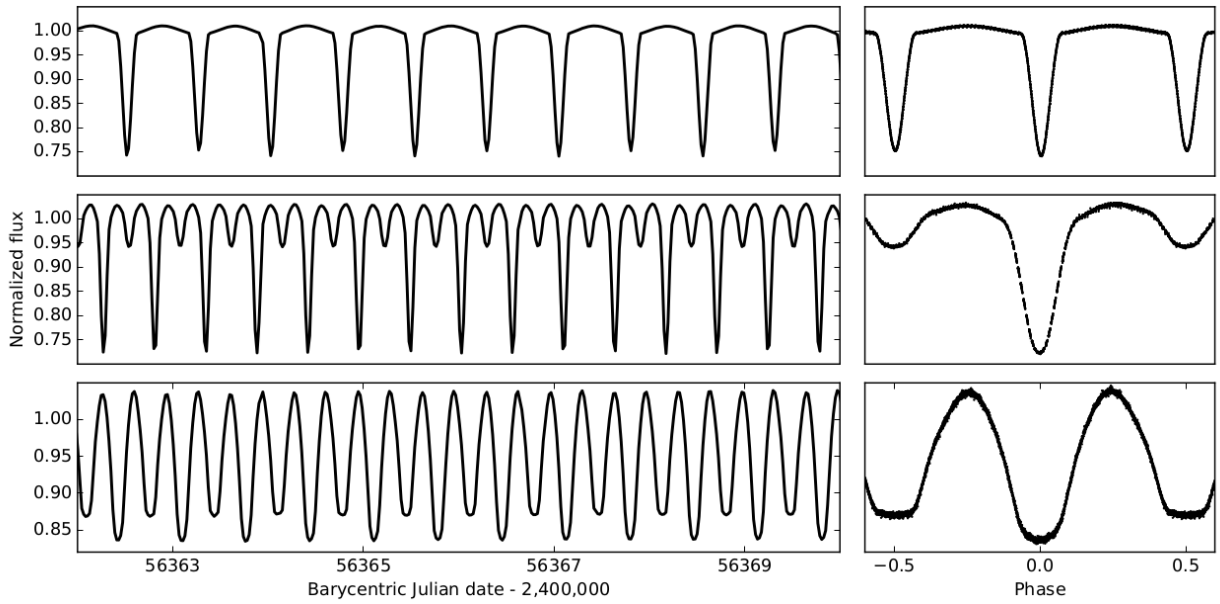

Figure 1.2: Normalized flux as a function of time (*left*) and as a function of phase (*right*) of (*top panel*) *EA* type binary system KIC 5513861 (P=1.51 days), (*middle panel*) *EB* type binary system KIC 8074045 (P=0.54 days) and (*bottom panel*) *EW* type binary system KIC 3127873 (P=0.67 days) (Prša *et al.* 2016).

reprocessing of the hotter stars' radiation as it impinges on the atmosphere of its companion, increasing the cooler star's luminosity in the irradiated area (Kallrath & Milone 2009). Algol is visible to the unaided eye and was one of the first variable stars discovered. Its curious behavior was recognized in ancient Greece; Homer wrote of "the Demon Star" in his epic, *the Iliad* (Reynolds 2005). W Ursae Majoris binary systems have *EW* type light curves and β Lyrae binary systems have *EB* type light curves. Both types are continuously variable and have round tops. Distinction is made by comparing the depths of primary and secondary minima. The depths of the minima in an *EW* type light curve are nearly the same while in *EB* types they are not. For these systems, the viewable portion of the surface is continuously changing. Figure 1.4 shows a *EB* type light curve and Figure 1.5 shows an *EW* type light curve.

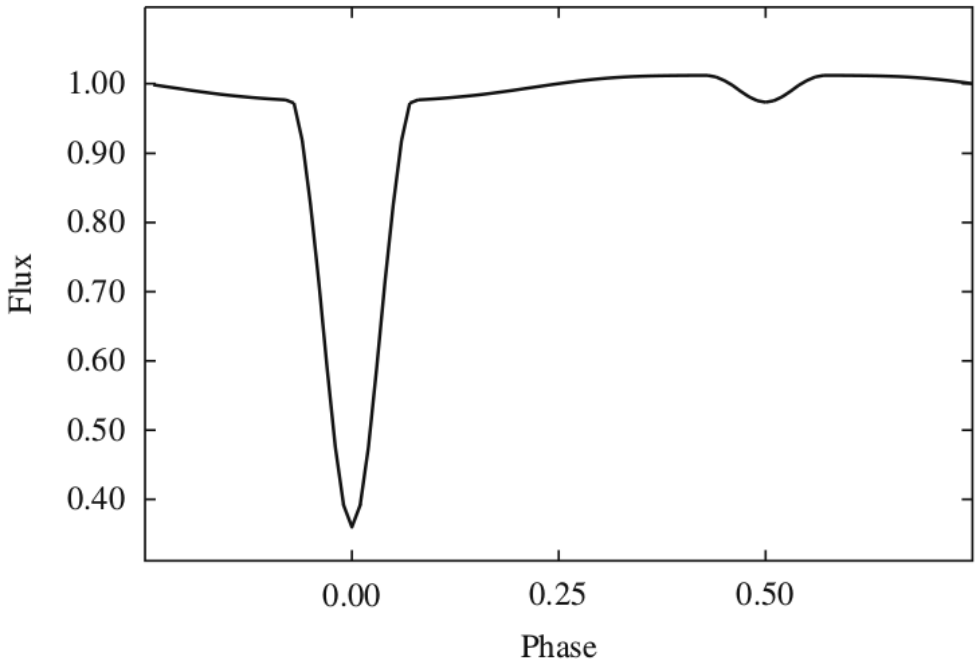

Figure 1.3: Synthetic EA type light curve. Plot was produced using the parameter file *algolv.bmd* from the BINARY MAKER 2.0 examples collection (Bradstreet 1993). The reflection effect can be seen around the secondary minimum.

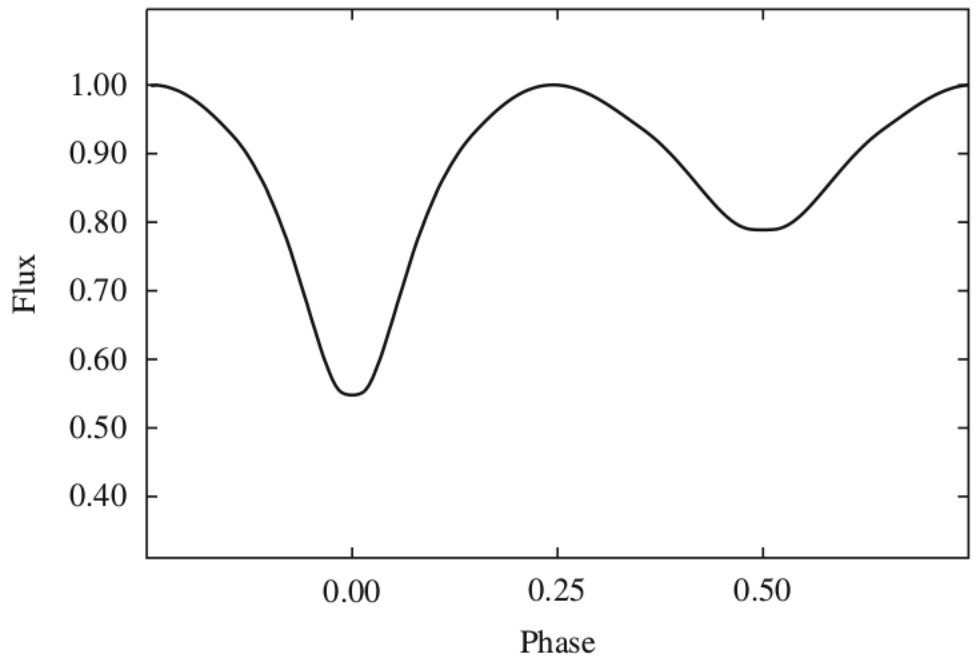

Figure 1.4: Synthetic EB type light curve. Plot was produced with BINARY MAKER (Bradstreet 1993) using the parameters for *RU Ursae Minoris* given in the *Pictorial Atlas* (Terrell et al. 1992).

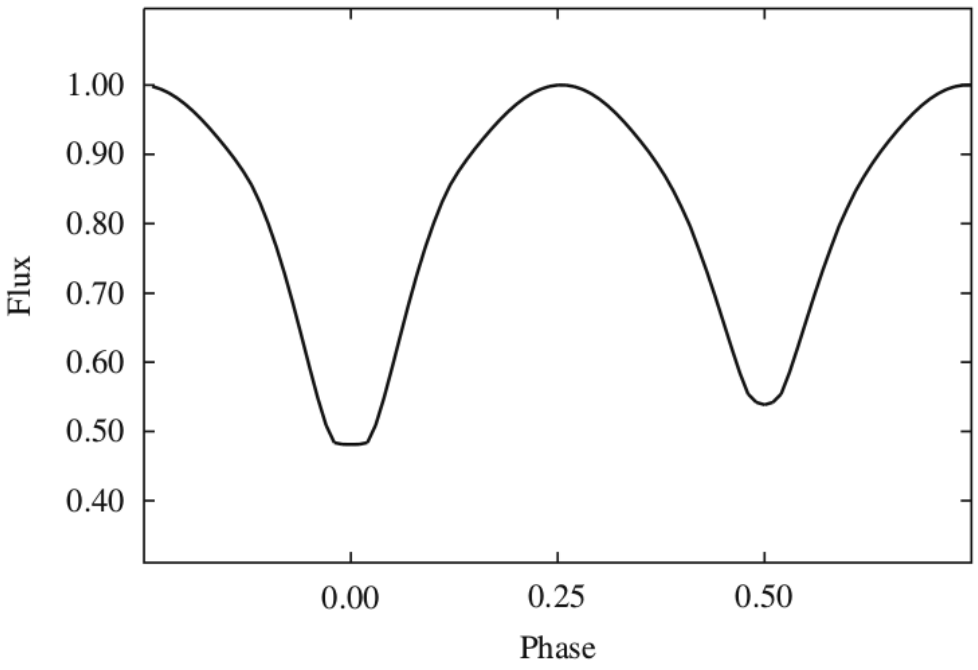

Figure 1.5: Synthetic EW type light curve. Plot was produced using the parameter file *abandb.bmd* from the BINARY MAKER 2.0 examples collection (Bradstreet 1993).

1.3 Morphology of Binary Systems

The classification scheme of EBs is twofold. While phenomenological classes are based on observations, morphological classification is based on theory that provides a visualization of the form and structure of a binary system. Stars in a close binary system with a separation roughly equal to the diameter of the larger star may have their outer layers gravitationally deformed into a teardrop shape (Carroll & Ostlie 2007). Stellar surfaces are calculated with Roche geometry, a theory that considers what forces are acting on the distribution of mass in a binary system.

1.3.1 Roche Geometry

Tidal forces between the two stellar components of EBs tend to produce circular orbits (Kallrath & Milone 2009). The distribution of stellar mass in the system is governed by only two forces: the gravitational attraction between the two components and the centrifugal force

of the system orbiting about its center of mass. The co-rotating frame is a reference frame in which the distribution of stellar mass is static. Nineteenth century French mathematician, Edouard Roche, devised a way to describe this distribution. Roche utilized the concept of equipotential surfaces. These are surfaces on which the *effective gravitational potential*, the sum of rotational and gravitational potential energy per unit mass, is constant (Kallrath & Milone 2009). The surface of a star is described by an equipotential surface. Its effective gravitational potential is Ω, the *surface potential*. The equation that defines the effective gravitational potential can be written in a form that is independent of the absolute sizes and masses of the individual stellar components by using the semi-major axis a as the unit of distance. Consider the following example with two stars of a binary system in a circular orbit. Let M_1 and M_2 be point masses representing the center of mass of each component. Their orbital motion is confined to the xy plane and they maintain a separation $a = a_1 + a_2$ (see Figure 1.6). Placing M_1 at the origin and M_2 at the point $(x = 1, y = 0, z = 0)$ in the co-rotating frame sets the semi-major axis $a = 1$ and the location of the center of mass of the system at $(x = a_1, y = 0)$. The axis of rotation intersects the orbital plane at the center of mass such that

$$M_1 a_1 = M_2 a_2. \tag{1.3}$$

With $G(M_1 + M_2)/a$ as the unit of energy, the effective gravitational potential at the point (x, y, z) in the co-rotating (rest) frame of the system is given by

$$\Omega = \frac{2}{(1+q)r_1} + \frac{2q}{(1+q)r_2} + p^2, \tag{1.4}$$

where r_1 is the distance from the M_1, r_2 is the distance from M_2, p is the perpendicular distance from the axis of rotation and q is the mass ratio (Lucy 1967).

$$q = \frac{M_2}{M_1} \tag{1.5}$$

and the distances r_1 and r_2 are

$$r_1^2 = x^2 + y^2 + z^2 \tag{1.6}$$

and

$$r_2^2 = (x-1)^2 + y^2 + z^2. \tag{1.7}$$

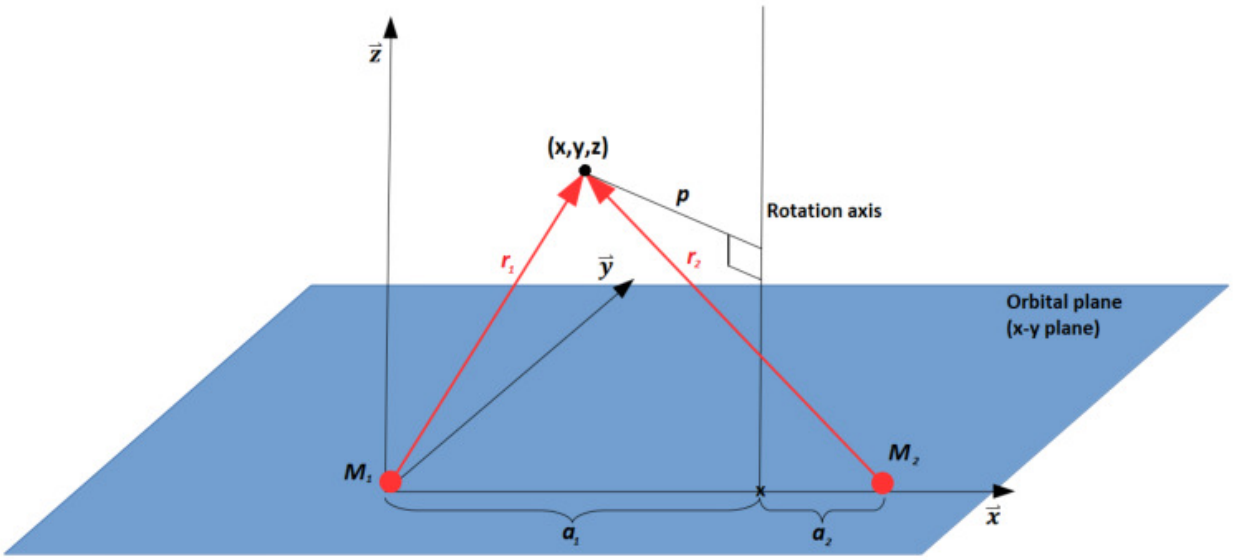

Figure 1.6: The effective potential Ω at the point (x, y, z) is determined with Equation 1.9. Points in space that have the same effective potential form an equipotential surface. The stellar surface is modeled with an equipotential surface.

Substituting $(a_2 = 1 - a_1)$ then combining Equation 1.3 and Equation 1.5, the length a_1 can be solved in terms of q (see Figure 1.7). The perpendicular distance from the axis of rotation is determined from the Pythagoras relation

$$p = \sqrt{[x - \frac{q}{(1+q)}]^2 + y^2}, \tag{1.8}$$

which makes Ω a function of position and mass ratio q.

$$\Omega = \frac{2}{(1+q)r_1} + \frac{2q}{(1+q)r_2} + [x - \frac{q}{(1+q)}]^2 + y^2. \tag{1.9}$$

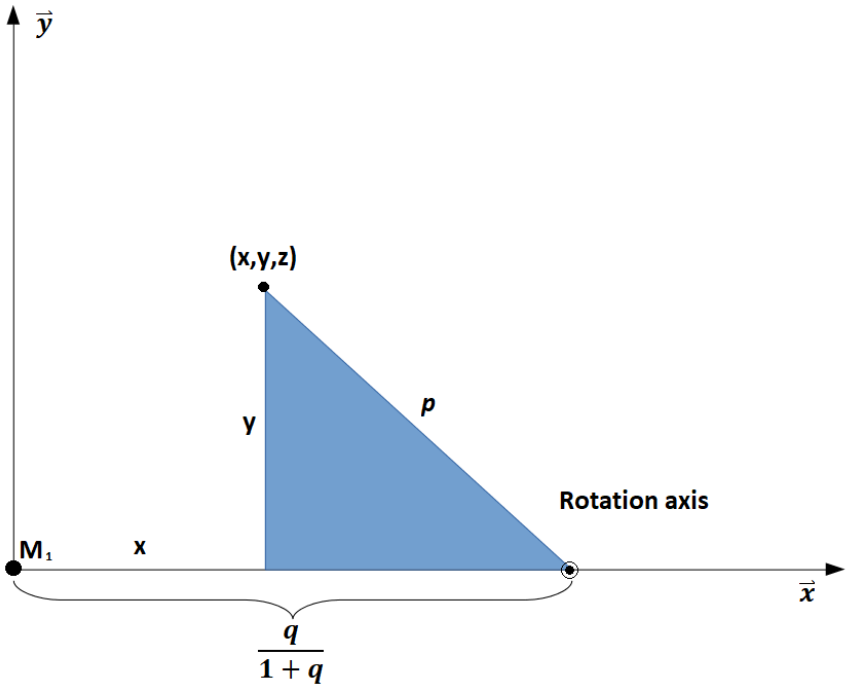

Figure 1.7: The length a_1 from Figure 1.6 is the distance from M_1 to the axis of rotation. It can be solved in terms of the mass ratio q. The perpendicular distance p from the axis of rotation to the point (x, y, z) is determined with Equation 1.8.

Points in space that have the same effective gravitational potential form an equipotential surface. Equipotential surfaces are *level* surfaces, i.e., the sum of the gravitational and centrifugal forces is directed perpendicularly to these surfaces. A test mass m (a theoretical particle that experiences the forces present in the system without influencing the system) located at the point (x, y, z) experiences a net force with magnitude given by the gradient

$$F = -m\nabla\Omega. \tag{1.10}$$

There are five locations in the co-rotating frame of the binary system where the force on a test mass, initially at rest, experiences no net force ($\nabla\Omega = 0$). The gravitational force on the test mass due to the masses of the stellar components is balanced by the centrifugal force.

These locations of unstable equilibrium (Carroll & Ostlie 2007) are shown situated about the stellar components of the binary system in Figure 1.8. The locations are named after the nineteenth century French mathematician who discovered them, Joseph-Louis Lagrange, and they are numbered from L1 to L5. Lagrange points L1, L2 and L3 are situated in the orbital plane on the axis that connects the centers of mass of each stellar component. *Equipotential contours*, intersections of equipotential surfaces with the orbital plane, provide a two-dimensional representation of equipotential surfaces. Figure 1.8 shows several contours including the ones that pass through the L1, L2 and L3 Lagrange points. Equipotential surfaces that are close to either stellar component are spherical shapes centered on the component. Moving away from a stellar component, the surfaces become larger, distorting into teardrop shapes. The teardrop shapes eventually become large enough so that they touch at the inner Lagrange point. The inner Lagrange point, L1, is situated in between the stellar components of a binary system. The equipotential surface that passes through this Lagrange point defines two *Roche lobes*. Each Roche lobe envelopes one of the stellar components. The equipotential surface that passes through L1 is the largest equipotential surface to envelope the stellar components independently and is called the inner Lagrangian surface Ω_I (Kallrath & Milone 2009). The the relative sizes of the two volumes of space inscribed by the inner Lagrangian surface, the Roche lobes, are determined by the mass ratio q (Kallrath & Milone 2009). The more massive star has the larger Roche lobe. The equipotential surface that passes through the Lagrange point L2 is also shown in Figure 1.8. It is called the outer Lagrangian surface Ω_O. The volume of space inscribed by the outer Lagrangian surface has a dumbbell shape. Morphological representations of W UMa type variable stars possess this dumbbell shape.

1.3.2 Detached and Semi-detached Binary Systems

Morphological classification of a binary system is based on the extent to which the mass of each stellar component fills its respective Roche lobe. Wide binary systems are *de-*

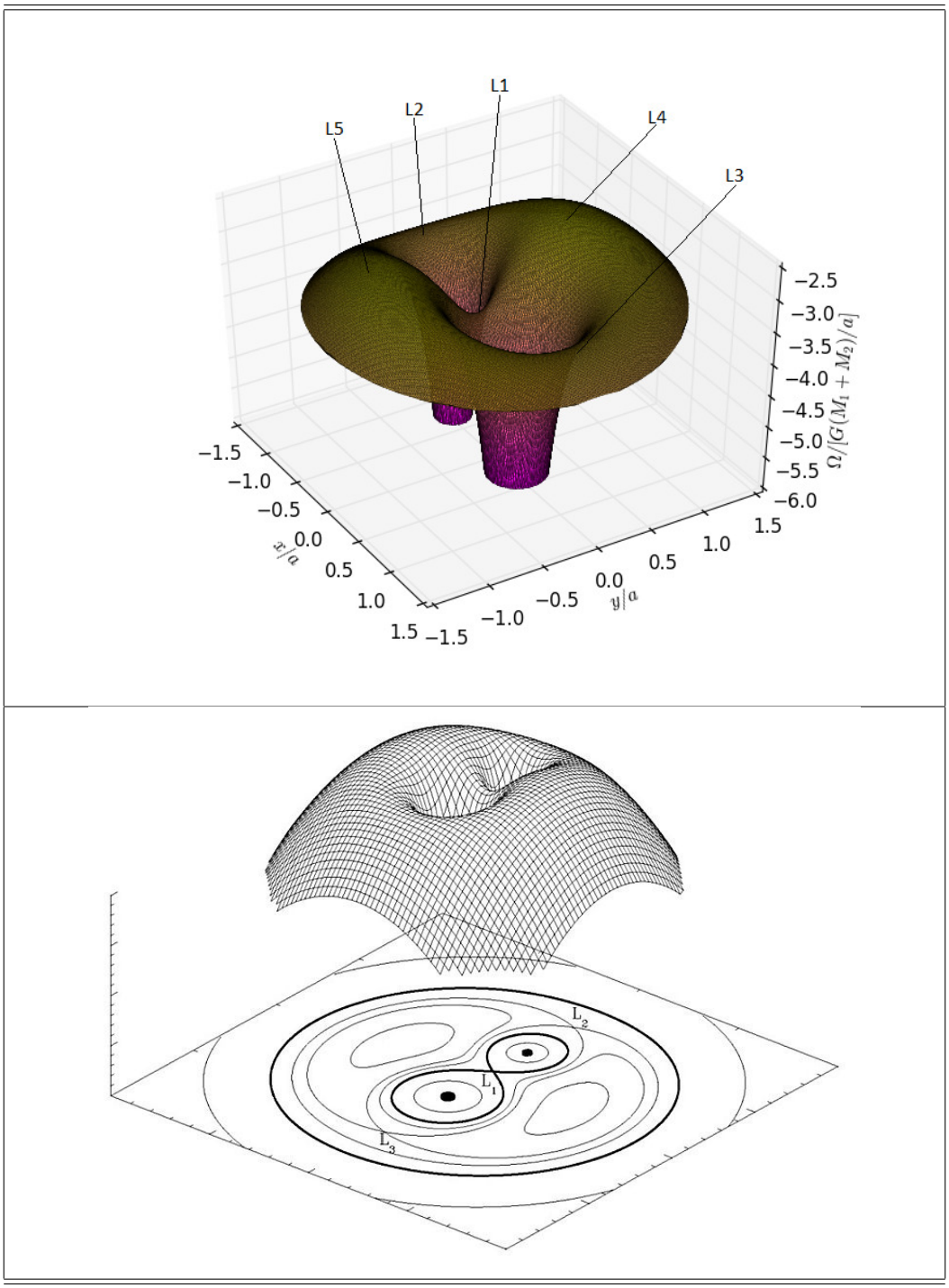

Figure 1.8: (*top*) Effective gravitational potential in the xy-plane for a binary star with mass ratio $q = 2$. The binary's center of mass is at the origin. Lagrange points L1, L2 and L3 are situated on the x-axis. Lagrange points L4 and L5 form equilateral triangles with the positions of the stellar components. (*bottom*) Several Roche surfaces projected on to the orbital plane. L1, L2 and L3 Lagrange points are indicated (van der Sluys 2006).

tached binary systems; neither star fills its Roche lobe. Figure 1.9 shows the inner Lagrangian Ω_I and outer Lagrangian Ω_O surfaces of a detached binary system. The corresponding shapes of the stellar components are nearly spherical. Close binary systems are also defined as those systems in which a stellar component fills its Roche lobe at some stage in its evolution (Plavec 1968). To illustrate the situation in which a stellar component fills its Roche lobe consider the effective gravitational potential of a binary system plotted in Figure 1.10. It is a slice of Figure 1.8 (*top panel*) along the x-axis, the axis that joins the centers of mass of the stellar components. It shows potential energy barriers corresponding to L1 and L2. An analogy is to picture these energy barriers as physical objects that hold a liquid. Figure 1.10 shows that the potential well of the star located at $x = 0$ holds its maximum amount of liquid; any additional liquid would spill over the L1 barrier into the potential well of the other star. This depicts the situation where one star fills its Roche lobe while the other does not. Such a system is called a *semi-detached binary*. Mass of the star that has filled its Roche lobe with energy greater than Ω_I can escape from the potential well of the star. It may transfer to the other star. Stellar mass with energy greater than Ω_O can escape the binary system altogether through the L2 Lagrange point. Figure 1.11 shows the inner Lagrangian Ω_I and outer Lagrangian Ω_O surfaces of a semi-detached binary system. The corresponding shape of the component star that has filled its Roche lobe has a teardrop shape defined by its Roche surface.

1.3.3 Over-Contact Binary Systems

A stellar component of a binary system that exactly fills its Roche lobe is said to be in contact with its Roche lobe. If both component stars overfill their respective Roche lobe the system is an *over-contact binary*. For this system, the component stars are also in contact with each other. This contact region is centered about the inner Lagrangian point L1. These systems have a common stellar envelope, a singular dumbbell shaped outer surface defined by the effective gravitational potential Ω, where $\Omega_I \leq \Omega \leq \Omega_O$. For the

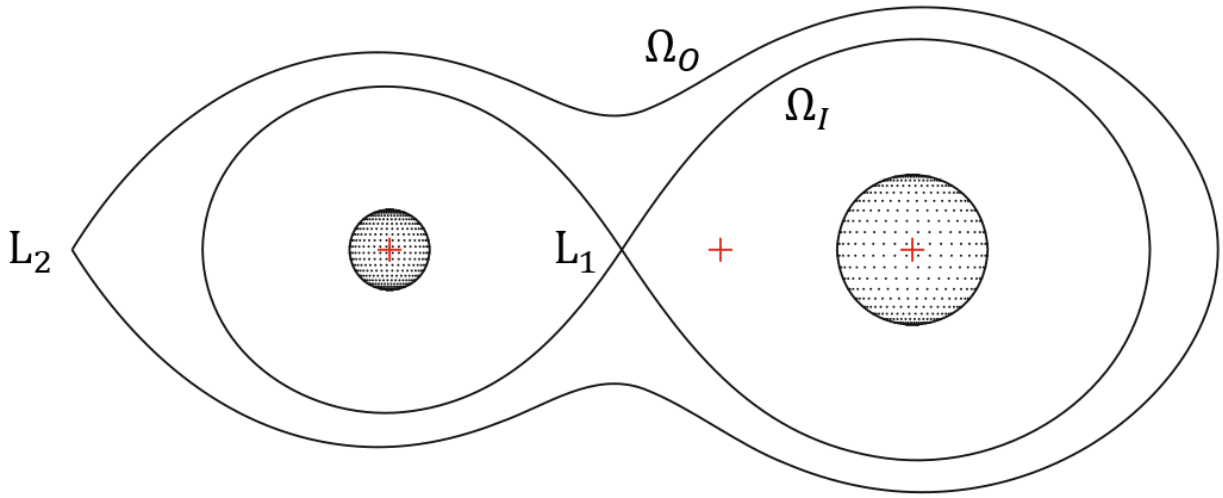

Figure 1.9: Detached System: Roche Surfaces with corresponding shapes of composite stars. The Inner Lagrangian Ω_I surface is the largest equipotential surface to envelope the stellar components independently and passes through L1. The Outer Lagrangian Ω_O surface passes through L2. The center of mass for the binary system is labeled with the center plus sign. Image produced with `Binary Maker 2.0` (Bradstreet 2005).

case of circular orbits, the degree of contact can be quantitatively described by the contact parameter f or *fill-out factor* given by Equation 1.11 (Kallrath & Milone 2009). If $\Omega = \Omega_I$ then the contact parameter $f = 0$ and both stellar components fill their Roche lobe. f can be as high as 1 when $\Omega = \Omega_O$. Figure 1.12 shows the shape of an over-contact binary system. Over-contact binary morphology explains *EW* type light curves very well (Kallrath & Milone 2009). Over-contact binary systems are known as W Ursae Majoris (W UMa) type variable stars (Carroll & Ostlie 2007). These systems typically have orbital periods of less than one day. They have spectral classes F, G and K (Henden & Kaitchuck 1982). W UMa stars can be further divided into two types based on temperature differences between stellar components. In *A-type* contact systems, the hotter, brighter star is also more massive than its companion. In *W-type* contact systems, it is less massive (Kallrath & Milone 2009).

$$f = \frac{\Omega - \Omega_I}{\Omega_O - \Omega_I} \tag{1.11}$$

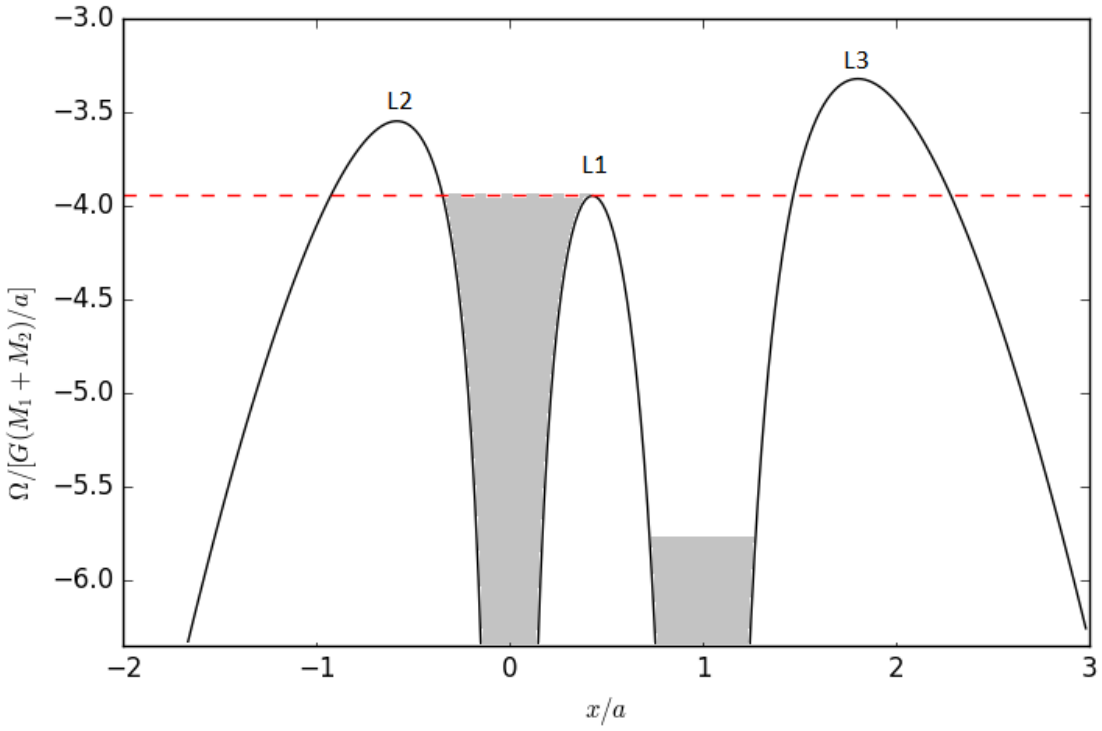

Figure 1.10: The effective gravitational potential along the x-axis, the axis that joins the centers of mass of the two component stars. The stellar component at $x = 0$ has filled its Roche lobe while the stellar component at $x = 1$ has not. Dashed line indicates value of the inner Lagrangian surface Ω_I.

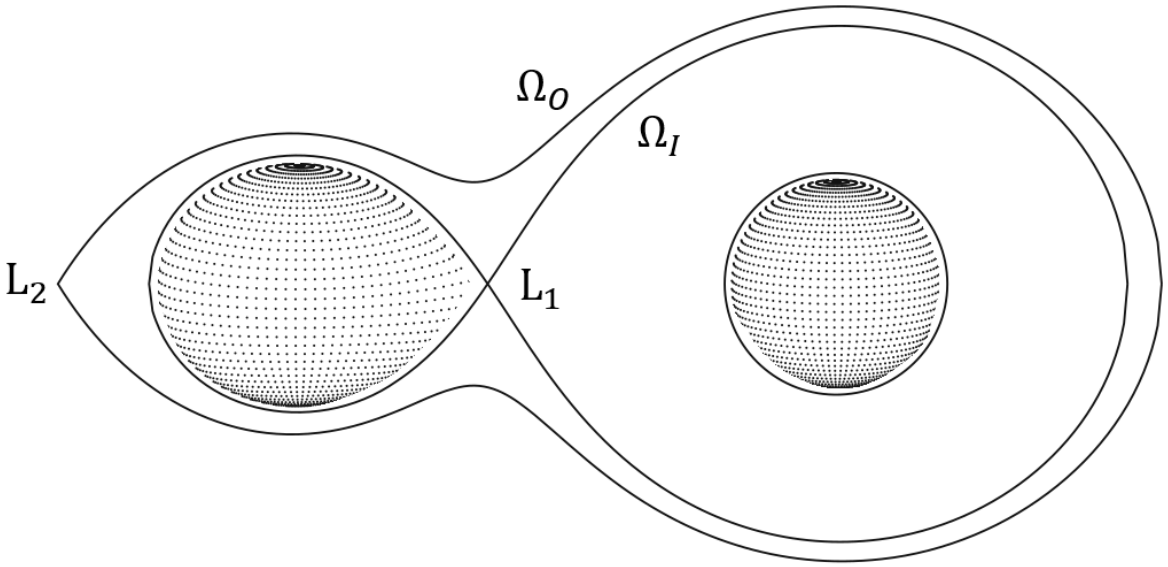

Figure 1.11: Semi-Detached System: Roche Surfaces with corresponding shapes of component stars. The Inner Lagrangian Ω_I surface is the largest equipotential surface to envelope the stellar components independently and passes through L1. The Outer Lagrangian Ω_O surface passes through L2. Star on the left fills its Roche Lobe while its companion does not. Image produced with `Binary Maker` 2.0 (Bradstreet 2005).

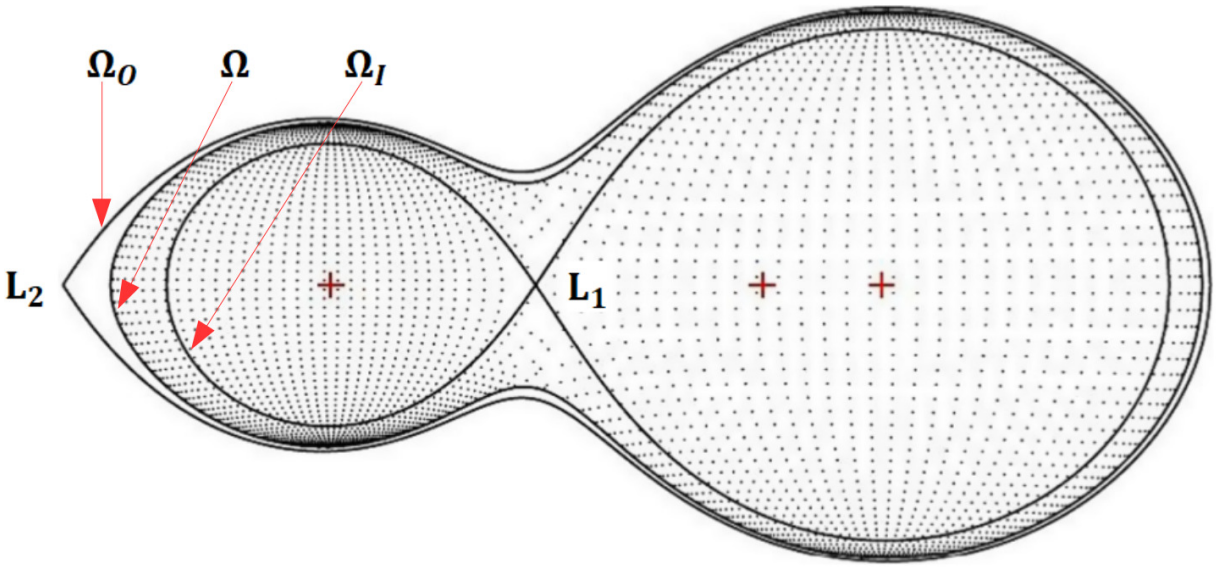

Figure 1.12: Contact System: component stars of a contact system overfill their Roche Lobes and share a common envelope. The result is a dumbbell shaped stellar surface defined by $\Omega_I \leq \Omega \leq \Omega_O$. Ω_O passes through the L2 Lagrangian point and Ω_I passes through the L1 Lagrangian point. Image is a morphological representation of Binary star GSC 1283-53 with contact parameter $f = 0.834$ (Essam *et al.* 2013).

1.4 Modeling of Eclipsing Binary Systems

The study of EBs has a rich history. American astronomer, Edward C. Pickering made an investigation of the orbit of Algol on the basis of its light curve as early as 1880 (Aitken 1935). His model assumed that the two stars are spherical with uniformly illuminated disks and move in circular orbits. Generally, an EB model is capable of generating a synthetic light curve from theoretically determined orbital parameters. The goal of a model is to provide a solution to the *inverse problem*, to determine orbital parameters from observed light curves. The Pickering model evolved with the work of Henry Russell and Zdeněk Kopal to include treating the binary components as ellipsoids and rectification of the observed light curve to remove the effects of variation outside the eclipses (Russell 1946). With the advent of the computational analysis, several programs were written based on the rectifiable model. Around the same time however, the model began to lose favorability. Underlying assumptions made it rarely compatable with reality, espescially for semi-detached and over-contact systems. While the Russell model serves a limited purpose well, it is not suited to improvements which would make it physically more realitsic (Wilson & Devinney 1971). Astronomers developed new models and programs. Lucy (1968) calculated light curves of over-contact systems directly using a single value for the surface potential Ω (see Equation 1.9). The outer layers of the Lucy model for a W UMa system are convective and a first approximation to the appropriate relation between $T_{\rm eff}$ and the local gravity g is (Lucy 1967)

$$T_{\rm eff} \propto g^{\beta}, \tag{1.12}$$

where the coefficient $\beta = 0.08$. The Wilson-Devinney (1971) model is based on Roche geometry. Several orbital parameters such as inclination i, luminosity L, surface potential Ω and mass ratio q are incorporated into the Wilson-Devinney (WD) model. Presently, the WD computer code is the most widely used of all the light curve modeling tools (Kallrath

& Milone 2009).

The PHysics Of Eclipsing BinariEs (PHOEBE) software by Prša & Zwitter (2005) provides a graphical user interface (GUI) to the WD code. The GUI contains several tabs, each dedicated to different apects of the modeling procedure. The four main tabs are data, parameters, fitting and plotting. The modeling process begins by loading observational data into the data section. The data can be light curve data or radial velocity data. Presently, I do not have radial velocity observational data. Once the observational data are loaded, light curves can be displayed in the plotting section. Synthetic light curves can also be displayed. They are generated from values assigned to the orbital parameters in the parameters section. A few values, including orbital period and effective temperature are determined beforehand and are adjusted manually in the parameter section. Values for other parameters are selected in the parameters section and determined numerically in the fitting section. The WD code uses the method of *differential corrections* (Kopal 1943) to converge onto a solution to the inverse problem. The fitting algorithm is executed one iteration at a time. Each iteration produces a set of corrections for the parameters selected for fitting. The corrections and new values are displayed next to the present values. If the new values are reasonable, the parameters are updated and the new values are used for the next iteration. In between iterations, the synthetic and observed light curves can be displayed in the plotting section to monitor the fitting process. The two binary systems I selected from the Northern Sky Variability Survey (NSVS) for investigation were classified by Hoffman *et al.* (2009) as W UMa over-contact binary systems. I use the PHOEBE software package to establish orbital parameters of these systems.

Chapter 2

Data Acquisition

Data acquisition begins with the choice of target stars. The SIMBAD database is accessed via the VizieR Service to locate a catalog of variable stars. Objects populating the catalog were discovered by the Northern Sky Variability Survey (NSVS) (Woźniak 2004). The catalog contains thousands of stars and can be filtered in a search. Specifying an appropriate range of right ascensions and declinations ensures that stars in the search results are viewable for several hours during observation nights. The search results can be organized by several parameters including phenomenological classification and orbital period. Brighter systems are preferred because they require shorter exposure times. Systems with shorter orbital periods are desirable. They require fewer observation nights to cover an entire orbit. If possible, stars with few previous references are selected. Since light curves are generated using differential photometry, it is wise to make sure that there are at least two non-variable stars near the target star. These stars will serve as the comparison star and the check star and must be present in each image frame. Ideally, the magnitudes and radial profiles of the comparison and check stars will be comparable to the variable star and at least one of them should be a Tycho Star (Høg *et al.* 2000).

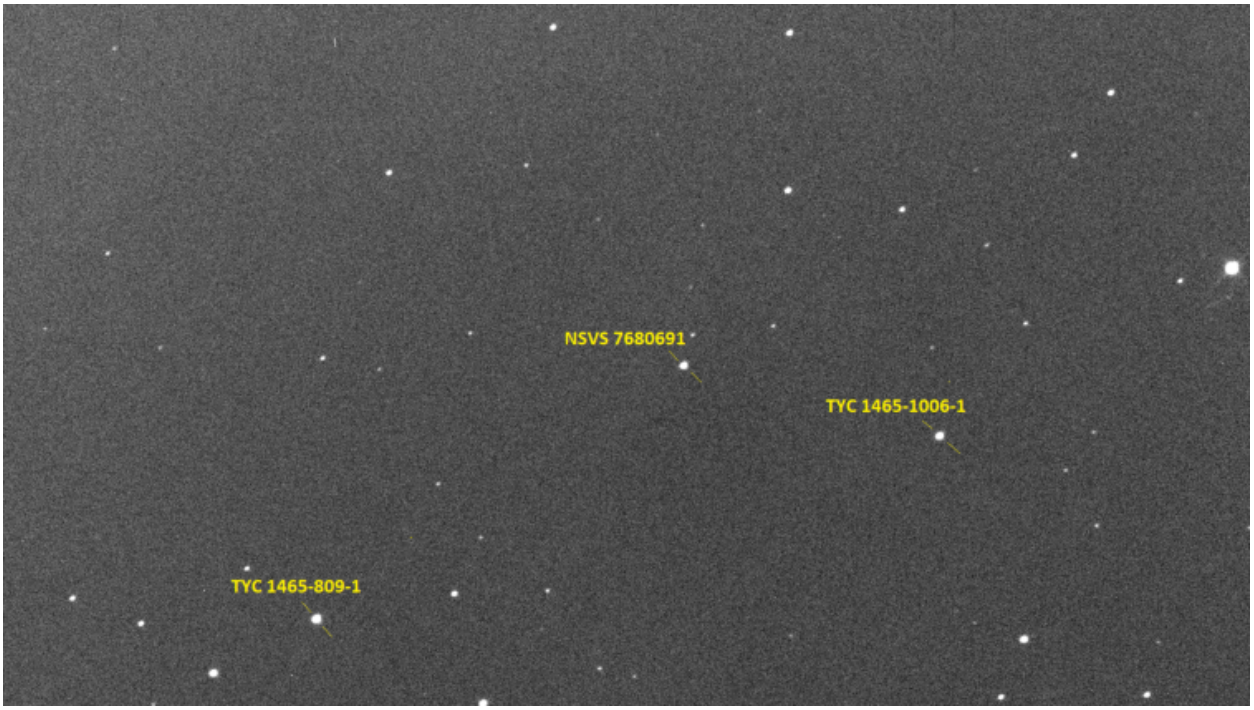

Figure 2.1: Typical image frame including target star NSVS 7680691, the comparison star TYC 1465-809-1 and the check star TYC 1465-1006-1. Image acquired with the 0.5-meter telescope located on the Ball State University (BSU) campus. It is equipped with a Finger Lakes Instrumentation (FLI) PL 16801 CCD camera.

2.1 The Northern Sky Variability Survey

The NSVS was conducted for a full year between 1999 April and 2000 March from Los Alamos, New Mexico (Woźniak 2004). Observing on 275 out of 365 nights, the NSVS compiled an extensive temporal record of photometric data. It contains light curves for over 14 million objects in the optical magnitude range 8 to 15.5 (Woźniak 2004). The data contained in the NSVS was collected by the first-generation Robotic Optical Transient Search Experiment (ROTSE-I). The experiment used a telescope that was fully automatic and consisted of four 200 mm lenses. Its combined field of view was $16^\circ \times 16^\circ$ (Woźniak 2004). The primary objective of the ROTSE-I was to provide a quick response to reports of gamma ray bursts (GRB) from the GRB Coordinate Network (GCN). Since reports of GRB were received approximately once every ten days and each report needed only about an hour to investigate, the ROTSE-I telescope was able to devote most of its observing time to

systematically monitoring the sky (Woźniak 2004). With its large field of view, the ROTSE-I telescope was able to cover the entire local sky twice each observation night (Woźniak 2004). The pair of observations are useful in detecting variability. They also provide a handle on spurious detections due to man-made space objects, cosmic rays, hot pixels and other effects (Woźniak 2004).

From the data contained in the NSVS, several thousand variable stars have been discovered, classified and cataloged (Hoffman *et al.* 2009). Target stars were selected from the 4659 variable objects in the NSVS identified by Hoffman *et al.*. Because there are so many, relatively few have been extensively studied. Also, the large area nature of the survey means the temporal coverage of the stellar systems is course and sporadic. A lengthy baseline of a year is used to generate the light curves, but the lack of the temporal resolution to resolve an individual orbit prevents an extensive photometric study of these systems. By taking several scores of images each observation night I can generate a light curve with a baseline of a few days. Thus, I achieve greater temporal resolution and establish the orbital periods with greater accuracy.

2.2 Observations

All photometric data are taken by a charged coupled device (CCD) that is attached to the telescope. It is a detection device comparable to a camera; the data can be used to create a two dimensional image of the objects being observed. Like a camera, the CCD is fitted with a shutter that can keep its light-detecting components unexposed to light. Janesick & Blouke (1987) compared the operation of a CCD to a field where an array of buckets neatly lined up in rows and columns collect rain water during a rainfall. After the rainfall is over, the amount of rainwater in each bucket is measured giving a two dimensional representation of the rainfall. In a CCD the buckets are called pixels and they do not collect water, they collect light. That is, they collect photons. Ideally, they would only collect photons of

interest, ones that originate from the binary star and other photometry stars being observed through the telescope. But this is not possible, the night sky is not absolutely dark. It has some measure of brightness to it. There are numerous sources of photons that contribute to the sky background of an image. The sources include unresolved astronomical objects, city lights, read noise, thermally generated dark current electrons and actual photons from the sky (Howell 2006). Estimating the brightness of the sky background of an image is important. Pixels that collect photons of interest will also contain photons from the sky background. To measure the brightness of the binary star and other objects in the images, the sky background must be removed.

Both of the targeted stars are W UMa binary systems. Observations on the first target, NSVS 3971593, were conducted from 2015 September to 2015 December. Observations on the second target, NSVS-7680691, were conducted from 2016 March to 2016 April. Table 2.1 lists data given by SIMBAD and Hoffman *et al.* (2009). I observed these stars in three band-pass filters, Johnson (B), Johnson (V) and Cousins (R_C). The observations were conducted using the 0.4-meter and 0.5-meter telescopes at the Cooper Science Observatory located on the Ball State University (BSU) campus. The 0.4-meter telescope is equipped with a Santa Barbara Instruments Group (SBIG) STXL-6303e CCD camera. The 0.5 meter telescope is equipped with a Finger Lakes Instrumentation (FLI) PL 16801 CCD camera. Additional Observatory data are given in Table 2.2.

Parameter	Target 1	Target 2
Identification	NSVS 3971593	NSVS 7680691
Right Ascension (J2000)	$2^h\ 5^m\ 15.87^s$	$13^h\ 37^m\ 12.13^s$
Declination	N $41^\circ\ 28^m\ 13.3^s$	N $21^\circ\ 34^m\ 7.1^s$
Period	0.65552 days	0.31631 days
Amplitude	0.400	0.241

Table 2.1: Coordinate data is from SIMBAD. Orbital periods and light curve amplitudes are reported by Hoffman *et al.* (2009).

Geographical Data				
(Location)	(Latitude)	(Longitude)	(Elevation)	
Muncie, Indiana	40.20°	85.41°	289.56 m	
Telescopes				
(series)	(aperture)	(type)	(mount)	(imaging camera)
Meade LX200	0.4 meter	Schmidt Cassegrain	Fork	SBIG STXL-6303e
Parallax Instruments	0.5 meter	Ritchey-Chrétien		FLI PL16801
Imaging Camera Data				
(Camera)	(Gain)	(Read Noise)	(Filters)	(Telescope)
SBIG STXL-6303E	1.46	12.97	B,V,R	Meade LX200
FLI PL16801	1.40	10.43	B,V,R	Parallax Instruments

Table 2.2: Additional data for the Cooper Science Observatory located on the BSU campus. The 0.4-meter telescope is equipped with a SBIG STXL-6303e CCD camera. The 0.5 meter telescope is equipped with a FLI PL 16801 CCD camera.

The telescopes and CCD cameras are all computer automated, allowing the user to execute a predefined series of exposures. To set up the exposure series the user enters several parameters starting with the coordinates (RA and Dec) of the target star(s). The choice of filters, exposure lengths, binning and the number of times to repeat the series is also entered. The values entered can be saved as a script for the software to execute. I set the script to change filters after every exposure and to use 2×2 binning. Compared to 1×1 binning, this reduces the CCD readout time by a factor of four (Howell 2006) which in turn, increases the temporal resolution of the resulting light curves. The exposure times are different for each filter and they are determined by considering two competing factors: photometry quality and temporal resolution. The target star, comparison star and check star must have a certain level of brightness to be used in photometry. The longer the exposure, the brighter the stars will be in the image and the better the results will be from photometry. However, longer exposures also reduces temporal resolution. The brightness of the selected stars in the image is measured using the CCD camera software. Each target star is observed on multiple nights. Table 2.3 and Table 2.4 lists the observation nights, the number of image frames taken in each bandpass filter for each night and the telescope used. Note that for observation nights April 15^{th} and 16^{th}, I used both telescopes on the same target.

Observation Nights for NSVS 3971593

Date	Number of frames			
	B	V	R_C	TOTAL
September 17, 2015	61	62	62	185
October 15, 2015	57	56	56	169
October 19, 2015	127	127	127	381
November 8, 2015	69	72	71	212
November 9, 2015	93	93	93	279
November 11, 2015	132	148	147	427
November 14, 2015	133	135	134	402
November 15, 2015	70	70	70	210
November 16, 2015	70	70	70	210
December 6, 2015	40	39	37	116

Table 2.3: Observation nights for NSVS 3971593. Filters are Johnson B, Johnson V and Cousins R. All data taken with 0.4m Meade LX200 telescope.

Observation Nights for NSVS 7680691

Date	Number of frames				Telescope
	B	V	R_C	TOTAL	
March 27, 2016	48	48	47	143	0.5m Parallax Instruments
April 14, 2016	28	39	44	111	0.5m Parallax Instruments
April 15, 2016	33	33	18	84	0.4m Meade LX200
April 15, 2016	41	38	39	118	0.5m Parallax Instruments
April 16, 2016	46	34	33	113	0.4m Meade LX200
April 16, 2016	33	33	33	99	0.5m Parallax Instruments
April 17, 2016	49	46	48	143	0.5m Parallax Instruments
April 18, 2016	68	67	67	202	0.5m Parallax Instruments
April 24, 2016	22	36	32	90	0.4m Meade LX200
April 24, 2016	73	73	74	200	0.5m Parallax Instruments

Table 2.4: Observation nights for NSVS 7680691. Filters are Johnson B, Johnson V and Cousins R.

Chapter 3

Data Reduction

3.1 Data Reduction Overview

Before the brightness of an EB can be measured, photometric data must be reduced. The data must be transformed into a standard system so that it will be scientifically useful. The star field images, also called *object frames*, must be calibrated in a standard reduction process to ensure that the results of the photometry are comparable with results from other investigations. The reduction process eliminates unwanted artifacts from the images that were introduced during the acquisition of the data. The Image Reduction and Analysis Facility (IRAF) software (Tody 1993) written by the National Optical Astronomy Observatories (NOAO) is used to complete this task. The reduction process consists of a number of operations that are applied to each image. Special images called calibration frames are made each observation night to complete the reduction process. The calibration frames include 60 bias frames, 6 dark frames and 30 flat frames. Typically, half of these frames are taken at dusk and half are taken at dawn. They are used to reduce the photometric data that is taken on that night.

3.1.1 Bias

The CCD converts its collected photons into electrons via the photoelectric effect. The number of electrons held by each pixel is proportional to the number of photons it collected. Each electron contributes the same amount of electric charge to the total electric charge of a pixel. To determine the number of photons collected by each pixel, the charge of each pixel is read in a process called readout. This process is not perfectly repeatable. If the same pixel is read twice, each time with an identical charge, a slightly different output signal may be produced (Howell 2006). The electronics that perform the readout introduce spurious electrons into the output signal of the readout device. The unwanted fluctuation in the signal due to the readout process is called readout noise. It is usually given as an average number of electrons per pixel introduced into the output signal of the readout device.

A bias frame has an exposure time of zero seconds and the camera shutter remains closed. It is a readout of the unexposed CCD pixels. The bias frames are used to measure the zero level of the CCD output. The 60 bias frames taken on an observation night are averaged together to eliminate read noise variations and random fluctuations. For photometric data taken by the 0.4m Meade LX200 telescope, the mean bias frame is subtracted from all other frames: darks, flats and object frames. The CCD used for the 0.5m telescope generates an overscan strip on each image. The strip consists of a number of rows or columns that do not correspond to physical pixels of the CCD. Like a bias frame, the overscan is used to estimate the zero level of the CCD output. Its advantage is that it is created with each image at the time of readout. It can detect fluctuations in the zero level that occur during the course of an observation night. The overscan of each image is used to set the zero level for that image.

3.1.2 Dark Current

Dark current refers to the spurious electrons that are thermally generated. Any material that is at a temperature above absolute zero will introduce unwanted electrons into the output signal of the readout device. The higher the operating temperature of the CCD

the more unwanted electrons will pollute the output signal. To minimize the dark current the CCD is cooled. On warm nights the operating temperature of the STXL-6303E CCD attached to the 0.4m Meade LX200 telescope could be brought down to $-20°$ Celsius. On cold nights it could be brought down to $-40°$ Celsius.

Like the bias frames, dark frames are made using unexposed CCD pixels. The exposure time is for several minutes. The exposure time should be as long or longer than any object frame exposure time. For this investigation, dark frames are taken with exposure lengths of 10 minutes each. After the bias frame subtraction, the 6 dark frames from each observation night are averaged together. The mean dark frame is subtracted from the flat and object frames.

3.1.3 Flat Fielding

The pixels of a CCD do not respond uniformly to light. There are small differences in quantum efficiency from pixel to pixel and image vignetting and dust shadows are common. To compensate for these variations, several flat field images are taken for each bandpass filter. Each pixel in the flat field image is normalized by dividing its value by the average pixel value. In a flat frame, a pixel that is more sensitive than the average pixel will have a normalized value greater than 1. A pixel that is less sensitive than the average pixel will have a normalized value less than 1. Each pixel in an object frame is divided by the normalized value of the corresponding pixel in a flat frame.

The flat frames are not easily obtained. Ideally, a flat field image is taken with a uniform illumination of the CCD such that every pixel receives equal amounts of light in each bandpass (Howell 2006). Some observatories use an illuminated screen or painted section on the inside of the telescope dome as a source. At the BSU Observatory, flat frames are obtained by taking exposures of the dawn and dusk sky. Five of these *sky flats* are taken at dusk and five are taken at dawn for each filter. The ten sky flats for each filter are averaged together after bias and dark frame subtractions. The mean flat frame of each filter

is used to correct the object frames taken in the corresponding filter. After the flat field correction, the object frames are calibrated and ready for photometry.

3.2 Data Reduction with IRAF

All image reductions are performed using IRAF. The generic CCD reductions package, `ccdred`, which is located in the image reductions package, `imred`, contains the necessary tasks. The primary task is `ccdproc`. It works together with other tasks to process CCD images. Some of theses other tasks are `zerocombine`, `darkcombine` and `flatcombine`.

3.2.1 CCD sections

All images are trimmed in the reduction process. Rows and columns on the edges of the images that do not have useful photometric data (or overscan section data for the 0.5m telescope) are removed. The section of an image that contains useful photometric data is called the data section. The section of an image that contains the overscan is called the bias section. The `implot` task is used to determine the dimensions of these sections. The dimensions of the data section do not change from image to image. Once the dimensions have been determined from one image, they can be used to trim images. The same is true for the bias section for images from the 0.5m telescope. The dimension values are entered as parameters into the image headers. The bias section parameter is called BIASSEC and the data section parameter is called DATASEC.

3.2.2 Image Headers and Task Parameters

CCD images contain information other than pixel values. This extra information is contained in the *image header*. The image header is a long list of data parameters, the values associated with the data parameters and a brief definition of the data parameters. A sample from a typical image header is shown in Appendix A.1. Image headers can be edited.

The values can be changed and additional data parameters can be added to the list. The task `hedit` is used to edit the image header of a single image or to edit the image headers of a list of images. Each task in IRAF contains a list of input parameters. In order for a task to operate it needs to access values from several data parameters in the image headers. An example of adding the parameter DATASEC to a list of image headers is also shown in Appendix A.1. DATASEC is just one of the parameters that need to be added to the headers of the images. Others include RDNOISE, EGAIN and BIASSEC (for 0.6m telescope data).

3.2.3 Instrument Parameters

In the reduction process, at the start of every IRAF session, the first task to execute is `setinstrument`. This sets values that pertain to the instruments used to gather data. The setinstrument parameter list is shown in Appendix A.2. After the instrument and site parameters are set and the setinstrument task is executed, the list of parameters for the task `ccdred` is displayed. These parameters are not adjusted. After executing the ccdred task, the list of parameters for the ccdproc task is displayed. These parameters will be adjusted several times during the reduction process but the ccdproc task will not be used on object frames until the end. Before the image frames are processed with the ccdproc task, the calibration frames must be processed.

3.2.4 Overscan

For the 0.5m telescope data, a fitting function for the overscan must be specified. I use a cubic spline fitting function and determine the number of spline pieces (order number) by interactively fitting the function in ccdproc. Using the parameters shown in Appendix A.3 (Table A.4 through Table A.7), ccdproc is executed on a few bias frames. To change the order number to 6 in the interactive window, the colon command *:order 6* is used. The new spline function is fit using the *f* key. The resulting RMS value can be found above the plot. Higher order functions usually have smaller RMS values. Smaller RMS values are desired

but at some point the difference in RMS values from one order to the next is not significant. I typically used order numbers between 7 and 10. The overscan strip correction is applied to all frames from the 0.5m telescope data. The 0.4m telescope data do not have overscan strips.

3.2.5 zerocombine

The 60 bias frames are combined together to generate the Zero level calibration image. The zerocombine task is used to combine the bias frames. This task works with other tasks including ccdproc. Appendix A.3 Table A.8 shows how the parameters of ccdproc are set before executing the zerocombine task. The only parameter I adjust in the zerocombine task before executing is the images parameter. The value of this parameter should be the same as the value given for the images parameter in the ccdproc task. Executing the zerocombine task creates the Zero level calibration frame named *Zero.fts*.

3.2.6 darkcombine

The 6 dark frames are averaged together to make the Dark count calibration image. The darkcombine task is used to combine the dark frames. Appendix A.3 Table A.9 shows how to set the parameters of ccdproc before executing the darkcombine task. The only parameter adjusted in the darkcombine task is the images parameter. It creates a calibration image named *Dark.fts*.

3.2.7 flatcombine

There are a total of 30 sky flats to combine, 10 for each bandpass filter Johnson B, Johnson V and Cousins R (R_C). The flatcombine task will combine flat frames of the same filter; the output will be three calibration images named *FlatB.fts*, *FlatV.fts* and *FlatR.fts*. The flatcombine task is able to process all of the flat frames at once. Appendix A.3 Table A.10

shows how to set the parameters in the ccdproc task before executing the flatcombine task. The only parameter adjusted in the flatcombine task is the images parameter. The flat field calibration images are the last of the calibration frames needed to process the object frames.

3.2.8 Process object frames

After the calibration frames have been processed the object frames are calibrated. The ccdproc task trims each object image. It also applies zero level correction, dark count correction and flat field correction to each object image. For object images from the 0.5m telescope, the overscan strip correction is also applied. Appendix A.3 Table A.11 shows how to set the parameters of ccdproc before executing it. After the ccdproc task is executed the object images are ready for photometry. The `ccdlist` task can be used to see what process have been applied to any image.

3.3 Heliocentric Julian Date

Although the object images are ready for photometric analysis, there is one change needed in each image header. To generate light curves for the binary star in the object images, the time that the image was taken is paired with the brightness of the photometry stars in the image. The Coordinated Universal Time (UTC) is the primary standard used by the scientific community. The UTC is recorded in the image header when an object image is taken. The use of UTC as the time parameter for generating light curves is appropriate for a single night but will be problematic when combining light curves from several nights. The problem is that the light arriving from the stars being observed have different path lengths at different times of the year. A different time parameter is needed to correct this problem. Using the observatory data and UTC, the `setjd` task is used to set the Heliocentric Julian Date (HJD) for each image. It automatically creates a parameter called HJD. The HJD is the time at which the light from the stars being observed would have reached the center of

the sun. This time is independent of where the Earth is at in its orbit and of which time zone the obsevatory is located.

Chapter 4

Data Analysis

Reduced photometric data of the W UMa type eclipsing binary systems (EBs) NSVS 3971593 and NSVS 7680691 are analyzed. Light curves are generated with differential aperture photometry. Initial analysis of the light curves reveals the orbital period of each system. Times of mideclipse (minimum light) are determined and used to calculate ephemerides. Apparent magnitudes of each system are determined by referencing the comparison stars to the Tycho-2 catalog (Høg *et al.* 2000). Effective temperatures of the stellar surfaces are determined from the color index $(B - V)$. The light curves, orbital periods and effective temperatures are used as input parameters by the PHOEBE (Prša 2005) software to model the EBs.

4.1 Differential Aperture Photometry

IRAF is used to perform aperture photometry on the EBs. The Aperture Photometry Package, `apphot`, which is found in the Digital stellar photometry package, `digiphot`, contains the necessary tasks. The primary task is `phot`, it provides flux measurements given in *instrumental magnitude*. Phot also calculates the error in the instrumental magnitude. The magnitude scale is logarithmic and arranged so that a smaller magnitude means a brighter star. A difference of 5 magnitudes between two stars corresponds to the star with the smaller

magnitude being 100 times brighter than the other.

In *differential* photometry, it is the difference in magnitude that is being measured. Light curve data of the binary systems are generated by taking the difference in instrumental magnitude between the variable (binary) star and the comparison star. The difference in instrumental magnitude between the comparison star and the check star is taken to ensure that the comparison star is not also a variable star. The comparison and check stars are selected to have nearly the same color and brightness as the variable star. An image of the W UMa type variable star NSVS 3971593 with the chosen comparison and check stars is shown in Figure 4.1. An image of the W UMa type variable star NSVS 7680691 with the chosen comparison and check stars is shown in Figure 4.2.

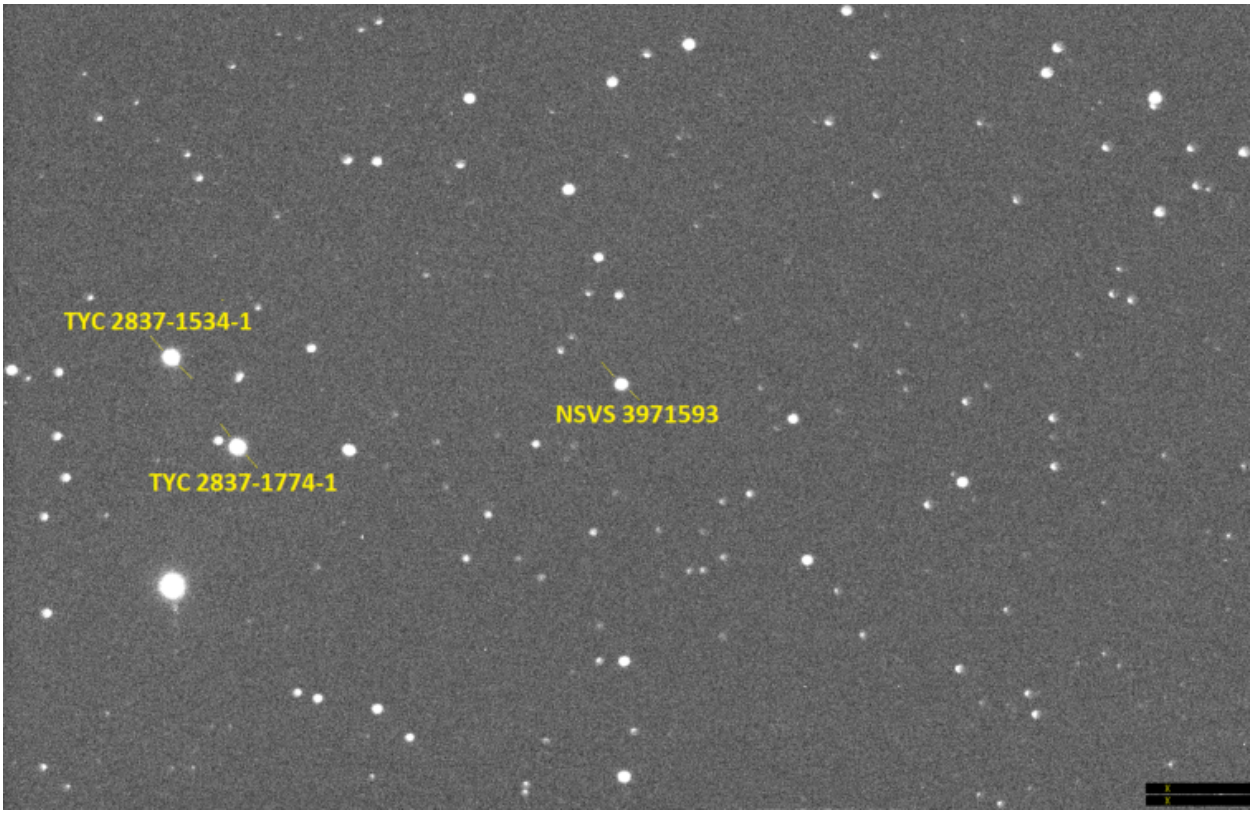

Figure 4.1: Trimmed image frame of W UMa type variable star NSVS 3971593, the comparison star TYC 2837-1774-1 and the check star TYC 2837-1534-1 taken with the 0.4m telescope.

The word *aperture* in differential aperture photometry refers to the method used to

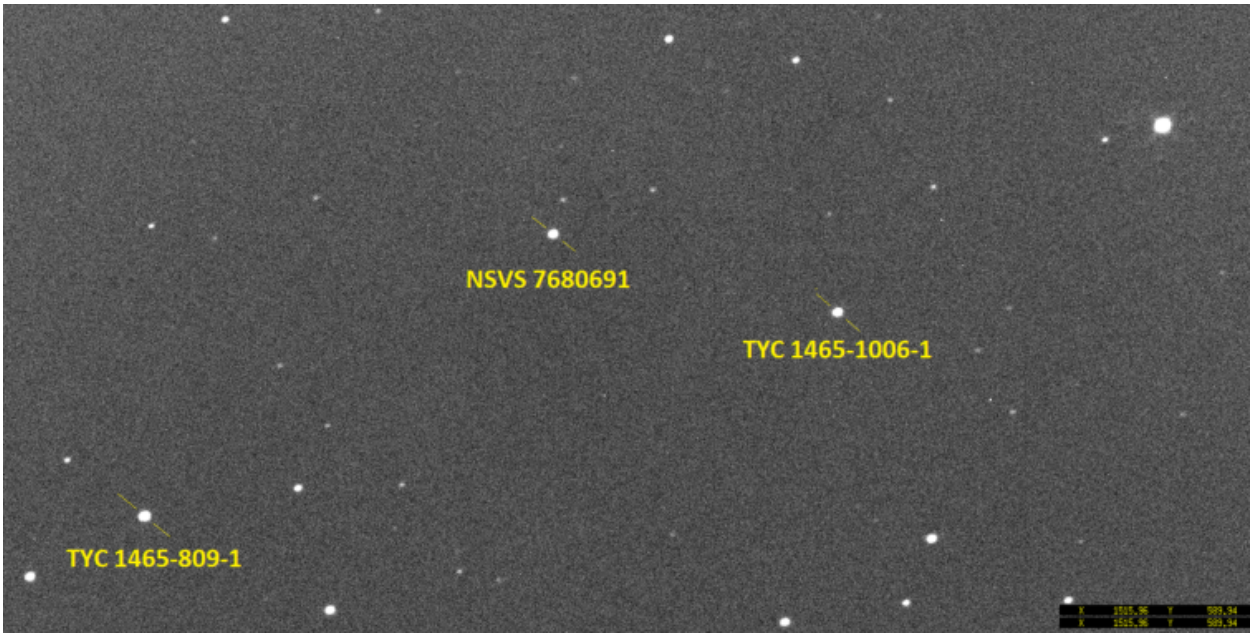

Figure 4.2: Trimmed mage frame of W UMa type variable star NSVS 7680691, the comparison star TYC 1465-809-1 and the check star TYC 1465-1006-1 taken with the 0.5m telescope.

calculate the instrumental magnitudes of the photometry stars. The aperture is simply a circle placed around a star on the image. The flux is taken as the sum of all pixel values inside the circle with the contribution of the sky background removed. The mean value of the sky background is measured with an annulus that is placed around the star. The annulus and aperture are concentric about the star center. The inner radius of the annulus is usually a few pixels larger than the aperture used to measure the brightness of the star. Pixels between the aperture and annulus are ignored. Values of pixels within the annulus are averaged to give the mean value of the sky background. The method used to select the size of each aperture and annulus used for photometry is discussed in Section 4.1.1.

Ideally, stars in the object images have Gaussian shapes. They are brightest at the their centers and become dimmer moving away from the centers. The outer edge of a star is not well defined, it is absorbed into the sky background. Therefore, the aperture used to measure the brightness of the star will not capture all of the light from the star. To have accurate measurements of stellar magnitude it is desirable to capture as much light

from the star as possible. Larger apertures capture more light, but they also yield greater errors in magnitude. The signal-to-noise ratio for the measurement is also a function of aperture radius. It decreases as the aperture radius is increased beyond an optimum value. Figure 4.3 shows a trimmed object image including the eclipsing binary star NSVS 7680691, the comparison star and the check star. Around each star, the phot task draws the aperture and annuli used to measure the instrumental magnitudes. I exclusively use XImtool to display and work with images in IRAF. Figure 4.4 shows the interactive screen display for the phot task. It shows a radial plot of the eclipsing binary star NSVS 7680691 and the placement of the aperture and annuli used to measure its instrumental magnitude.

4.1.1 Choosing Apertures

The method of choosing a suitable aperture begins by examining the radial profile of the stellar images. The aperture and annulus selected to measure the instrumental magnitudes of the binary star, comparison star and check star must be the same for all three stars in a given image. A way of characterizing a Gaussian distribution like the radial profile of a star is to measure the full width of the distribution at half its maximum value. After an image is displayed, the radial profile of a star can be plotted and its full width half max (FWHM) can be measured with the `imexamine` task. In the image displayed in Figure 4.3, the FWHM for the binary, companion and check star was measured to be 4.45, 4.42 and 4.40 (pixels) respectively.

Variability in atmosphere transparency (the *seeing*) over the course of an observation night causes the FWHM of a star to vary from image to image. Therefore, I use a different aperture and annuli for each image. The `psfmeasure` task, found in the Observing utilities package `obsutil`, is used to measure the FWHM of the binary star in every image. Appendix A.4 shows how to set task parameters. The optimum photometry aperture radius and sky annulus are calculated from the measured FWHM. The American Association of Variable Star Observers (AAVSO) CCD Observing Manual recommends using an aperture diameter

Figure 4.3: Trimmed object image of eclipsing binary star NSVS 7680691.Phot task draws the apertures and annuli around each star: Left- comparison star, Middle-binary star, Right-check star.

between 3 and 4 times the FWHM. For each image I set the aperture radius $r_{apt} = 2.0 \cdot FWHM$, the inner radius of the sky annulus $r_{in} = 4.0 \cdot FWHM$ and the width of the sky annulus $\Delta r_{annulus} = 1.3 \cdot FWHM$. Using these values, the area contained within the sky annulus is 3 times greater than the area contained within the aperture. This yields a good statistical determination of the sky background (Howell 2006).

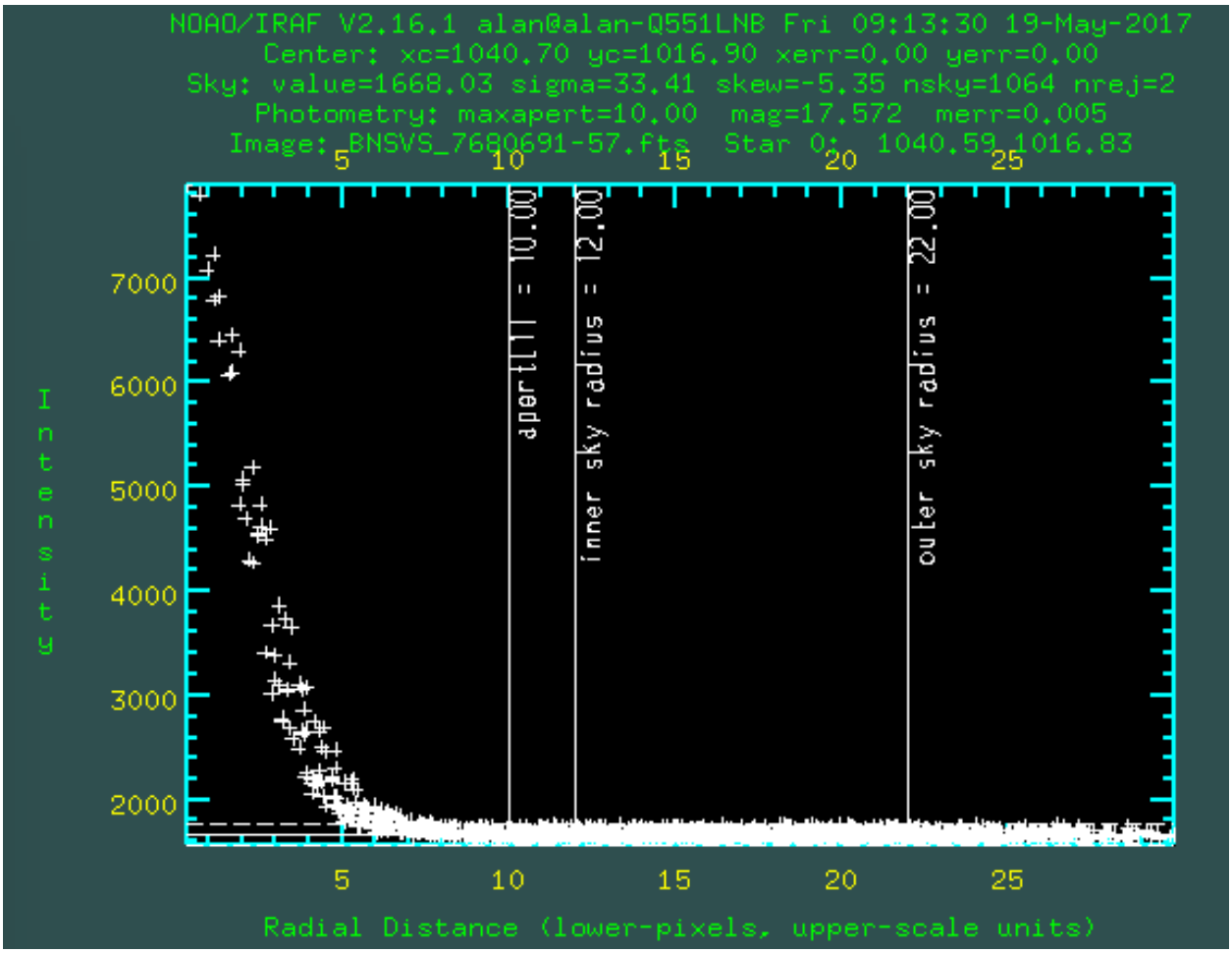

Figure 4.4: Screen Display from phot task. Intensity of pixels versus pixels. Shows radial profile of binary star and placement of aperture and annuli. Center of star is far left where intensity is greatest. Intensity of light from binary star decreases with increasing radial distance and becomes absorbed into the sky background. Sky background is marked with horizontal line. Vertical lines mark the placement of aperture and two annuli.

4.1.2 Coordinate List

In order for the phot task to perform photometry on a list of stars in an image, it must be able to find the stars in that image. The location of the stars vary from one image to the next. When photometry is done one image at a time, the image is displayed and the user can simply use the cursor to indicate the location of the stars. For a batch of images, the phot task must be instructed as to where to find the photometry stars in each image. Conveniently, most images have plate solutions. The plate solution is found in

the image header and provides a way to correlate a given pixel to a unique right ascension and declination. Once the photometry star locations are indicated on one image, phot can calculate the locations on any other image provided that it contains a plate solution. Images without plate solutions are rectified (aligned) before being analyzed with phot. Simple x and y coordinate transformations are made using the `imshift` task. It produces an image copy where the image center has been shifted by a certain number of pixels in x and y. The x-shifts and y-shifts are different for each image and they are calculated with the `imcentroid` task. The locations of the photometry stars in the shifted images do not vary from one image to the next. The procedure I used to create the shifted images is presented in Appendix A.5. Out of 20 nights of observational data, I have 4 nights from the 0.5m telescope where none of the images have plate solutions.

The phot task reads star locations from coordinate files created with the task `rimcursor`. For the shifted images, I use a different coordinate file for each batch and the coordinate format is left in the default *logical* system. The logical system sets the bottom left pixel to $(x, y) = (0, 0)$ and the scale unit to 1 pixel. For all other images, the output format is set to *world*. In this format, IRAF uses an image's plate solution to transform logical coordinates into right ascension and declination. In this format, the coordinate file can be used on different batches and different observation nights. For the EB NSVS 3971593, I only have data from the 0.4m telescope and I have plate solutions for all images. Thus, I only need one coordinate file for all of the data on this star. Three are needed for NSVS 7680691 data. One is created for data taken with the 0.4m telescope. Two are created for the data taken with the 0.5m telescope, the first is used for observations taken from the eastern half of the sky, the second is used for observations taken from the western half. The 0.5m telescope has a different mount than the 0.4m telescope. It performs a pier flip when tracking a target through the meridian. The star field images taken after the flip are rotated 180° compared to the field in images taken before. The pier flip necessitates the use of two separate coordinate files.

4.1.3 Measuring Instrumental Magnitudes

Before using the phot task, parameters in the `datapars` task are edited. These parameters tell other tasks in the apphot package where to look in the image headers for necessary information. The parameter list for datapars is shown in Appendix A.7. Images are separated into batches by bandpass filter and observation night. This is partially done due to the way a list of images is specified in the phot task. There is no graphical user interface (GUI) where images can be highlighted and phot can be made to work on the highlighted images. Instead, a list of images is typically specified with a single expression that incorporates the wild card character, *. This scheme demands that images in the same batch have a common set of characters in their filenames. It also demands that this common set of characters is not found in any other filenames that are present in the same directory. Images imported from the observatory computers have been separated into different directories, a different directory is created for each observation night. The image filenames always specify the bandpass filter. Therefore, it is convenient to separate batches by bandpass filter and observation night. To separate batches any other way would involve renaming images or placing them in a common subdirectory.

An example of how to set the phot task parameters is shown in Appendix A.7. Phot is used interactively to set the standard deviation of the sky (Sky Sigma). The Sky Sigma is measured in advance using the same task that calculates the FWHM, the imexamine task. The Sky Sigma is measured at several locations on a few different images in each batch. The values are averaged. Before the phot task is executed, the Sky Sigma parameter is set to the averaged value. To calculate r_{apt}, r_{in}, and $\Delta r_{annulus}$ for each image and pass these values to the phot task, I use a simple CL script. It is shown in Appendix A.7. Results of the phot task: instrumental magnitudes and errors in magnitude are written to magnitude files along with corresponding observation times (HJD). There is a magnitude file for every image. There may be more than one if the phot task is executed more than once on an image. Magnitude files created by the phot task must be processed. The `ptools` package, located

in the digiphot package, has a few tasks that are useful for extracting the data from the magnitude files. The `txconcat` task takes a list of magnitude files and combines them into one magnitude file. After all magnitude files of the same bandpass filter are combined, data from the combined file are written to a text file using the `txdump` task. The txdump task can be used to filter the data. Measurements of instrumental magnitude that have large errors can be excluded by setting the appropriate conditional. An example of the data extraction process is shown in Appendix A.8. My magnitude data is not filtered with txdump, instead it is filtered within a routine contained in the computer program that I wrote to generate light curves (see next section).

4.1.4 Generating Light Curves

After executing the phot task on a batch of images and processing the resulting magnitude files, I still needed a way to calculate differential magnitudes and propagated magnitude errors. To do this, I wrote a program in Python programming language named *process.py* that reads the text files created by the txdump task. If a batch has N images, the text file will contain a list of observation times t_i where $i = 1, 2, 3, \cdots, N$. For every observation time there are instrumental magnitude measurements for the variable star V_i, the comparison star $C1_i$ and the check star $C2_i$. There are also the errors associated with these magnitudes: σ_{V_i}, σ_{C1_i} and σ_{C2_i} respectively. The program calculates the differential magnitudes $V_i - C1_i$ and $C2_i - C1_i$. It also calculates the propagated magnitude errors $\sigma_{V_i - C1_i}$ and $\sigma_{C2_i - C1_i}$. Magnitude errors are summed in quadrature:

$$\sigma_{V_i - C1_i} = \sqrt{\sigma_{V_i}^2 + \sigma_{C1_i}^2}, \tag{4.1}$$

$$\sigma_{C2_i - C1_i} = \sqrt{\sigma_{C2_i}^2 + \sigma_{C1_i}^2}. \tag{4.2}$$

The program writes an output data file with a five column format. Each line in the output

file contains the observation time t_i (HJD), the differential magnitudes $V_i - C1_i$ and $C2_i - C1_i$ and the propagated errors $\sigma_{V_i - C1_i}$ and $\sigma_{C2_i - C1_i}$. The N calculated values of $V_i - C1_i$ are plotted over observation time to produce a light curve for the variable star.

The differential magnitudes $C2_i - C1_i$ are also plotted versus observation time. Ideally, each value is identical giving a linear plot with zero slope. Figure 4.5 is a plot of observed differential magnitudes generated by the process.py program. Except for values obtained in the last hour of the observing session, most differential magnitudes are close to the average value $\Delta m = 0.04$. The plot not only displays the absence of any significant variability in the comparison star, it indicates that I need to discard the last hour of data. I wrote a second Python program named *combine.py* that takes the generated light curve data files from each observation night and combines them into three files, one for each bandpass filter.

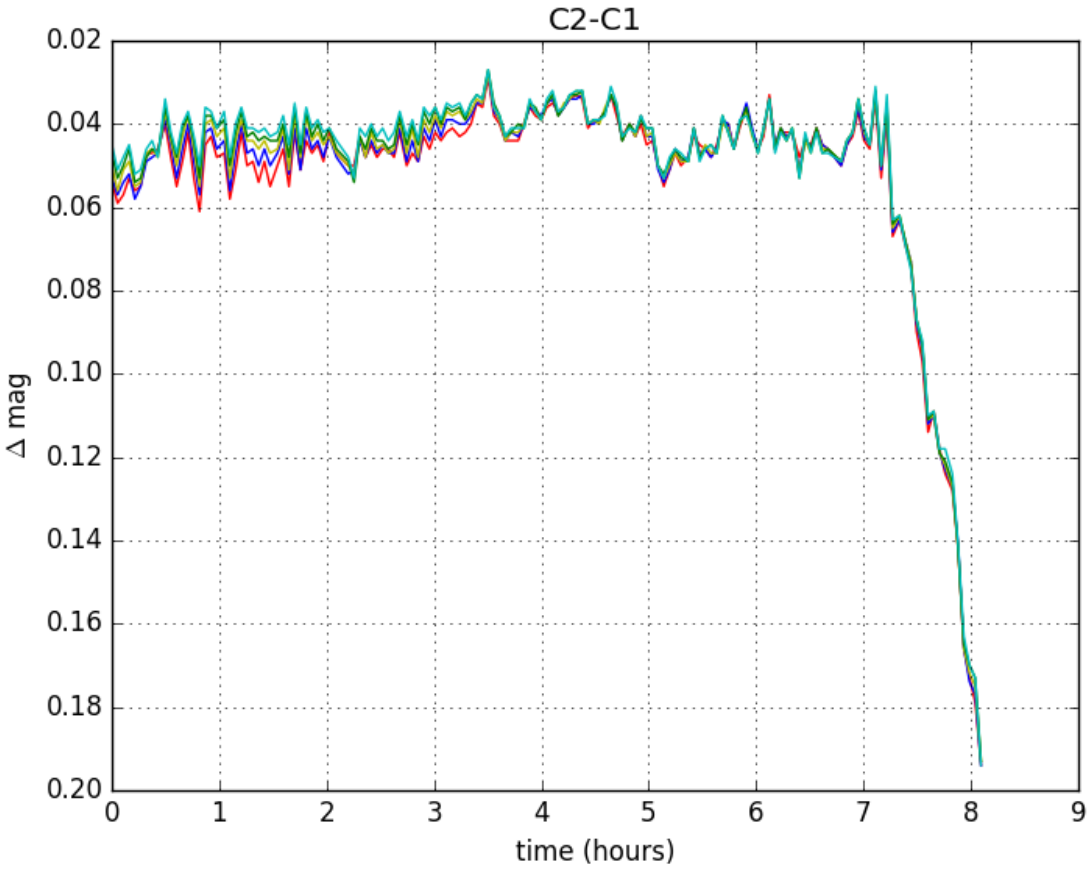

Figure 4.5: Differential light curves of C2-C1 created with the process.py program. The program calculates five different light curves, each created using a different set of apertures. Red curve: $r_{apt} = 1.500 \cdot FWHM$, blue curve: $r_{apt} = 1.625 \cdot FWHM$, yellow curve: $r_{apt} = 1.750 \cdot FWHM$, green curve: $r_{apt} = 1.875 \cdot FWHM$ and cyan curve: $r_{apt} = 2.000 \cdot FWHM$. The plot indicates that the comparison star is non-variable and also suggests that roughly the last hour of data should be discarded.

4.2 Orbital Period

The photometric data contained in the files generated by the python programs can be plotted to make light curves of the EBs. The curves are nearly sinusoidal. Curves that belong to the same binary star have a common period. This is the orbital period of the binary star. Before the light curves are loaded into the modeling software, PHOEBE (Prša 2005), the Johnson B, Johnson V and Cousins R (R_C) magnitudes are *folded* over the orbital period. The light curve of each binary star is cut into temporal sections equal to its orbital period. The sections are stacked together and the heliocentric Julian date is replaced with orbital phase. The orbital phase Φ is a function of time T and is defined with Equation 4.3. In this equation, T_0 is the epoch of the binary system and P is the period. The earliest observed primary eclipse defines T_0. A primary eclipse corresponds to the greatest light loss from the binary system, when the hotter component star is blocked from view (Henden & Kaitchuck 1982).

$$\Phi = \frac{T - T_0}{P} - \mathrm{Int}(\frac{T - T_0}{P}). \tag{4.3}$$

4.2.1 Initial Analysis

The `pdm` task in IRAF performs orbital period determination using phase dispersion minimization (Stellingwerf 1978). The parameter list is shown in Appendix A.9. I use the pdm task to quickly view folded light curves. It displays the period and epoch. I do not keep values determined by the pdm task. The orbital periods of the binary systems are determined with PERANSO software employing the analysis of variance (ANOVA) statistic (Schwarzenberg-Czerny 1996). It uses periodic orthogonal polynomials to fit observed light curves. The software allows the user to view folded light curves and identify outliers in the data set. Figure 4.6 shows the folded differential magnitudes versus orbital phase for NSVS 3971593. Figure 4.7 shows the folded differential magnitudes versus orbital phase for NSVS

7680691.

Orbital Periods

Eclipsing Binary Star	Period
NSVS 3971593	0.655722 ± 0.000211
NSVS 7680691	0.273007 ± 0.000060

Table 4.1: Orbital Periods determined by PERANSO software employing the analysis of variance (ANOVA) statistic.

4.2.2 The Ephemeris

The ephemeris is an equation that predicts when an EB can be observed in a particular orbital phase. The Heliocentric Julian dates corresponding to both primary and secondary eclipses are used to generate the ephemeris. These times are called *times of minimum light* because the light from the binary star is at a minimum at mideclipse. The observed times of minimum light are determined using the algorithm presented by Kwee and van Woerden (1967). The algorithm is implemented via a Fortran program (Robert Berrington, private communication 2016). It accepts cursor input from a graphical display of the observed light curve (see Figure 4.8). The user can zoom in on an eclipse and select one of the data points near mideclipse as the *guess* time of minimum T_1. A time width w symmetric about T_1 containing N data points is also selected. $(2n + 1)$ magnitudes spaced by equal time intervals Δt are generated by linear interpolation between consecutive data points contained in w, where $2n + 1 \approx N$. Taking time T_1 as a reflection axis yields n pairs of magnitudes equidistant and on opposite sides of T_1. The differences of these magnitude pairs Δm_k $(k = 1, 2, \cdots, n)$ are taken and the sum

$$s(T_1) \equiv \sum_{k=1}^{n} (\Delta m_k)^2 \tag{4.4}$$

is calculated. The reflection axis is then shifted to $(T_1 + \frac{1}{2}\Delta t)$ to calculate the sum $s(T_1 + \frac{1}{2}\Delta t)$

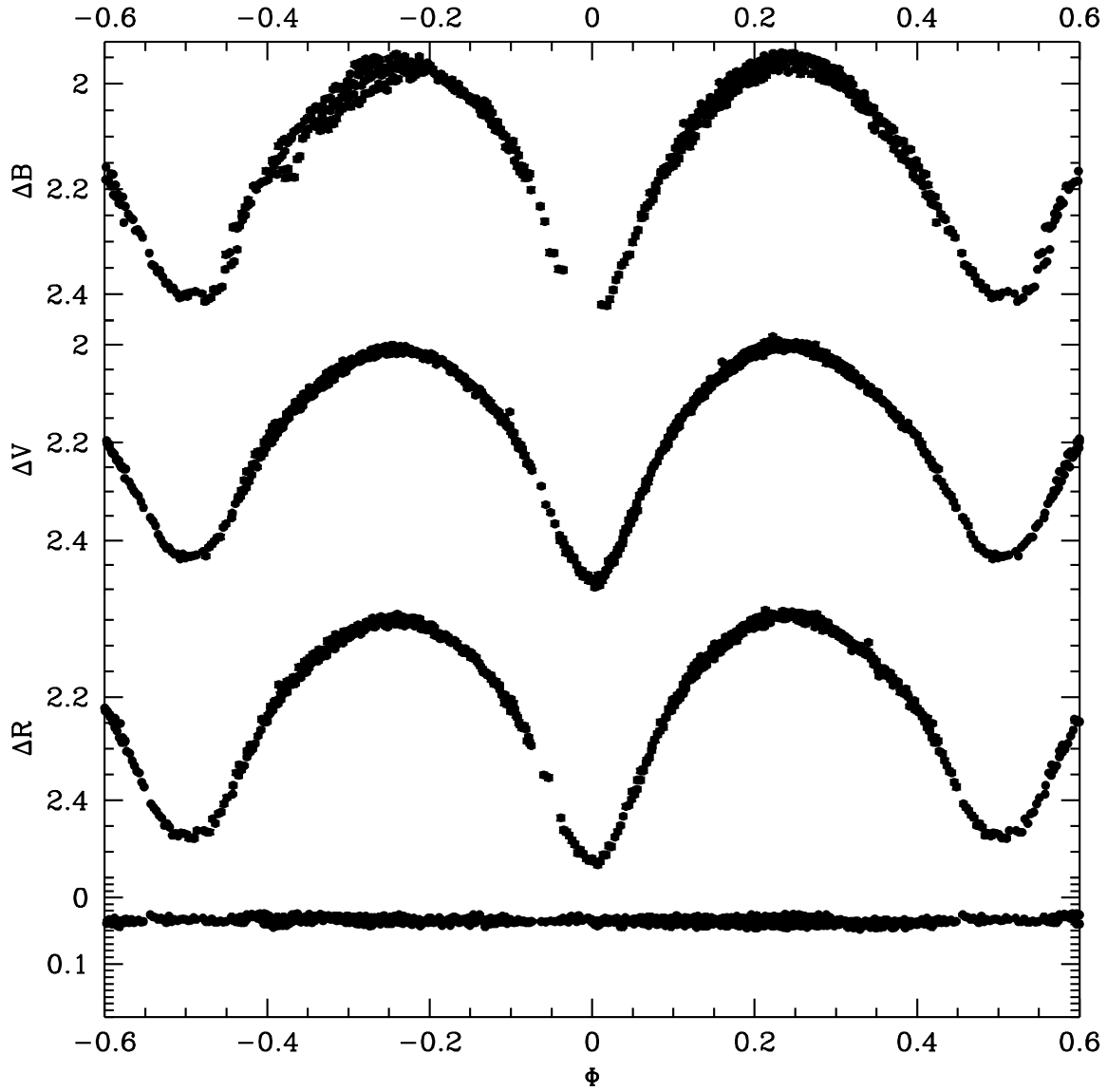

Figure 4.6: Folded light curves for differential aperture Johnson B, Johnson V and Cousins R magnitudes for NSVS 3971593. Phase values are defined by Equation 4.3. Top three panels show the folded light curves for Johnson B (top panel), Johnson V (middle panel), and Cousins R (bottom panel) magnitudes. Bottom panel shows the Johnson V-band magnitudes for the comparison minus the check star. All error bars are 1σ error bars. Repeated points do not show bars (points outside the phase range of $(-0.5, 0.5)$).

and shifted to $(T_1 - \frac{1}{2}\Delta t)$ to calculate the sum $s(T_1 - \frac{1}{2}\Delta t)$. Note that a different *guess* time of minimum T_1 must be selected if $s(T_1) > s(T_1 + \frac{1}{2}\Delta t)$ or if $s(T_1) > s(T_1 - \frac{1}{2}\Delta t)$. The function $s(T)$ is represented by a quadratic equation where the constants a, b and c are determined from a set of simultaneous equations (see Equation 4.5) using the values $s(T_1)$,

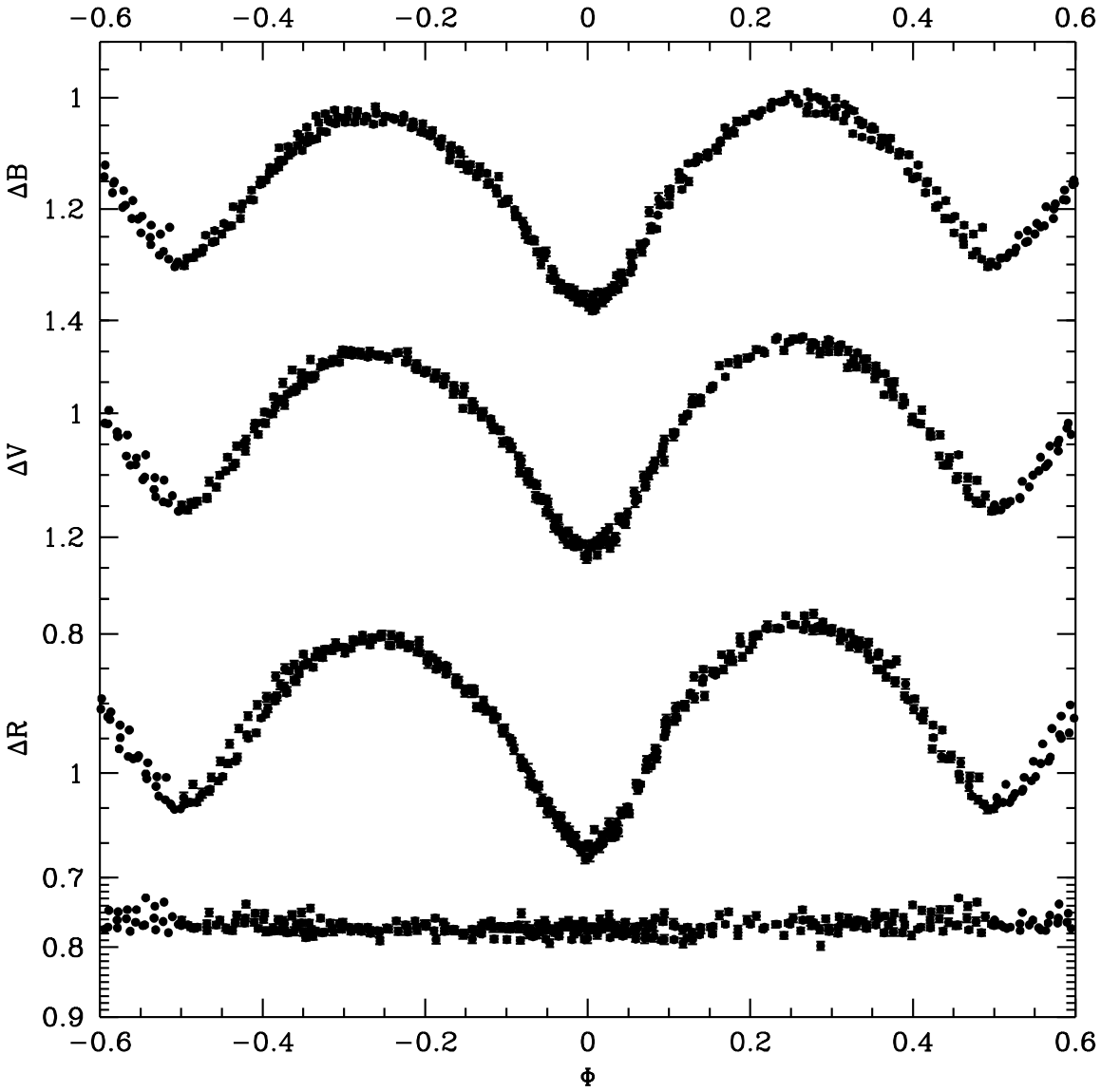

Figure 4.7: Folded light curves for differential aperture Johnson B, Johnson V and Cousins R magnitudes for NSVS 7680691. Phase values are defined by Equation 4.3. Top three panels show the folded light curves for Johnson B (top panel), Johnson V (middle panel), and Cousins R (bottom panel) magnitudes. Bottom panel shows the Johnson V-band magnitudes for the comparison minus the check star. All error bars are 1σ error bars. Repeated points do not show bars (points outside the phase range of $(-0.5, 0.5)$).

$s(T_1 + \frac{1}{2}\Delta t)$ and $s(T_1 - \frac{1}{2}\Delta t)$. The minimum value of the parabola represented by

$$s(T) = aT^2 + bT + c \tag{4.5}$$

is identified as the time of minimum light. Observed times of minimum light from each

bandpass filter are averaged together. The time corresponding to the earliest primary eclipse defines T_0, the *ephemeris epoch*. All future primary eclipses T_{pe} can then be calculated by

$$T_{pe} = T_0 + P \times E, \tag{4.6}$$

where P is the orbital period and E is the epoch number. The epoch number is the integer number of orbital periods that have transpired since T_0.

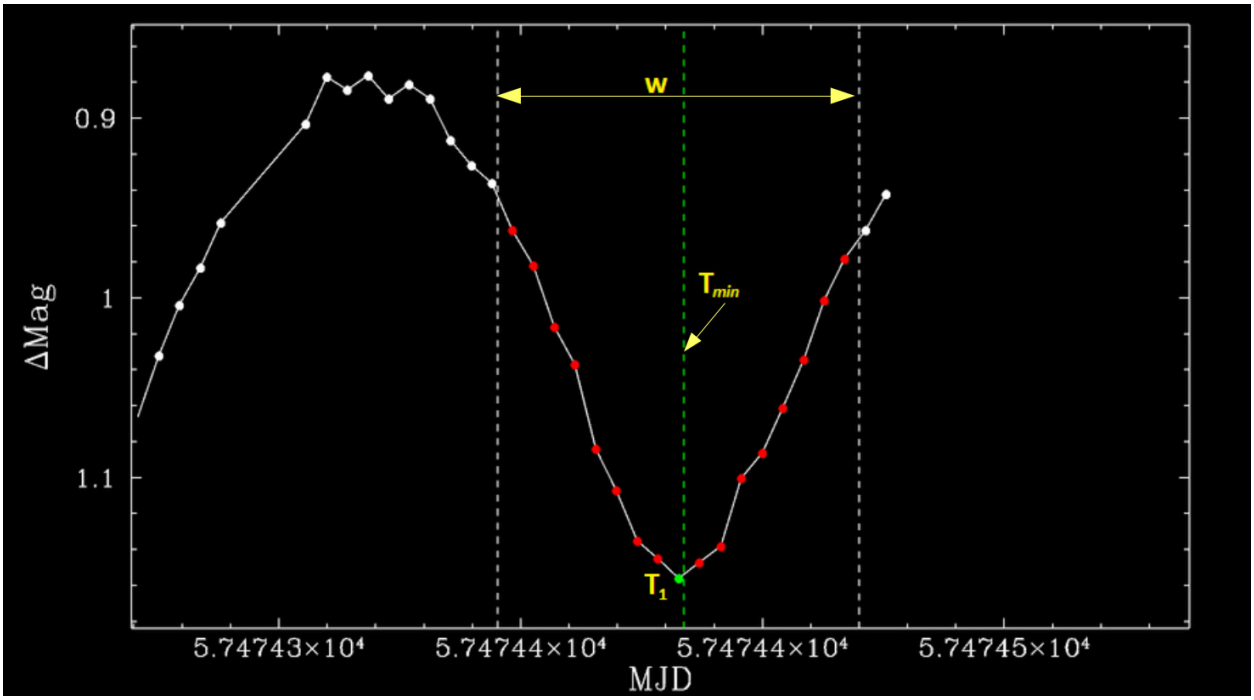

Figure 4.8: Graphical display of Johnson V differential magnitudes observed on April, 14 2016 with the 0.5m telescope at the Ball State University Observatory. Units of time are given in Modified Julian Date (MJD) where $MJD = HJD - 2400000.5$. The guess time of minimum light T_1 (*green datum point*) and time width w are indictaed. Besides T_1, there are 16 additional observed data points (*red data points*) contained within w. The algorithm presented by Kwee and van Woerden (1967) is used to determine the observed time of minimum T_{min} (*middle dashed line*).

According to the 81^{st} compilation of BAV results, Hubscher (2015) observed the binary system NSVS 3971593 to have an eclipse at $T_{min} = 2456940.4695 \pm 0.0113$. I determine this to be a secondary eclipse. The observed times of minimum, times determined directly from the algorithm by Kwee and van Woerden, are compared to the times of minimum

calculated with Equation 4.6 using the orbital periods determined in this investigation. The observed times of minimum T_{min} for NSVS 3971593 are shown in Table 4.2. Observed times of minimum for NSVS 7680691 are shown in Table 4.3. The observed times of minimum minus calculated times of minimum $(O-C)$ are also shown along with 1σ error bars. Figure 4.9 shows the plot of $(O-C)$ versus epoch number E for NSVS 3971593. Figure 4.10 shows the plot of $(O-C)$ versus epoch number E for NSVS 7680691. For each plot, a best-fit line is determined by a linear regression. The slope of the best fit line can be used to make a small correction to the period.

Times of Minimum for NSVS 3971593

T_{min}	Eclipse	E	$(O-C)$
$2456940.469500 \pm 0.0113^{\dagger}$	s	-602.5	0.009678 ± 0.011327
$2457314.879842 \pm 0.000921$	s	-31.5	0.002758 ± 0.001205
$2457335.532327 \pm 0.000776^{*}$	p	0.0	0 ± 0.000776
$2457340.778396 \pm 0.000618$	p	8.0	0.000293 ± 0.000993

Table 4.2: Calculated Heliocentric Julian Dates (HJD) for the observed times of minimum (*column 1*) with the type of minima (*column 2*). Observed minus calculated $(O-C)$ residual values (*column 4*) are given for the linear ephemeris (Equation 4.6) using the orbital period determined by PERANSO $P = 0.655722$ days. All reported times are averaged from the B, V and R_C bandpass times of minimum determined by the algorithm described by Kwee & van Woerden (1967). All $(O-C)$ values are given in units of days with primary eclipse values determined from integral epoch numbers, and secondary eclipse values determined from half integer values (*column 3*). Ephemeris Epoch T_0 is indicated with an Asterisk. Observed minimum from BAV results is indicated with a dagger.

Times of Minimum for NSVS 7680691

T_{min}	Eclipse	E	$(O-C)$
(1)	(2)	(3)	(4)
$2457474.744624 \pm 0.000538^{*}$	p	0.0	0 ± 0.000538
$2457474.882397 \pm 0.000440$	s	0.5	0.001270 ± 0.000695
$2457493.719459 \pm 0.001035$	s	69.5	0.000849 ± 0.001167
$2457493.854822 \pm 0.000332$	p	70.0	-0.000292 ± 0.000632
$2457494.674417 \pm 0.000622$	p	73.0	0.000282 ± 0.000822
$2457494.809316 \pm 0.000920$	s	73.5	-0.001322 ± 0.001066
$2457495.765957 \pm 0.000548$	p	77.0	-0.000206 ± 0.000768
$2457496.858078 \pm 0.000555$	p	81.0	-0.000113 ± 0.000773
$2457502.589946 \pm 0.000201$	p	102.0	-0.001392 ± 0.000574
$2457502.728009 \pm 0.001320$	s	102.5	0.000167 ± 0.001425
$2457502.863747 \pm 0.000634$	p	103.0	-0.000598 ± 0.000831

Table 4.3: Calculated Heliocentric Julian Dates (HJD) for the observed times of minimum (*column 1*) with the type of minima (*column 2*). Observed minus calculated $(O-C)$ residual values (*column 4*) are given for the linear ephemeris (Equation 4.6) using the orbital period determined by PERANSO $P = 0.273007$ days. All reported times are averaged from the B, V and R_C bandpass times of minimum determined by the algorithm described by Kwee & van Woerden (1956). All $(O-C)$ values are given in units of days with primary eclipse values determined from integral epoch numbers, and secondary eclipse values determined from half integer values (*column 3*). Ephemeris Epoch T_0 is indicated with an Asterisk.

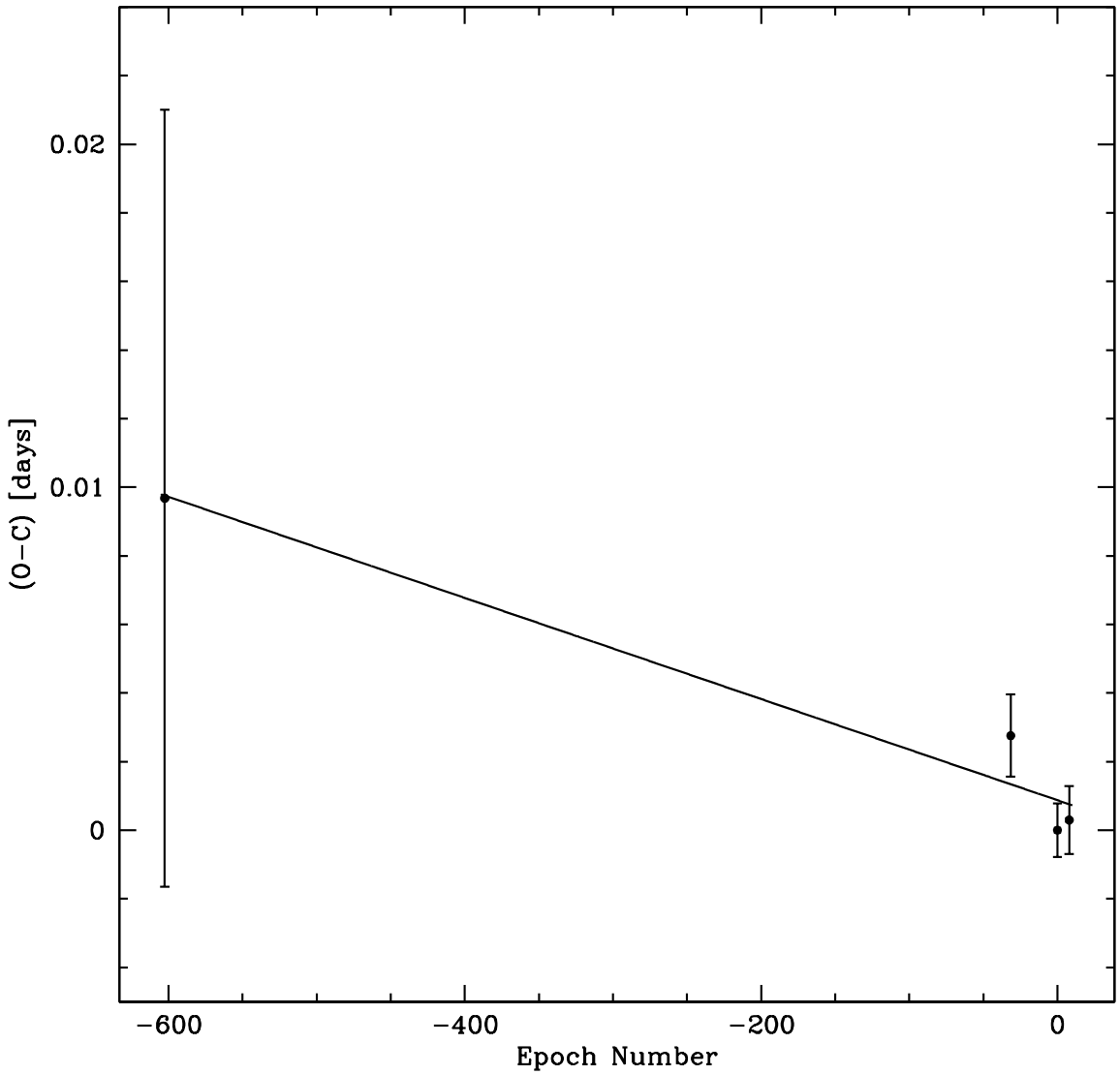

Figure 4.9: Observed minus calculated residual times of minimum $O-C$ versus orbital epoch number for NSVS 3971593. All points are given in Table 4.2. Secondary eclipses are plotted at half integer values and all error bars are 1σ error bars. Solid line shows the best-fit line determined by a linear regression fit to the $(O-C)$ residual values. The slope of the best-fit line suggests a correction to the orbital period that is less than the error in the period determined by PERANSO. I do not use it to adjust the orbital period determined in this investigation.

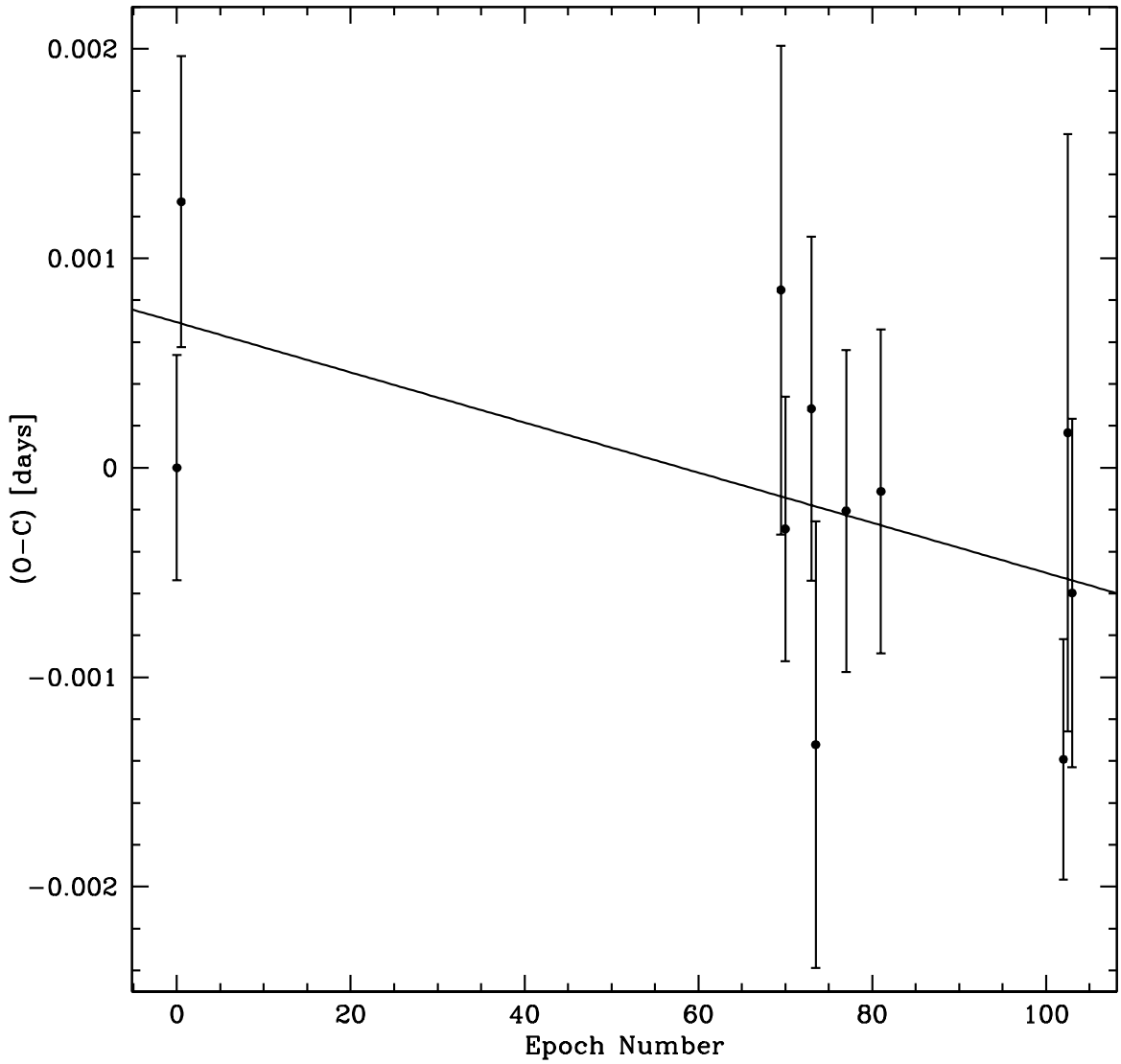

Figure 4.10: Observed minus calculated residual times of minimum $O - C$ versus orbital epoch number for NSVS 7680691. All points are given in Table 4.3. Secondary eclipses are plotted at half integer values and all error bars are 1σ error bars. Solid line shows the best-fit line determined by a linear regression fit to the $(O-C)$ residual values. The slope of the best-fit line suggests a correction to the orbital period that is less than the error in the period determined by PERANSO. I do not use it to adjust the orbital period determined in this investigation.

4.3 Effective Temperature

Light curves are analyzed to determine the effective surface temperatures of the binary systems. Apparent Johnson B and Johnson V magnitudes for the EBs are estimated by referencing known magnitude values. The comparison stars used for differential photometry are members of the Tycho-2 catalog (Høg *et al.* 2000), a list of bright stars containing measurements of apparent magnitudes. Data from the catalog is accessed via the SIMBAD Astronomical database; Johnson B and Johnson V bandpass magnitude data are given in Table 4.4. The V-band apparent magnitude of the comparison star is added to the differential V-band magnitude to find the V-band apparent magnitudes of the binary star. The B-band apparent magnitude is found similarly.

Apparent magnitudes are given to a Fortran program (Robert Berrington, private communication 2016) that determines the $(B-V)$ *color index*. A star with a smaller $(B-V)$ color is *bluer* than a star with a larger value of $(B-V)$ (Carroll & Ostlie 2007). All $(B-V)$ colors are calculated by subtracting linearly interpolated B magnitudes from measured V magnitudes. Figure 4.11 shows the V-band apparent magnitude folded light curve for NSVS 3971593 and measured values of its color index $(B-V)$. Figure 4.12 shows the V-band apparent magnitude folded light curve for NSVS 7680691 and measured values of its color index $(B-V)$. Color index values observed at orbital quadrature (orbital phase $\Phi = \pm 0.25$) are used to estimate effective surface temperatures of the EBs. Times of maximum light occur at quadrature. $(B-V)$ values observed at max I ($\Phi = 0.25$) and max II ($\Phi = -0.25$) are averaged together and reported as $(B-V)$ in Table 4.5. The range of $(B-V)$ values observed at quadrature determine the error in the reported value.

Interstellar extinction is the reddening of starlight as its bluer wavelengths are scattered and absorbed by dust clouds within the galaxy. Accurate determination of reddening to a star is vital for reliable derivation of its effective temperature (Yuan, Liu & Xiang 2013). A common measurement of interstellar reddening is *color excess* $E(B-V)$. It is determined with the extinction law

$$R \equiv \frac{A_\lambda}{E(B-V)}, \tag{4.7}$$

where $R \sim 3.1$ for the V-band (Fitzpatrick 1999) and A_λ represents the number of magnitudes of interstellar extinction present along a particular line of sight for a given bandpass (Carroll & Ostlie 2007). The given bandpass is a narrow range of wavelengths centered on the wavelength λ. Extinction varies with the observer's line of sight. It is typically larger for objects closer to the galactic center of the Milky Way where there is more interstellar dust. The NED Coordinate & Extinction Calculator via the NASA/IPAC Extragalactic Database is accessed to find the interstellar extinction estimates for the galactic coordinates of the EBs. Values for the Landolt V bandpass extinction $A_\lambda(V)$ reported by Schlafly & Finkbeiner (2011) are given in Table 4.5. they are used to find the color excess for each EB.

Effective temperatures and errors are estimated from Table 3 of Flower (1996). Table 3 lists numerical relations between intrinsic color index values $(B-V)_0$ and effective temperatures T_{eff}. The intrinsic color index value is found by subtracting the color excess from the observed color index value 4.8 using

$$E(B-V) \equiv (B-V) - (B-V)_0. \tag{4.8}$$

Effective temperatures have corresponding stellar spectral types given by Fitzgerald (1970). The binary star NSVS 3971593 is an F0. The binary star NSVS 7680691 is a G4. Table 4.5 lists the intrinsic color values, the effective temperatures and spectral classes of the EBs.

Binary Star (NSVS ID)	Comparison Star (Tycho ID)	B magnitude (value)	V magnitude (value)
3971593	2837-1774-1	9.46 ± 0.02	9.03 ± 0.02
7680691	1465-809-1	11.92 ± 0.11	11.37 ± 0.10

Table 4.4: Magnitude data from the SIMBAD database for comparison stars used in photometry for NSVS 3971593 and NSVS 7680691.

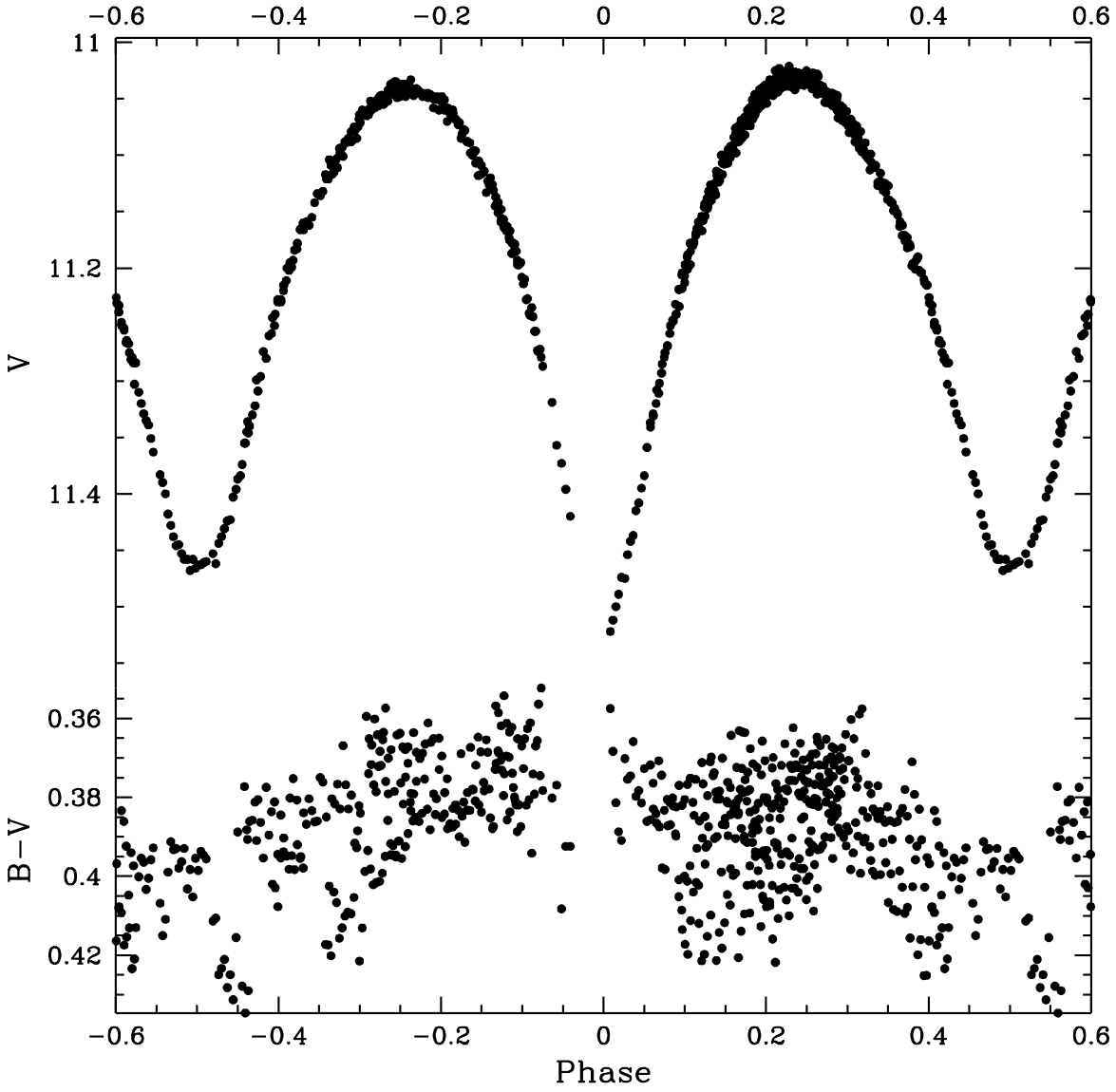

Figure 4.11: Folded light curve for the differential aperture Johnson V-band magnitudes (top panel) and (B-V) color (bottom panel) versus orbital phase for NSVS 3971593. Phase values are defined by Equation 4.3. Error bars are not shown for clarity. All (B-V) colors are calculated by subtracting linearly interpolated B magnitudes from measured V magnitudes.

4.4 Modeling of W UMa Systems

Modeling is completed with PHOEBE software. Observed differential magnitudes B, V and R_C constitute a set of observables $\mathbf{O^{obs}}$. Observables are phase dependent quantities such as luminosity and magnitude; they can be plotted as a function of phase to produce a

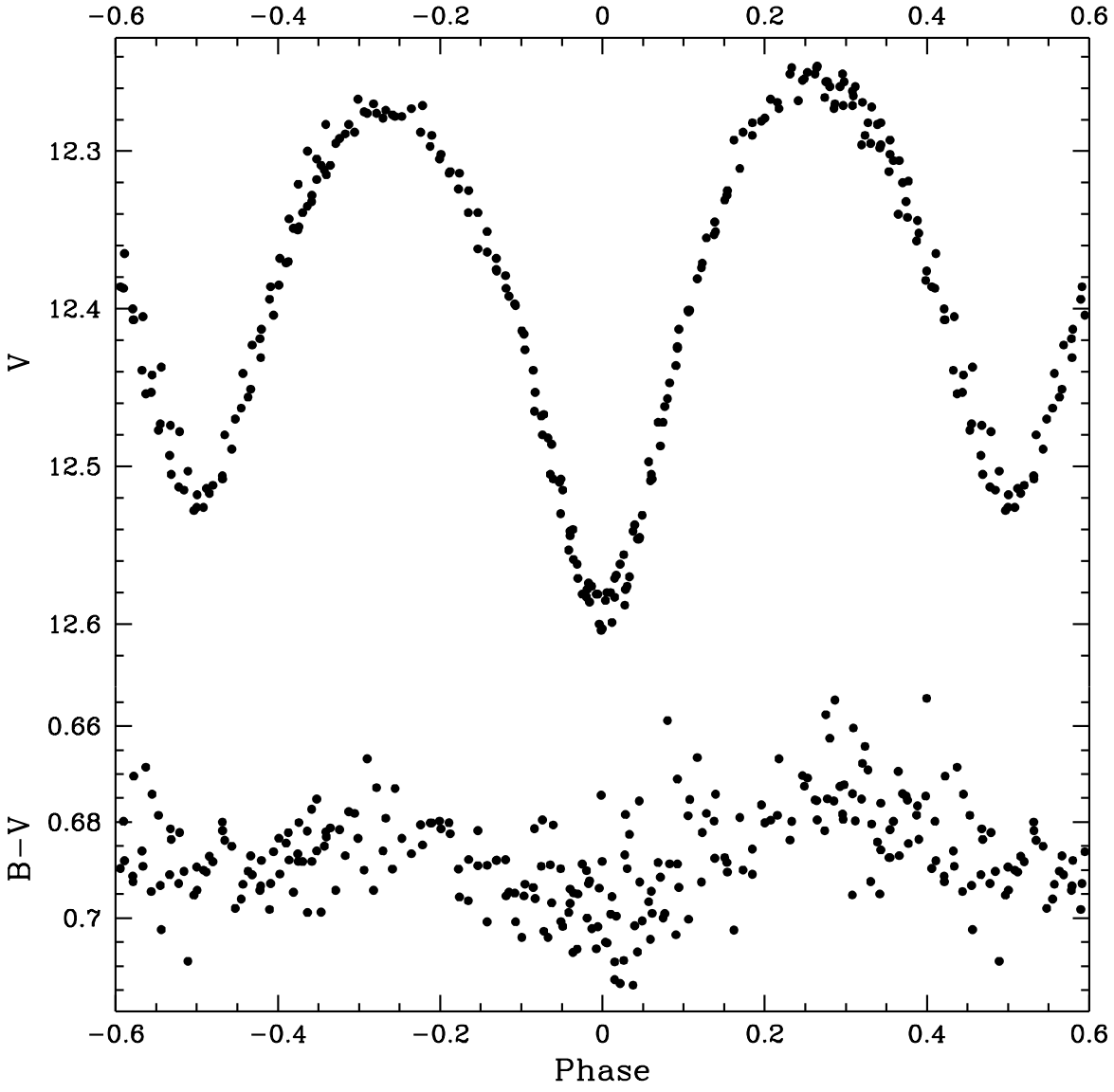

Figure 4.12: Folded light curve for the differential aperture Johnson V-band magnitudes (top panel) and (B-V) color (bottom panel) versus orbital phase for NSVS 7680691. Phase values are defined by Equation 4.3. Error bars are not shown for clarity. All (B-V) colors are calculated by subtracting linearly interpolated B magnitudes from measured V magnitudes.

light curve. To monitor the fitting progress the program takes the present values assigned to the set of parameters $\mathbf{x}$ and generates a synthetic light curve. The model calculates a set of observables $\mathbf{O^{calc}}$ from $\mathbf{x}$. To visually check the fit, the observed and synthetic light curves are plotted on the same plot. The goal of my investigation is to establish the set of orbital

NSVS 3971593		NSVS 7680691	
parameter	value	parameter	value
(1)	(2)	(3)	(4)
$(B-V)$	0.386 ± 0.052	$(B-V)$	0.675 ± 0.018
A_λ (V)	0.200	A_λ (V)	0.044
$E(B-V)$	0.065	$E(B-V)$	0.014
$(B-V)_0$	0.3210 ± 0.052	$(B-V)_0$	0.661 ± 0.018
T_{eff}	7110 ± 250 K	T_{eff}	5669 ± 120 K
Spectral type	F0	Spectral type	G4

Table 4.5: Color index (observed and intrinsic), extinctions, color excess, effective temperature and spectral type of binary stars NSVS 3971593 and NSVS 7680691.

parameters $\mathbf{x_0}$ for my selected binary systems. The determination of orbital parameters is done by finding the synthetic light curves that best-fit the observed light curves. The measure of deviation between $\mathbf{O^{calc}}$ and $\mathbf{O^{obs}}$ is the sum of the squared residuals χ^2. As the fitting progress optimizes the orbital parameters $\mathbf{x}$, χ^2 is minimized. The residuals between $\mathbf{O^{calc}}$ and $\mathbf{O^{obs}}$ can be displayed in the plotting section. A solution $\mathbf{x_0}$ is found when the residuals plot is nearly flat (minimized). For each EB, a star spot is introduced to the primary stellar component in the parameter section by specifying and fitting a combination of four parameters. The spot colatitude ϕ_1 is set to 90°; all spot models are limited to solutions where the location of the spot is on the equator of the primary component. The spot longitude λ_1, spot radius ϱ_1, and temperature factor $\tau_1 = \frac{T_{spot}}{T_{eff}}$ are fit by keeping two of the three fixed while optimizing the third. The pair being held fixed is alternated in between successive iterations. Finally, after the four spot parameters have been established, they are held fixed while the other parameters are allowed to converge onto a final solution. For each EB I present two solutions. One incorporates a star spot in the model, the other does not.

Chapter 5

W Ursae Majoris type variable star NSVS 3971593

The star NSVS 3971593 [= TYC 2837-1526-1, R. A. = $2^h5^m15.85^s$, Dec. = $+41°28'13.68''$, J2000.0] was found to be a variable star using photometric data from the NSVS (Woźniak 2004). Afterwards, Hoffman *et al* (2009) classified it as a W UMa type variable star and reported an orbital period of $P = 0.65552$ days. My observations of NSVS 3971593 span from 2015 September to 2015 December. Over ten nights a total of 2,213 images were taken in three bandpass filters: Johnson B, Johnson V and Cousins R (R_C). Images were reduced with IRAF (Tody 1993). Period analysis with PERANSO software (CBA Belgium Observatory 2011) yields an orbital period $P = 0.655722 \pm 0.000211$ days which is consistent with that reported by Hoffman *et al* (2009). Light curves are generated with differential photometry. Johnson B and Johnson V instrumental differential magnitudes are combined with the known calibrated Johnson B and Johnson V magnitudes of the comparison star TYC 2837-1774-1 to produce apparent magnitudes for NSVS 3971593. Effective temperature and spectral type are estimated from the $(B - V)$ color index measured at orbital quadrature ($\Phi = \pm 0.25$). The observed value $(B - V) = 0.386 \pm 0.052$ is corrected using the extinction coefficient $E(B - V) = 0.065$ from Schlafly & Finkbeiner (2011) at the galactic coordinates

for the binary star. The resulting intrinsic color index $(B-V)_0 = 0.3210 \pm 0.052$ indicates a spectral type F0 (Fitzgerald 1970) and an effective temperature of $T_{eff} = 7110 \pm 250$ K (Flower 1996). If NSVS 3971593 is assumed to be a normal main sequence star, Equation 4 of Harmanec (1988) estimates the stellar mass to be $M_\star = 1.52 \pm 0.08\ M_\odot$. With this mass estimate, Kepler's Harmonic law (see Equation 1.1) gives the semi-major axis $a = 4.61 \pm 0.08\ R_\odot$.

5.1 WD model

The PHOEBE modeling package (Prša & Zwitter 2005) is used to establish orbital parameters of eclipsing binary system NSVS 3971593. All three folded light curves, Johnson B, Johnson V and Cousins R_C are fit simultaneously. The binary system is assumed to be an over-contact binary of the W UMa type. The initial model constraint is set accordingly. The outer envelopes of the binary star are assumed to be convective; the gravity brightening coefficients β_1 (primary) and β_2 (secondary) defined by $F_{\text{surf}} \propto g^\beta$ (see Equation 1.12) are set to 0.32 (Lucy 1967). Values for the epoch T_0, orbital period P and effective temperature T_{eff} are entered in the parameters section. The bolometric albedo of each stellar component A_1 and A_2 is set to 0.5 as suggested by Ruciński (1969). Limb Darkening coefficients are interpolated with the logarithmic law using van Hamme (1993) tables. The reflection effect is optioned with two possible reflections. A crude initial fit is made using the initial default values for the monochromatic luminosities and surface potential Ω. Once the initial fit cannot be improved with further iterations, the orbital inclination i and mass ratio q parameters, with initial values $i = 80°$ and $q = 1.00$, are selected to be included in the fitting procedure.

Without radial velocity data, it is not possible to unequivocally determine the mass ratio q (K. B. Alton 2016). A q-search method is used to establish a photometric mass ratio q. The mass ratio is held fixed while the inclination i, the monochromatic luminosities and Ω are allowed to converge onto a test solution. Test solutions are found for values of q ranging

from 0.10 to 1.2 in increments of 0.01. For each test solution, the sum Σ of the weighted square deviations χ^2 are recorded. Typically, the mass ratio corresponds to the minimum in the resulting curve (see Figure 5.1). Results from the q-search indicate that the mass ratio $0.27 \leq q \leq 0.82$. I set the mass ratio parameter to a value near the middle of the range of values indicated by the q-search ($q = 0.60$). It is included along with the inclination i, the monochromatic luminosities and Ω in a final fitting procedure. Orbital elements of the binary system NSVS 3971593 are established from the best-fit parameters obtained. Orbital elements are reported in Table 5.1. Figures 5.2 through 5.4 show best-fit WD model fits to the observed light curve data along with the residuals.

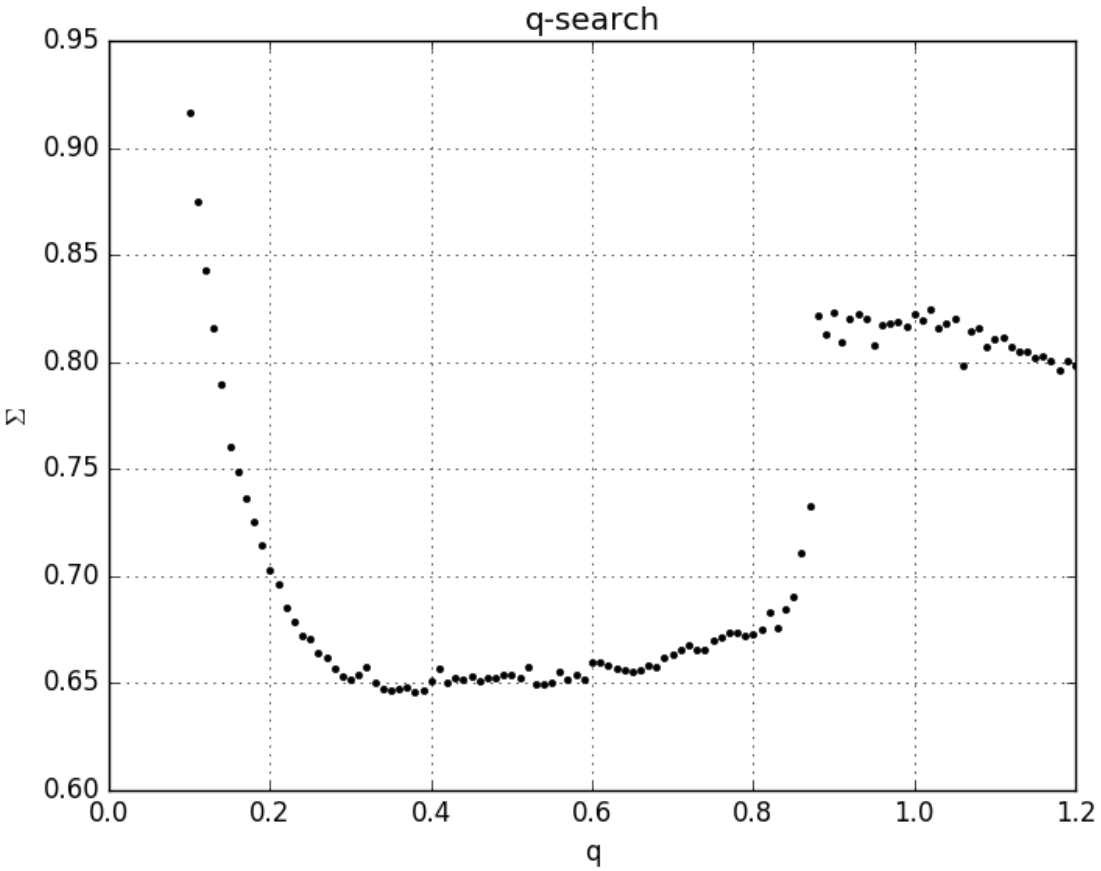

Figure 5.1: Results from the q-search indicate that the mass ratio is between $q = 0.27$ and $q = 0.82$.

A visual inspection of each light curve reveals that the observed differential magnitude

measured near the secondary minimum is less than the magnitude of the best-fit model curve. To improve the fit, a star spot is introduced to the primary stellar component. Star spot model solutions are not unique; a cool star spot on the secondary component (temperature factor $\tau_2 = \frac{T_{spot}}{T_{\rm eff}} < 1$) can have a similar effect on the shape of the light curve as that of a hot star spot on the primary component. Several spot models, each with greatly differing spot configuration are found to improve the fit. Often, I was unable to have PHOEBE converge onto a solution when any of the four star spot parameters were included (independently or simultaneously) in the fitting procedure. In these cases, spot parameters were adjusted manually, monitoring the light curve plot in between adjustments. Orbital elements established from the best-fit parameters of one of the spot models is reported in Table 5.1. Figures 5.5 through 5.7 show model fits with a star spot.

5.2 Summary for NSVS 3971593

Observed light curves have symmetric heights at max I ($\phi = 0.25$) and max II ($\phi = -0.25$). Unequal light curve maxima, known as the O'Connell effect (O'Connell 1951), is an unpredictable phenomenon (Linnell 1995) occasionally observed in the light curves of W UMa binaries. The best-fit WD model parameters reported remain uncertain without the spectroscopic data needed to establish an accurate mass ratio. Model solutions are degenerate to the observed light curves; differing solution sets within the $[i, q, \Omega]$ parameter space are equally likely to represent the orbital elements of the binary system. To further investigate the degeneracy, ten groups of B, V and R_C synthetic light curves are generated from the observed light curves with the following procedure. First, a mean light curve is generated by fitting an observed light curve with a Fourier series of 10^{th} order (Ruciński 1993). Then, a synthetic curve is generated by adding a Gaussian deviate of standard deviation equal to the photometric error of the observed data point to the mean value generated by the Fourier representation at a similar phase. For each group of synthetic light curves, solutions are

found for three randomly selected points in the $[i, q, \Omega]$ parameter space limited to q values that are consistent with the results of the q-search ($0.27 \leq q \leq 0.82$). The errors reported for the best-fit parameters in Table 5.1 reflect the standard deviation of the range of values obtained from the solutions to the ten groups of synthetic light curves. The wide range of values obtained for the mass ratio reiterate the need for spectroscopic data. Results of the modeling procedure confirm that the variable star NSVS 3971593 is an over-contact binary in thermal contact. Mass estimations combined with the mass ratio show that the primary component is more massive than the secondary component. It is an *A-type* system. Again, this assumes that binary components are main sequence stars and that the results of the q-search are reliable. The distance to the binary system and its absolute visual magnitude M_V are estimated from the best-fit parameters. (Ruciński and Duerbeck 1997) determined that the absolute visual magnitude is given by

$$M_V = -4.44 \log P + 3.02(\text{B-V})_0 + 0.12 \tag{5.1}$$

with an accuracy of ± 0.1. Using the intrinsic color index $(B - V)_0 = 0.321$, the distance modulus of the system is (m-M) $= 9.13 \pm 0.19$. After accounting for interstellar extinction $A_v = 0.200$, the distance to the system is 610 ± 50 pc.

Parameter	Symbol	Value	
(1)	(2)	(3)	(4)
Period	P_0 [days]	0.655722 ± 0.000211	0.655722 ± 0.000211
Epoch	T_0 [HJD]	$2457335.532327 \pm 0.000776$	$2457335.532327 \pm 0.000776$
Inclination	i [°]	71.72 ± 0.56	70.95 ± 0.56
Semimajor Axis	a [$R_\odot$]	4.61 ± 0.08	4.61 ± 0.08
Surface Temp.	$T_{\mathrm{eff},1,2}$ [K]	7110 ± 250	7110 ± 250
Surface Pot.	$\Omega_{1,2}$ [—]	3.242 ± 0.151	3.176 ± 0.151
Mass Ratio	q [—]	0.72 ± 0.08	0.72 ± 0.08
Luminosity	$[L_1/(L_1+L_2)]_B$	0.471 ± 0.035	0.468 ± 0.034
	$[L_1/(L_1+L_2)]_V$	0.459 ± 0.034	0.456 ± 0.033
	$[L_1/(L_1+L_2)]_{R_C}$	0.451 ± 0.033	0.447 ± 0.033
Stellar Mass	M_1 [$M_\odot$]	1.77 ± 0.09	1.77 ± 0.09
	M_2 [$M_\odot$]	1.28 ± 0.07	1.28 ± 0.07
Limb Darkening	$x_{bol,1,2}$	0.641	0.641
	$y_{bol,1,2}$	0.256	0.255
	$x_{B,1,2}$	0.784	0.782
	$y_{B,1,2}$	0.288	0.290
	$x_{V,1,2}$	0.686	0.685
	$y_{V,1,2}$	0.293	0.293
	$x_{R,1,2}$	0.588	0.588
	$y_{R,1,2}$	0.294	0.293
Spot Colatitude	ϕ_1 [°]	—	90
Spot Longitude	λ_1 [°]	—	180
Spot Radius	ϱ_1 [°]	—	35
Temp. Factor	τ_1 [—]	—	1.03

Table 5.1: Model Parameters for NSVS 3971593 (*column1*) determined by the best-fit WD model with symbols (*column 2*). Some parameters specify the primary with the number 1 and the seconday with the number 2. Values are for the best-fit stellar model without a stellar spot (*column 3*) and with a stellar spot (*column 4*).

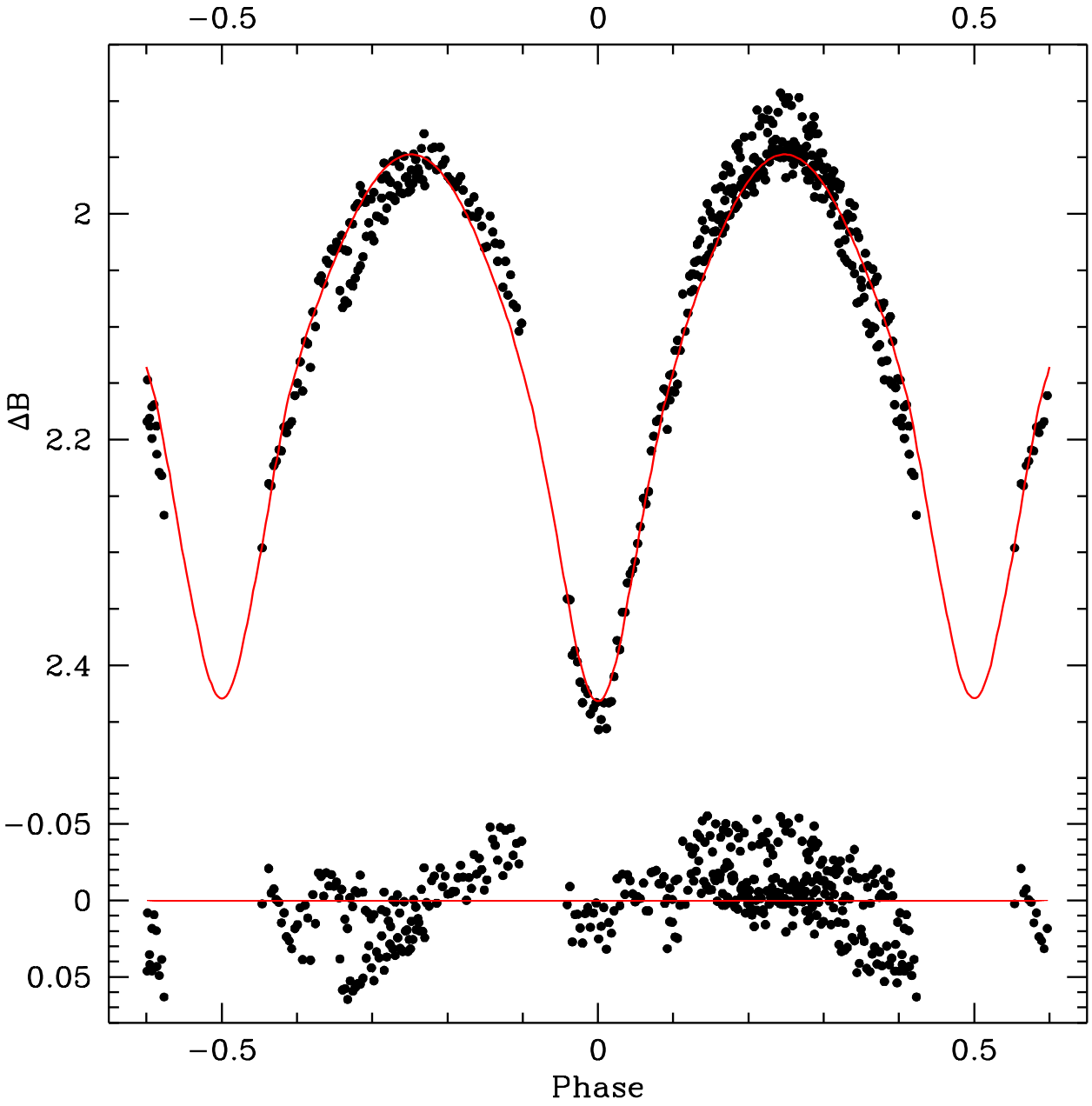

Figure 5.2: Best-fit WD model fit without spot (*solid line*) to the folded light curve for differential Johnson B band magnitudes (*top panel*). The best-fit orbital parameters are listed in Table 5.1. The *bottom panel* shows residuals from the best-fit model (*solid curve*). Error bars are omitted from the points for clarity.

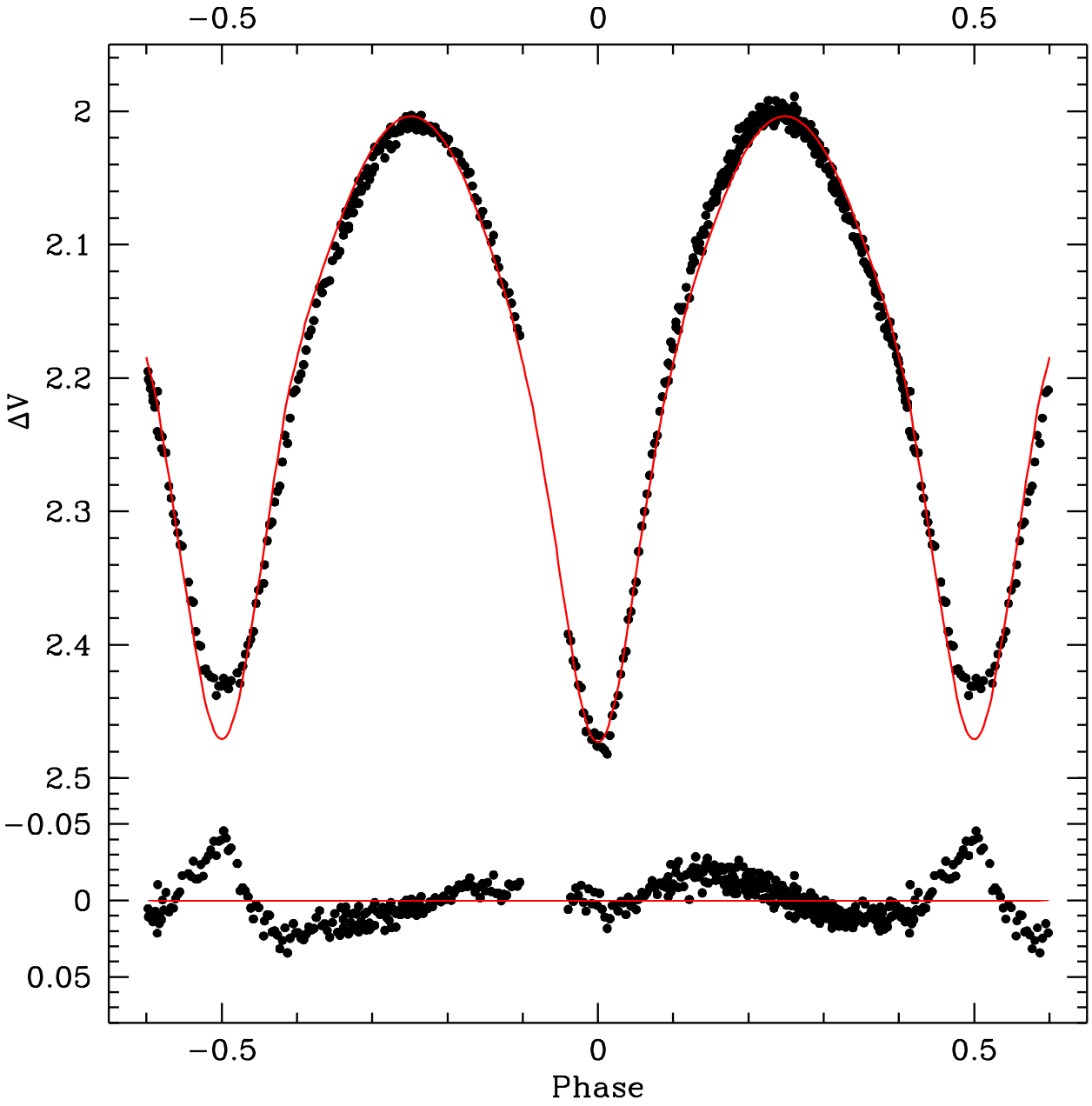

Figure 5.3: Best-fit WD model fit without spot (*solid line*) to the folded light curve for differential Johnson V band magnitudes (*top panel*). The best-fit orbital parameters are listed in Table 5.1. The *bottom panel* shows residuals from the best-fit model (*solid curve*). Error bars are omitted from the points for clarity.

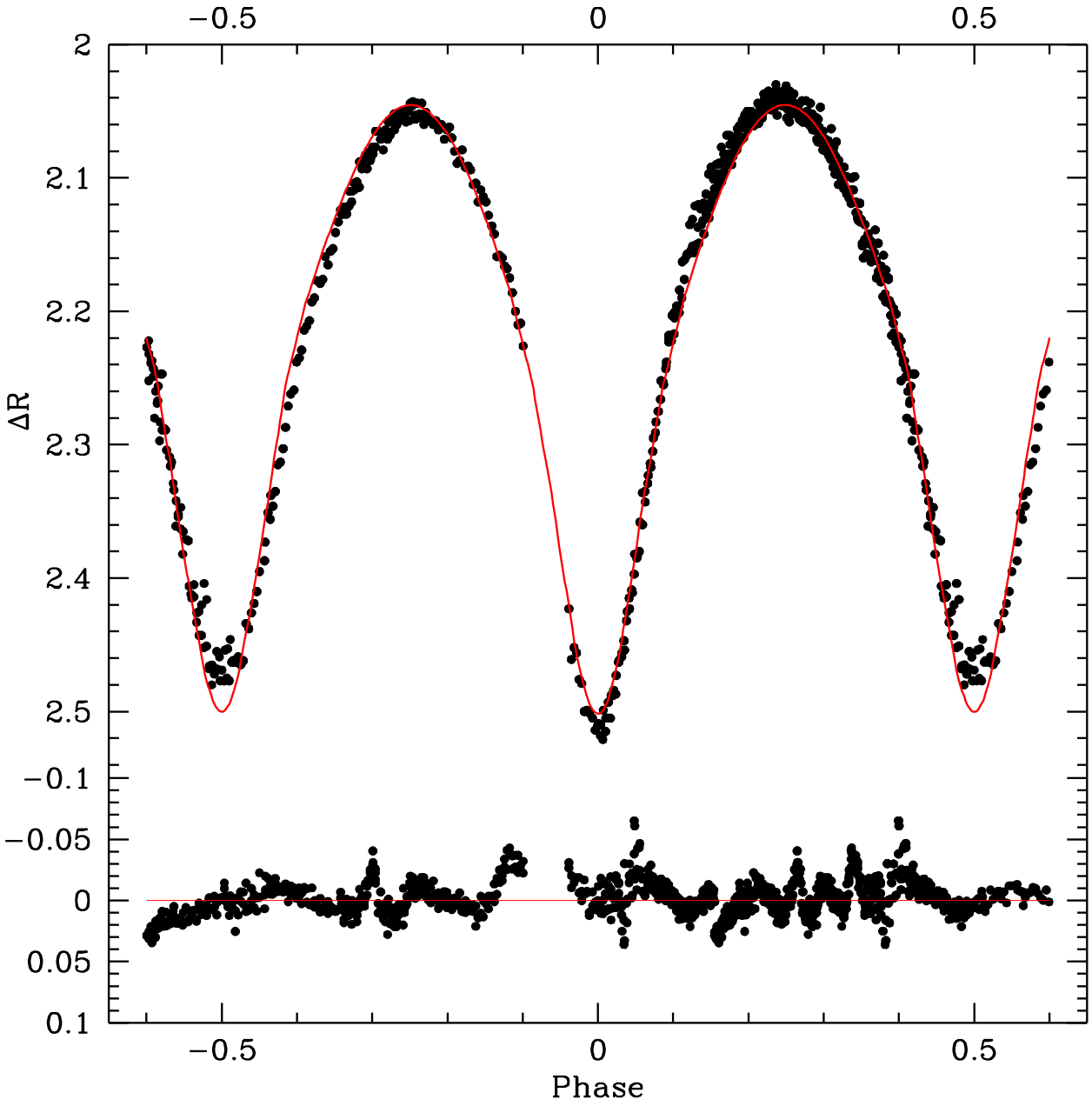

Figure 5.4: Best-fit WD model fit without spot (*solid line*) to the folded light curve for differential Cousins R band magnitudes (*top panel*). The best-fit orbital parameters are listed in Table 5.1. The *bottom panel* shows residuals from the best-fit model (*solid curve*). Error bars are omitted from the points for clarity.

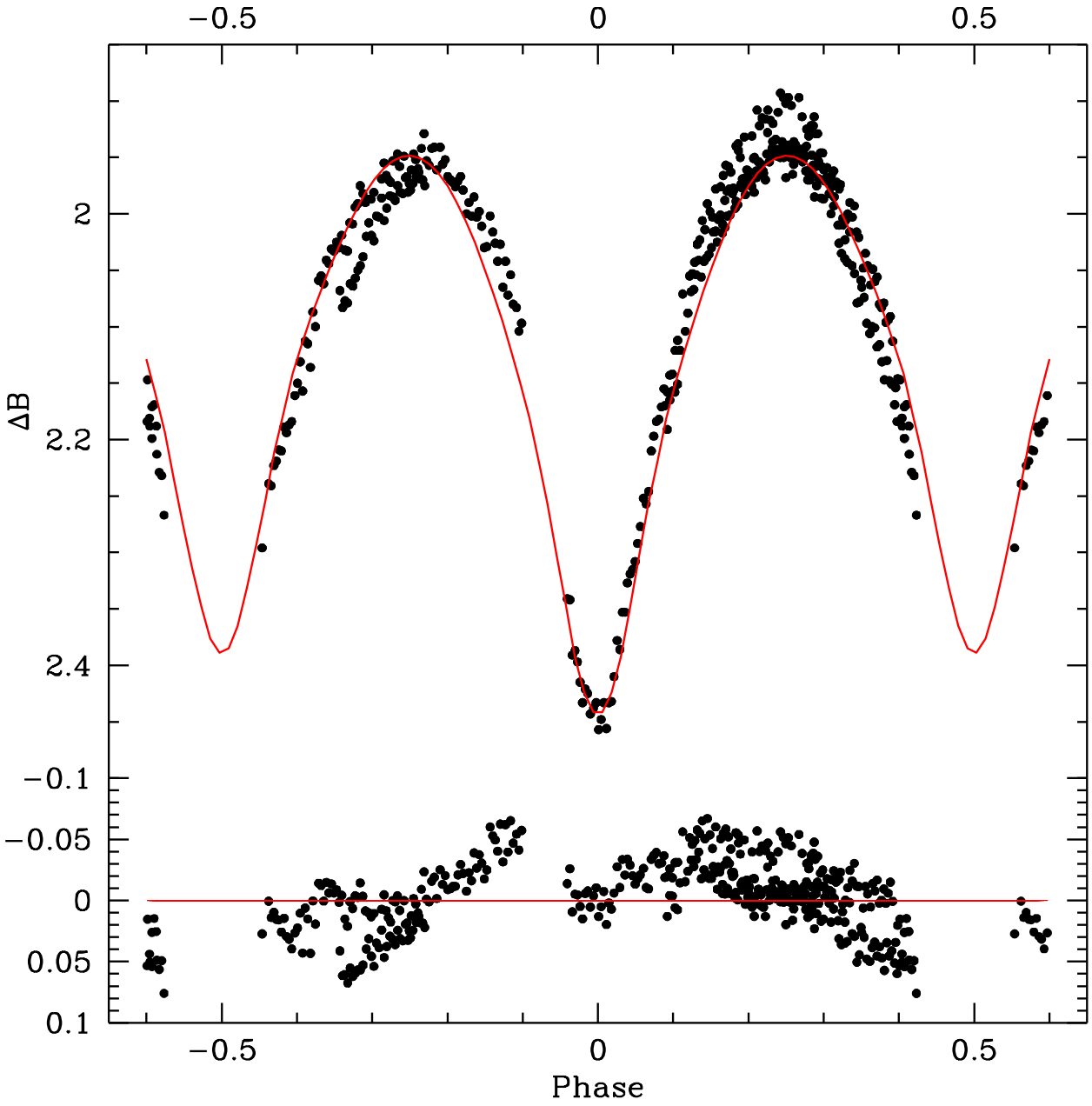

Figure 5.5: Best-fit WD model fit with spot (*solid line*) to the folded light curve for differential Johnson B band magnitudes (*top panel*). The best-fit orbital parameters are listed in Table 5.1. The *bottom panel* shows residuals from the best-fit model (*solid curve*). Error bars are omitted from the points for clarity.

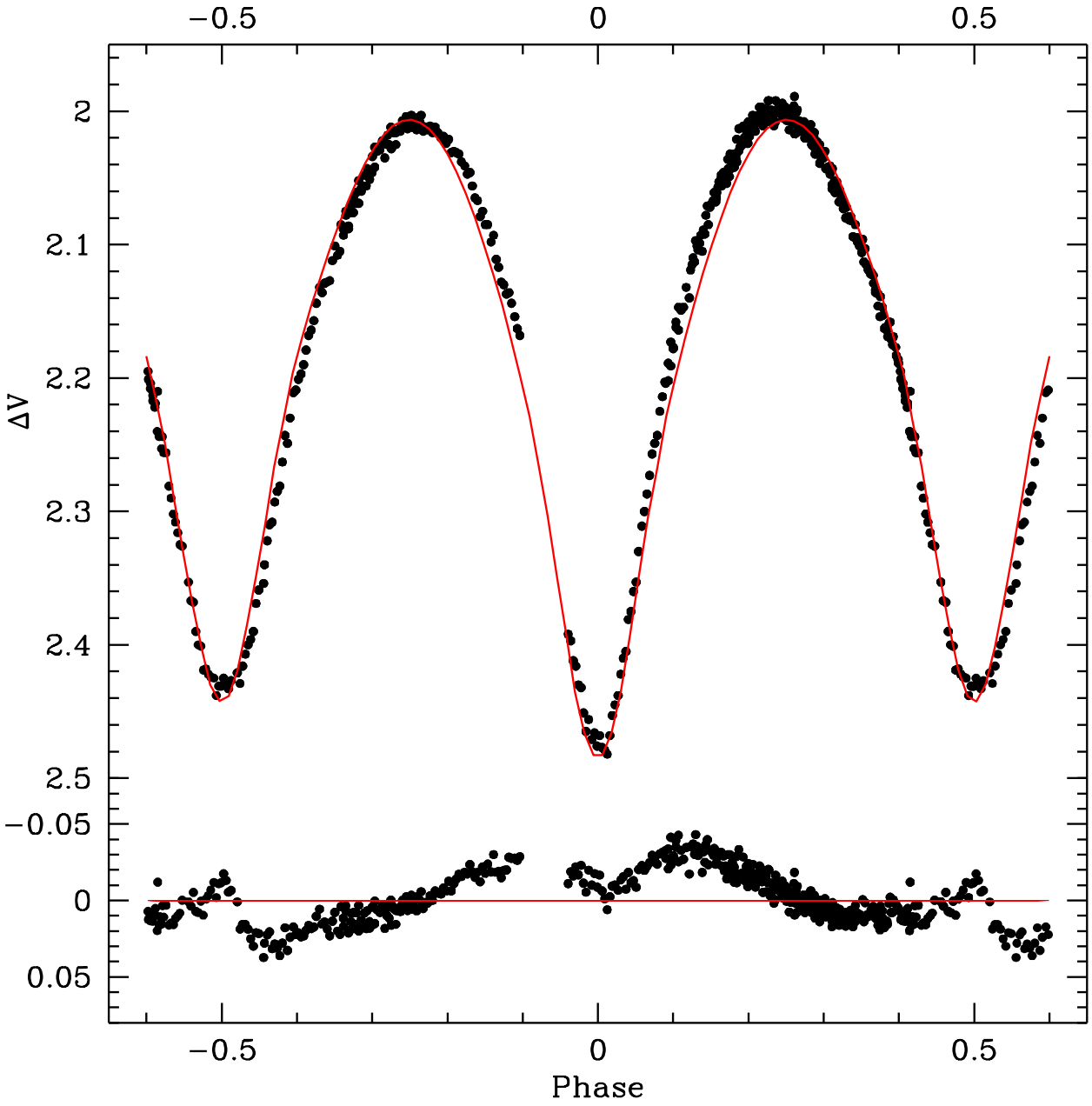

Figure 5.6: Best-fit WD model fit with spot (*solid line*) to the folded light curve for differential Johnson V band magnitudes (*top panel*). The best-fit orbital parameters are listed in Table 5.1. The *bottom panel* shows residuals from the best-fit model (*solid curve*). Error bars are omitted from the points for clarity.

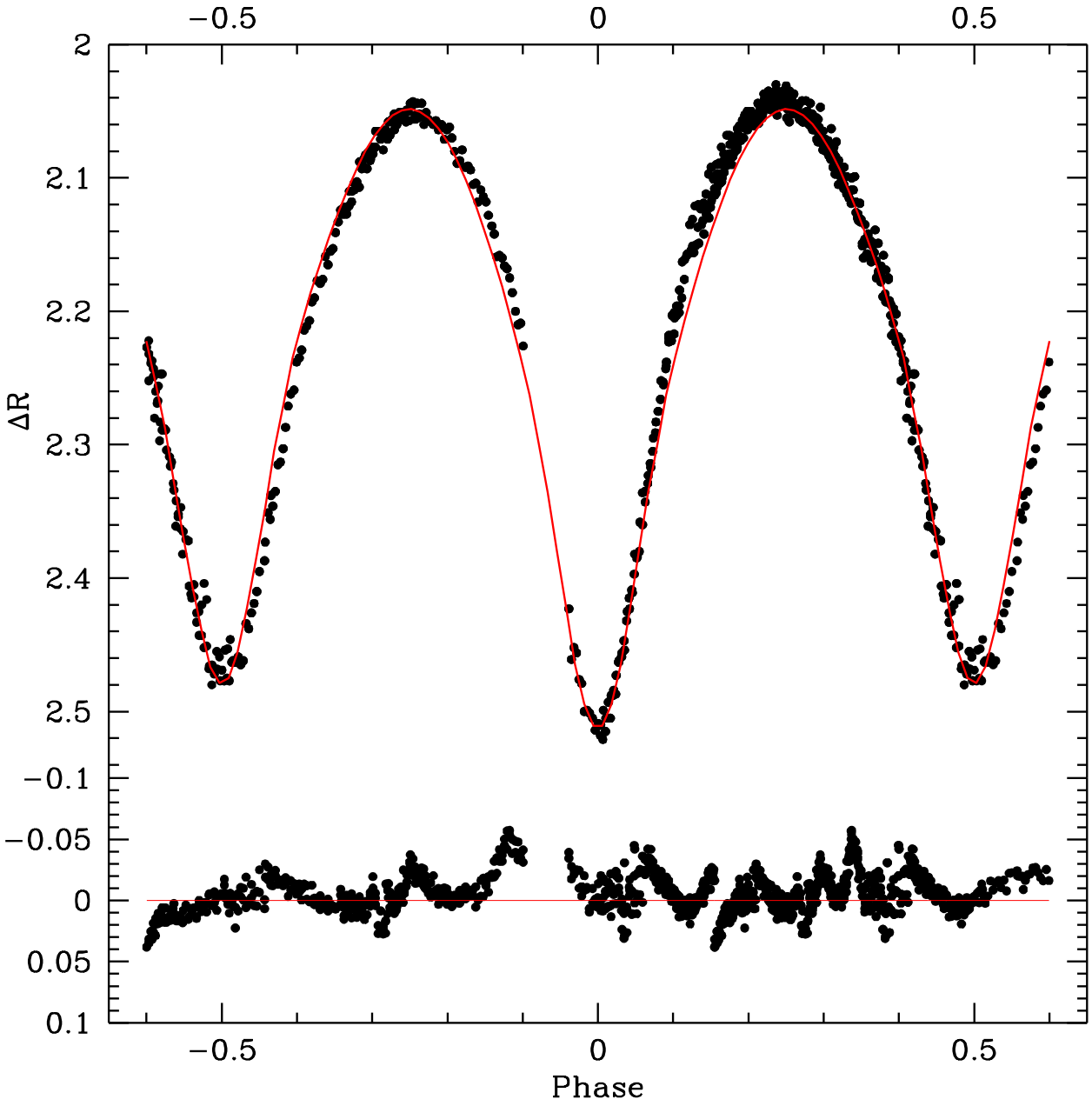

Figure 5.7: Best-fit WD model fit with spot (*solid line*) to the folded light curve for differential Cousins R band magnitudes (*top panel*). The best-fit orbital parameters are listed in Table 5.1. The *bottom panel* shows residuals from the best-fit model (*solid curve*). Error bars are omitted from the points for clarity.

Chapter 6

W Ursae Majoris type variable star NSVS 7680691

The star NSVS 7680691 [=2MASS J13371227+2134088, R. A. = $13^h37^m12.276^s$, Dec. = $+21°34'8.8''$, J2000.0] was found to be a variable star using photometric data from the NSVS (Woźniak 2004). Afterwards, Hoffman *et al* (2009) classified it as a W UMa type variable star and reported an orbital period of $P = 0.31631$ days. This was later confirmed by A. J. Drake *et al* (2014) who reported $P = 0.316306$ days. My observations of NSVS 7680691 span over 29 days in March and April of 2016. Over 2/3 of the data were taken in a span of 5 days. On seven nights a total of 1324 images were taken in three bandpass filters: Johnson B, Johnson V and Cousins R (R_C). Images were reduced with IRAF (Tody 1993). Period analysis with PERANSO software (CBA Belgium Observatory 2011) yields an orbital period $P = 0.273007 \pm 0.000060$ days. This is 13.7% shorter than that reported by Hoffman *et al* and A. J. Drake *et al*. Light curves are generated with differential photometry. Johnson B and Johnson V instrumental differential magnitudes are combined with the known calibrated Johnson B and Johnson V magnitudes of the comparison star TYC 1465-809-1 to produce apparent magnitudes for NSVS 7680691. Effective temperature and spectral type are estimated from the $(B - V)$ color index measured at orbital quadrature ($\Phi = \pm 0.25$).

The observed value $(B-V) = 0.675 \pm 0.018$ is corrected using the extinction coefficient $E(B-V) = 0.014$ from Schlafly & Finkbeiner (2011) at the galactic coordinates for the binary star. The resulting intrinsic color index $(B-V)_0 = 0.661 \pm 0.018$ indicates a spectral type G4 (Fitzgerald 1970) and an effective temperature of $T_{\rm eff} = 5669 \pm 120$ K (Flower 1996). If NSVS 7680691 is assumed to be a normal main sequence star, Equation 4 of Harmanec (1988) estimates the stellar mass to be $M_\star = 1.06 \pm 0.02$ $M_\odot$. With this mass estimate, Kepler's Harmonic law (see Equation 1.1) gives the semi-major axis $a = 2.27 \pm 0.01$ $R_\odot$.

6.1 New Orbital Period

I accept the orbital period determined by my investigation notwithstanding it is inconsistent with that reported by Hoffman *et al* and A. J. Drake *et al*. The period analysis software PERANSO (CBA Belgium Observatory 2011) employs a method presented by A. Schwartzenberg and Czerny (1995) that uses periodic orthogonal polynomials to fit observed light curves. The method searches through a range of trial orbital periods $P_{min} \leq P \leq P_{max}$ specified by the user. The analysis of variance (ANOVA) statistic $\Theta(P)$ evaluates the quality of the fit. A higher value of $\Theta(P)$ indicates that P is a better fit and more likely to be the orbital period. A plot of $\Theta(P)$ versus orbital period P shows three significant peaks (see Figure 6.1). The orbital period reported in my investigation $P = 0.273007 \pm 0.000060$ corresponds to the highest peak $\Theta(P) \approx 355$. The smaller peaks ($\Theta(P) \approx 190$) are found at $P \approx 0.240$ and $P \approx 0.316$, the latter of which corresponds to the orbital period determined by Hoffman *et al* and A. J. Drake *et al*. The best-fit orbital period determined by PERANSO is confirmed using phase dispersion minimization (Stellingwerf 1978) via the `pdm` task in IRAF. In this alternate period analysis software, the same range of trial orbital periods is searched. Results indicate that the most probable orbital period is $P = 0.273081$ followed by $P = 0.315945$. Figure 6.2 shows a comparison of differential Johnson V magnitudes from my investigation folded over different orbital periods. The top panel shows magnitudes folded

over the orbital period determined by Hoffman *et al* and A. J. Drake *et al*. The bottom panel shows magnitudes folded over the orbital period reported in my investigation.

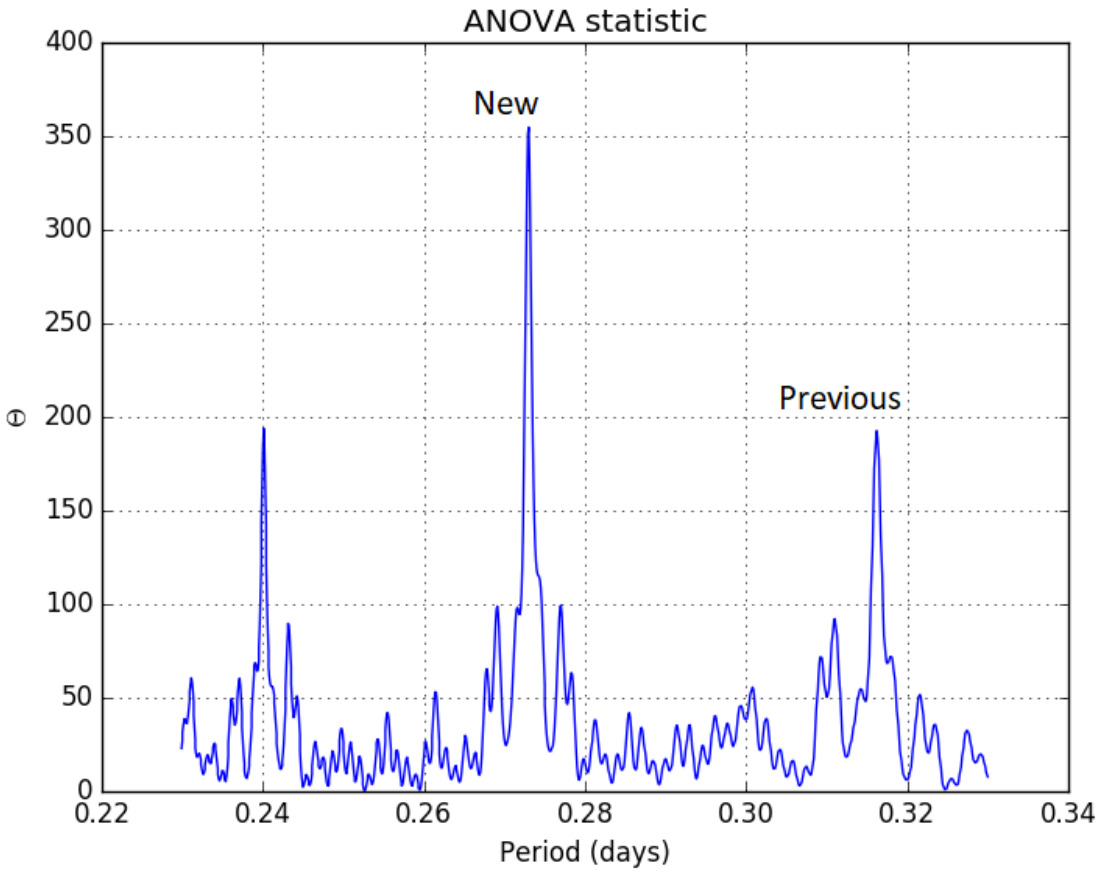

Figure 6.1: Analysis of Variance (ANOVA) statistic Θ versus period P for NSVS 7680691.The new orbital period is the best-fit period $P = 0.272987 \pm 0.0002$ (*middle peak*) determined by this investigation. The previous orbital period is indicated. Plot shows minor significance in $P = 0.316273 \pm 0.0005$ (*right peak*).

6.2 WD model

The PHOEBE modeling package (Prša & Zwitter 2005) is used to establish orbital parameters of eclipsing binary system NSVS 7680691. All three folded light curves, Johnson B, Johnson V and Cousins R_C are fit simultaneously. The binary system is assumed to be an over-contact binary of the W UMa type. The initial model constraint is set accordingly.

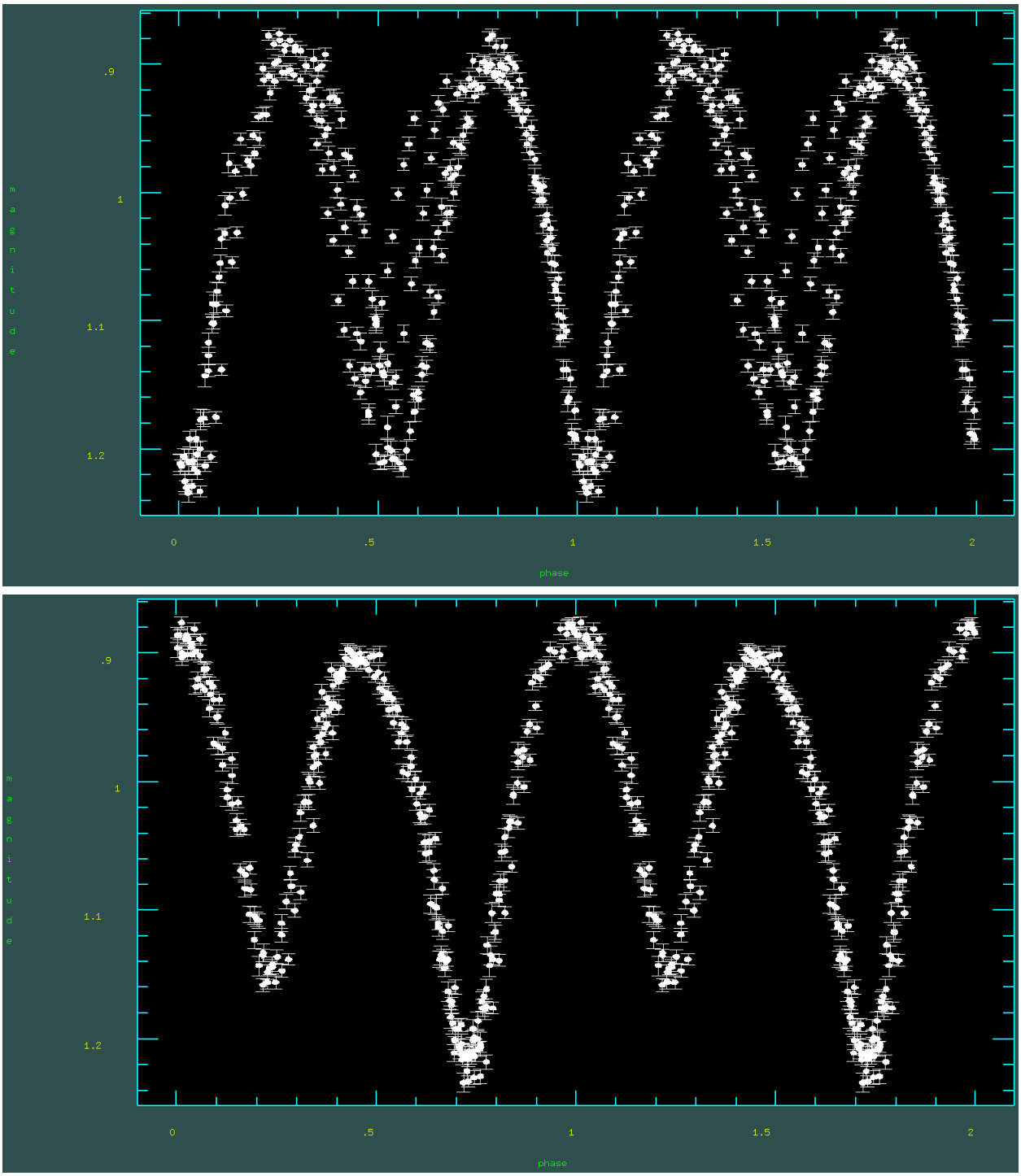

Figure 6.2: Display from the `pdm` task in IRAF. Johnson V magnitudes folded over the orbital period determined by Hoffman *et al* and A. J. Drake *et al* (*top panel*). Johnson V magnitudes folded over the orbital period determined by my investigation (*bottom panel*).

The outer envelopes of the binary star are assumed to be convective; the gravity brightening coefficients β_1 (primary) and β_2 (secondary) defined by $F_{\text{surf}} \propto g^{\beta}$ (see Equation 1.12) are set to 0.32 (Lucy 1967). Values for the epoch T_0, orbital period P and effective temperature T_{eff} are entered in the parameters section. The bolometric albedo of each stellar component A_1 and A_2 is set to 0.5 as suggested by Ruciński (1969). Limb Darkening coefficients are interpolated with the logarithmic law using van Hamme (1993) tables. The reflection effect is optioned with two possible reflections. A crude initial fit is made using the initial default values for the monochromatic luminosities and surface potential Ω. Once the initial fit cannot be improved with further iterations, the orbital inclination i and mass ratio q parameters, with initial values $i = 80°$ and $q = 1.00$, are selected to be included in the fitting procedure.

Without radial velocity data, it is not possible to unequivocally determine the mass ratio q (Alton 2016). A q-search method is used to establish the mass ratio q. The mass ratio is held fixed while the inclination i, the monochromatic luminosities and Ω are allowed to converge onto a test solution. Test solutions are found for values of q ranging from 0.52 to 4.30. For each test solution, the cost function is recorded. The cost function is a statistical value that PHOEBE calculates directly from flux values of the observed light curves and the sum of the weighted deviations χ^2. The cost function conveys the quality of the model fit, a lower value indicates a better fit. For convenience, I use it for the q-search instead of χ^2. The resulting curve (see Figure 6.3) sets the lower limit of the mass ratio to $q = 0.52$. Solutions with the mass ratio $q < 0.52$ were not obtainable or unrealistic. The q-search fails to indicate the subclass (*A-type* or *W-type*). In general, A-type W UMa variables can be characterized by their total mass ($M_T > 1.8 M_{\odot}$), spectral class (A-F) and orbital period ($P > 0.4 days$) (Alton 2016). Based on the spectral type (G4) and the orbital period ($P = 0.273007 \pm 0.000060$) observed, NSVS 7680691 appears to belong to the W-type subclass. In the W-type subclass, the primary component is less massive than its companion. The mass ratio parameter is set to $q = 1.00$ and is included along with the inclination i, the monochromatic luminosities and Ω in a final fitting procedure. Orbital elements of the

binary system NSVS 7680691 are established from the best-fit parameters obtained. Orbital elements are reported in Table 6.1. Figures 6.4 through 6.6 show best-fit WD model fits to the observed light curve data along with the residuals.

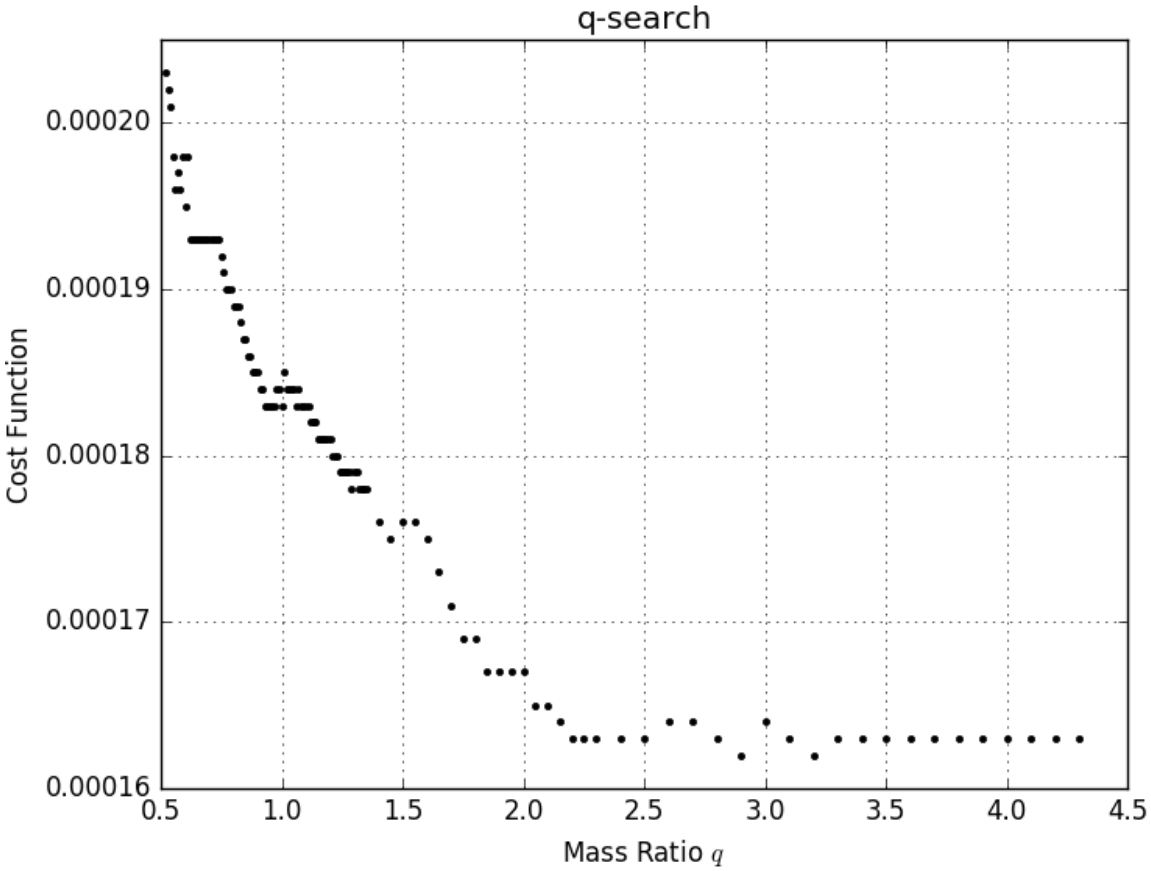

Figure 6.3: Results from the q-search are inconclusive. Radial velocity data is needed to determine the mass ratio q.

A visual inspection of each light curve reveals that the observed differential magnitude measured near the secondary minimum is less than the magnitude of the best-fit model curve. To improve the fit, a star spot is introduced to the primary stellar component. Several spot models, each with greatly differing spot configurations are found to improve the fit. Often, I was unable to have PHOEBE converge onto a solution when any of the four star spot parameters were included (independently or simultaneously) in the fitting procedure. In these cases, spot parameters were adjusted manually, monitoring the light curve plot in

between adjustments. Orbital elements established from the best-fit parameters of one of the spot models is reported in Table 6.1. Figures 6.7 through 6.9 show model fits with a star spot.

6.3 Summary for NSVS 7680691

Observed light curves have equal heights at max I ($\phi = 0.25$) and max II ($\phi = -0.25$). Unequal light curve maxima, known as the O'Connell (1951) effect, is an unpredictable phenomenon (Linnell 1991) occasionally observed in the light curves of W UMa binaries. The best-fit WD model parameters reported remain uncertain without the spectroscopic data needed to establish an accurate mass ratio. Model solutions are degenerate to the observed light curves; differing solution sets within the $[i, q, \Omega]$ parameter space are equally likely to represent the orbital elements of the binary system. To further investigate the degeneracy, ten groups of B, V and R_C synthetic light curves are generated from the observed light curves with the following procedure. First, a mean light curve is generated by fitting an observed light curve with a Fourier series of 10^{th} order (Ruciński 1993). Then, a synthetic curve is generated by adding a Gaussian deviate of standard deviation equal to the photometric error of the observed data point to the mean value generated by the Fourier representation at a similar phase. For each group of synthetic light curves, solutions are found for three randomly selected points in the $[i, q, \Omega]$ parameter space. The errors reported for the best-fit parameters in Table 6.1 reflect the standard deviation of the range of values obtained from the solutions to the ten groups of synthetic light curves. The wide range of values obtained for the mass ratio reiterate the need for spectroscopic data. Results of the modeling procedure confirm that the variable star NSVS 7680691 is an over-contact binary in thermal contact. Mass estimations combined with the mass ratio show that the primary component is more massive than the brighter primary component. It appears to be a *W-type* system. The distance to the binary system and its absolute visual magnitude M_V are estimated from

the best-fit parameters. (Ruciński and Duerbeck 1997) determined that the absolute visual magnitude is given by Equation 5.1. Using the intrinsic color index $(B-V)_0 = 0.661$, the distance modulus of the system is (m-M) $= 7.63 \pm 0.06$. After accounting for interstellar extinction $A_v = 0.044$, the distance to the system is 329 ± 10 pc.

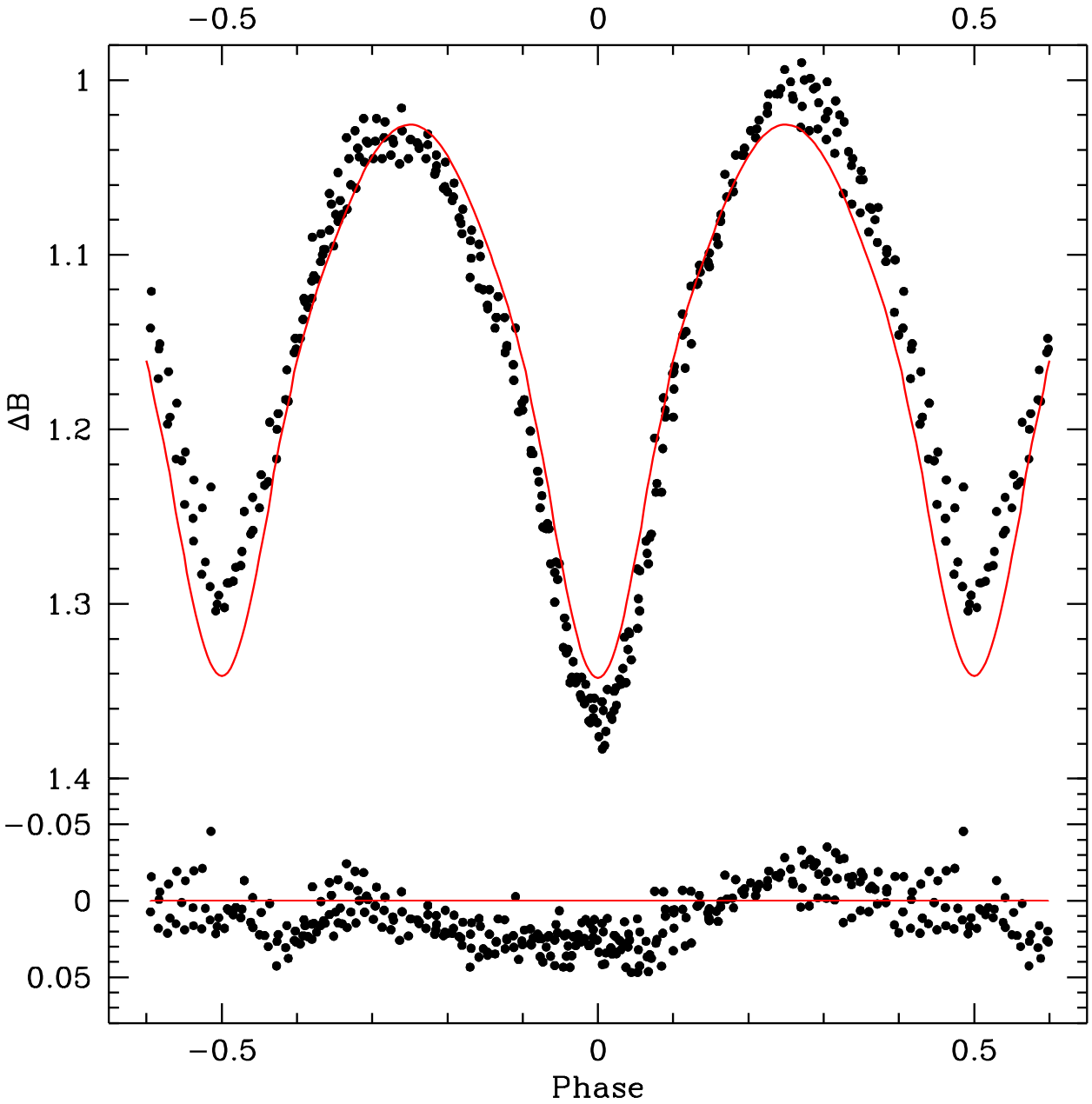

Figure 6.4: Best-fit WD model fit without spot (*solid line*) to the folded light curve for differential Johnson B band magnitudes (*top panel*). The best-fit orbital parameters are listed in Table 6.1. The *bottom panel* shows residuals from the best-fit model (*solid curve*). Error bars are omitted from the points for clarity.

Model Parameters for NSVS 7680691

Parameter	Symbol	Value	
(1)	(2)	(3)	(4)
Period	P_0 [days]	0.273007 ± 0.000060	0.273007 ± 0.000060
Epoch	T_0 [HJD]	$2457474.744624 \pm 0.000538$	$2457474.744624 \pm 0.000538$
Inclination	i [°]	63.31 ± 0.31	63.56 ± 0.31
Semimajor Axis	a [$R_\odot$]	2.27 ± 0.03	2.27 ± 0.03
Surface Temp.	$T_{\rm eff,1,2}$ [K]	5669 ± 120	5669 ± 120
Surface Pot.	$\Omega_{1,2}$ [—]	3.650 ± 0.125	3.69 ± 0.125
Mass Ratio	q [—]	0.95 ± 0.08	0.96 ± 0.08
Luminosity	$[L_1/(L_1+L_2)]_B$	5.36 ± 0.03	0.395 ± 0.026
	$[L_1/(L_1+L_2)]_V$	6.12 ± 0.03	0.426 ± 0.026
	$[L_1/(L_1+L_2)]_{R_C}$	6.73 ± 0.03	0.450 ± 0.029
Stellar Mass	M_1 [$M_\odot$]	1.09 ± 0.04	1.08 ± 0.04
	M_2 [$M_\odot$]	1.03 ± 0.04	1.04 ± 0.04
Limb Darkening	$x_{bol,1,2}$	0.646,0.644	0.646,0.644
	$y_{bol,1,2}$	0.203,0.221	0.203,0.221
	$x_{B,1,2}$	0.840,0.827	0.840,0.827
	$y_{B,1,2}$	0.126,0.180	0.126,0.180
	$x_{V,1,2}$	0.766,0.744	0.766,0.744
	$y_{V,1,2}$	0.223,0.256	0.223,0.256
	$x_{R,1,2}$	0.675,0.651	0.675,0.651
	$y_{R,1,2}$	0.246,0.268	0.246,0.268
Spot Colatitude	ϕ_1 [°]	—	90
Spot Longitude	λ_1 [°]	—	180
Spot Radius	ϱ_1 [°]	—	30
Temp. Factor	τ_1 [—]	—	1.05

Table 6.1: Model Parameters for NSVS 7680691 (*column1*) determined by the best-fit WD model with symbols (*column 2*). Some parameters specify the primary with the number 1 and the secondary with the number 2. Values are for the best-fit stellar model without a stellar spot (*column 3*) and with a stellar spot (*column 4*).

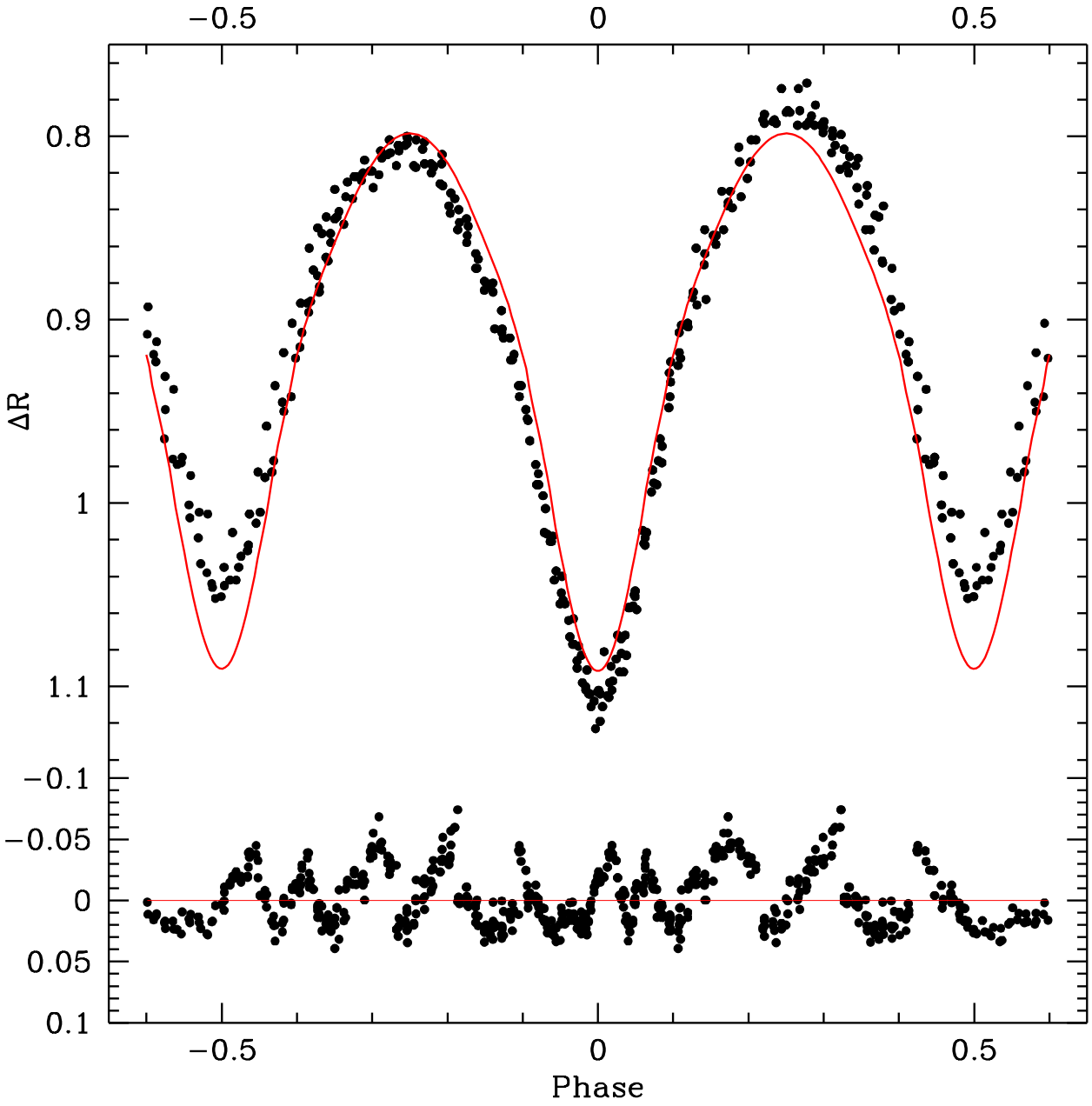

Figure 6.5: Best-fit WD model fit without spot (*solid line*) to the folded light curve for differential Cousins R band magnitudes (*top panel*). The best-fit orbital parameters are listed in Table 6.1. The *bottom panel* shows residuals from the best-fit model (*solid curve*). Error bars are omitted from the points for clarity.

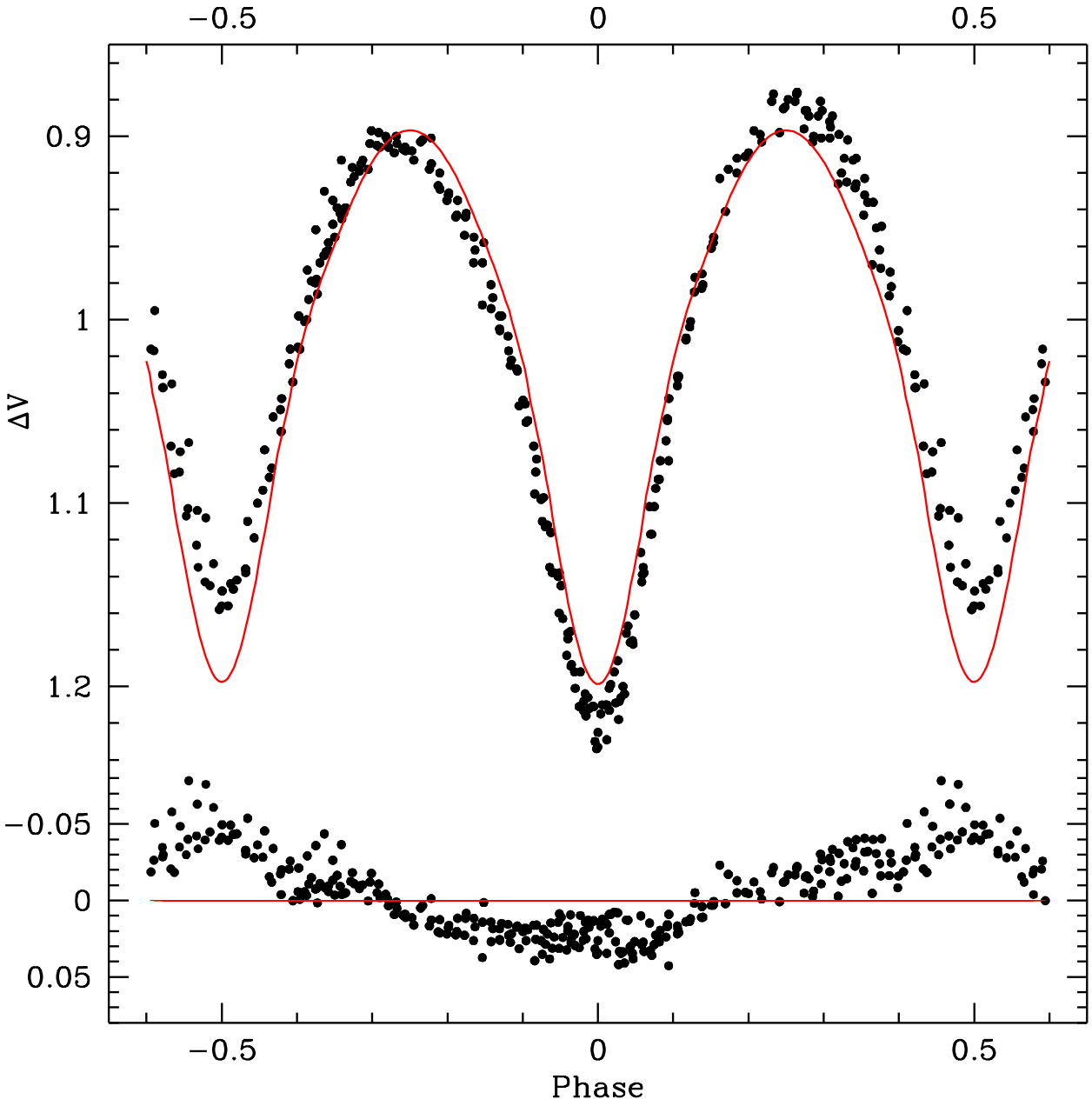

Figure 6.6: Best-fit WD model fit without spot (*solid line*) to the folded light curve for differential Johnson V band magnitudes (*top panel*). The best-fit orbital parameters are listed in Table 6.1. The *bottom panel* shows residuals from the best-fit model (*solid curve*). Error bars are omitted from the points for clarity.

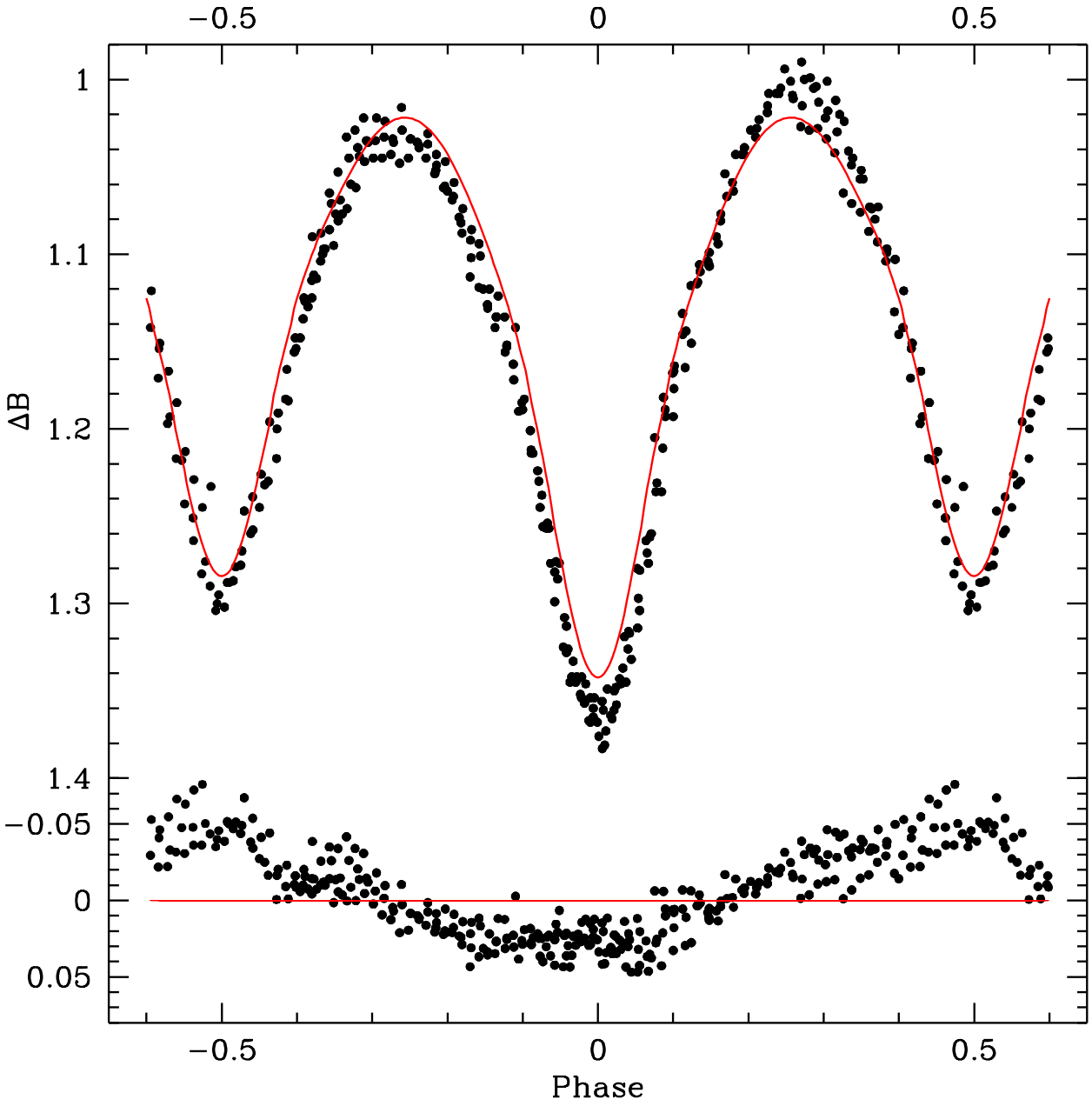

Figure 6.7: Best-fit WD model fit with spot (*solid line*) to the folded light curve for differential Johnson B band magnitudes (*top panel*). The best-fit orbital parameters are listed in Table 6.1. The *bottom panel* shows residuals from the best-fit model (*solid curve*). Error bars are omitted from the points for clarity.

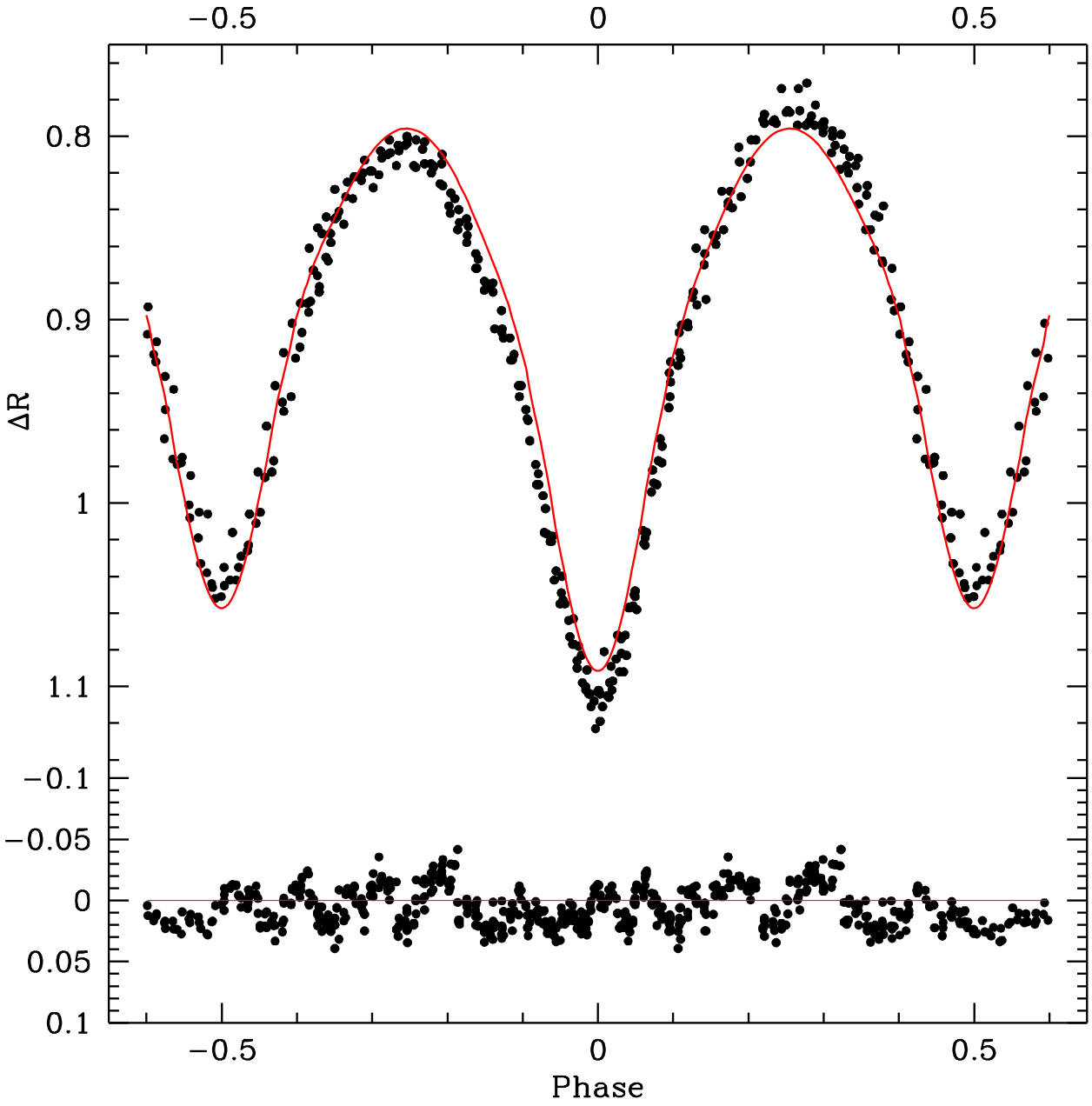

Figure 6.8: Best-fit WD model fit with spot (*solid line*) to the folded light curve for differential Cousins R band magnitudes (*top panel*). The best-fit orbital parameters are listed in Table 6.1. The *bottom panel* shows residuals from the best-fit model (*solid curve*). Error bars are omitted from the points for clarity.

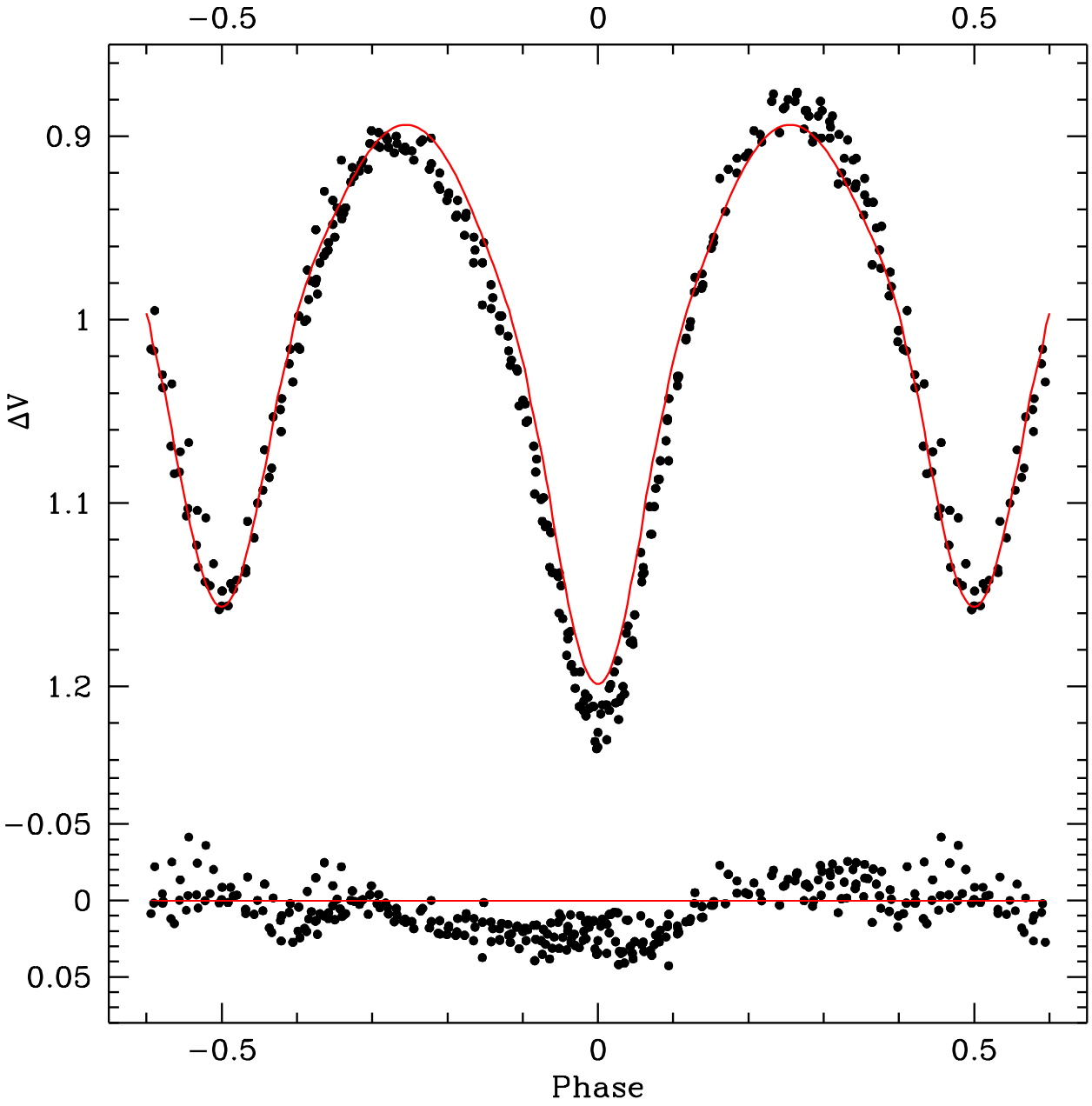

Figure 6.9: Best-fit WD model fit with spot (*solid line*) to the folded light curve for differential Johnson V band magnitudes (*top panel*). The best-fit orbital parameters are listed in Table 6.1. The *bottom panel* shows residuals from the best-fit model (*solid curve*). Error bars are omitted from the points for clarity.

Chapter 7

Conclusion

The selected variable stars NSVS 3971593 and NSVS 7680691 are both confirmed to be W UMa over-contact binaries. Effective surface temperatures and spectral class are determined from the observed intrinsic color index. NSVS 3971593 is a F0 spectral type (Fitzgerald 1970) and the orbital period of the binary system determined in this investigation confirms the value reported by Hoffman *et al* (2009). I determine the eclipse reported in the BAV results for NSVS 3971593 to be a secondary eclipse. NSVS 7680691 is a G4 spectral type. The orbital period determined in this investigation contradicts that reported by Hoffman*et al* (2009) and A. Drake *et al* (2014). The visual magnitude amplitude observed in this investigation is approximately 50% larger than that reported by A. Drake *et al* (2014). Orbital elements established for each binary system are determined with PHOEBE software (CBA Belgium Observatory 2011). Due to the lack of spectroscopic (radial velocity) data, values reported for mass ratio q and effective potential Ω remain uncertain. Each binary system is assumed to be composed of normal main sequence stars. Under this assumption, stellar mass estimates following Harmanec (1988) combined with the photometrically determined mass ratio suggest that NSVS 3971593 belongs to the A-type subclass. In A-type contact systems, the hotter, brighter star is also more massive than its companion (Kallrath & Milone 2009). NSVS 7680691 appears to be a W-type contact system based on the ob-

served orbital period and spectral class. The semi-major axis a for each binary system is determined via Kepler's Harmonic law (see Equation 1.1). The PHOEBE software provides graphical plots of the binary systems. Morphological representations of the best-fit spot model for each system are shown in Figure 7.1 and Figure 7.2. This study provides a preliminary model of the selected binary systems but further spectroscopic studies are needed to validate the orbital elements established by this investigation.

This investigation has been and continues to be a tremendous learning experience. A significant portion of my work was invested into the photometry process, specifically, learning to use IRAF (Tody 1993). About one third of my observational data was found to be unusable due to atmospheric conditions (clouds). The problem could of have been avoided by increasing the exposure lengths for the images. Another solution may be to correct star brightness variations caused by variations in atmospheric transparency by using a method similar to the one presented by Chang *et al* (2015). This method removes systematic variations shared by light curves of nearby stars, while true variabilities are preserved. Although I am interested in using a better method, I would expect only marginal improvements in the quality of the generated light curves. In retrospect, I should have taken better data. With longer exposure times, I believe I could achieve better results from the modeling process. I plan to further develop the computer program I wrote for calculating differential magnitudes. An algorithm that uses ensembles of comparison stars as described by Honeycutt (1992) will be incorporated into the differential photometry computation.

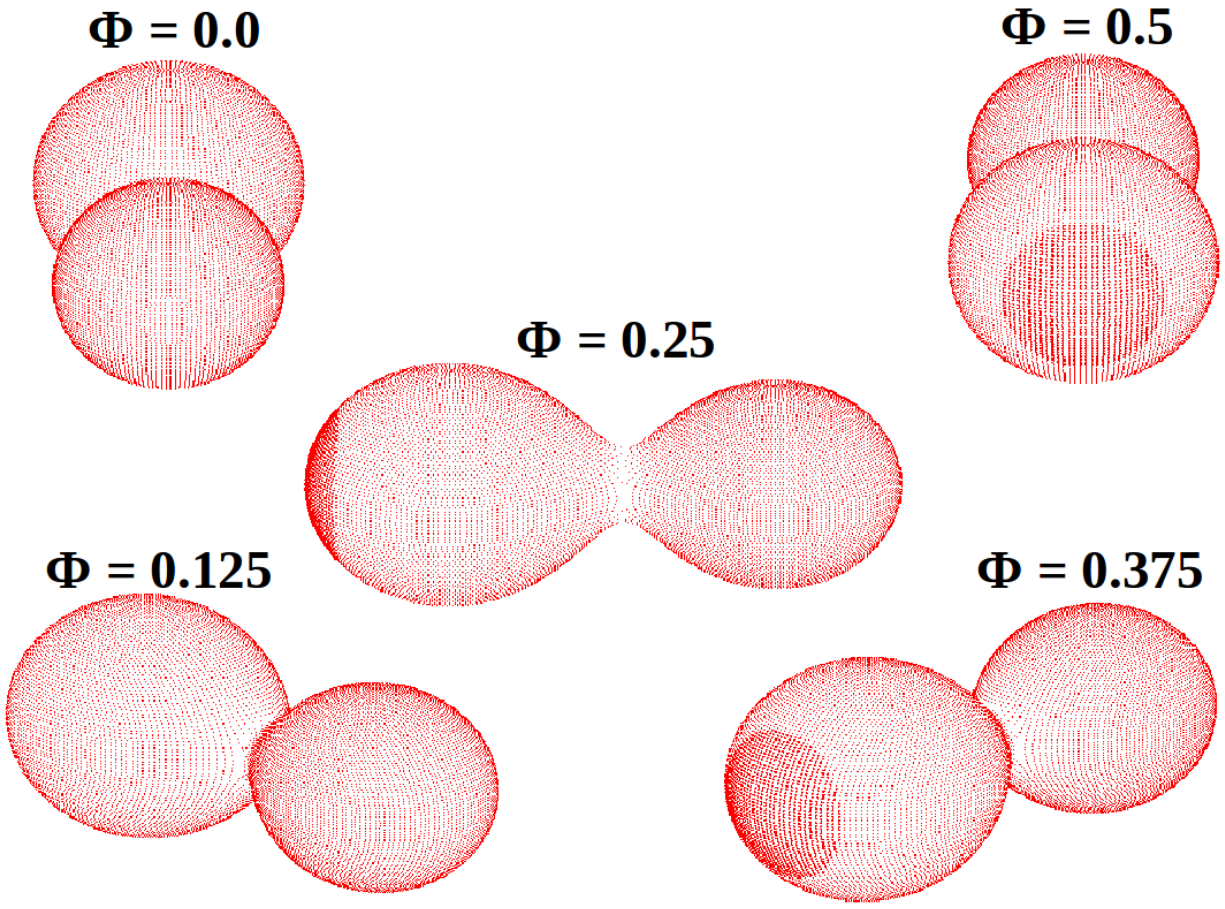

Figure 7.1: Morphological representation of the best-fit WD spot model fit for NSVS 3971593. Corresponding orbital phase is given in each panel. The darker region of the stellar surface is the stellar spot.

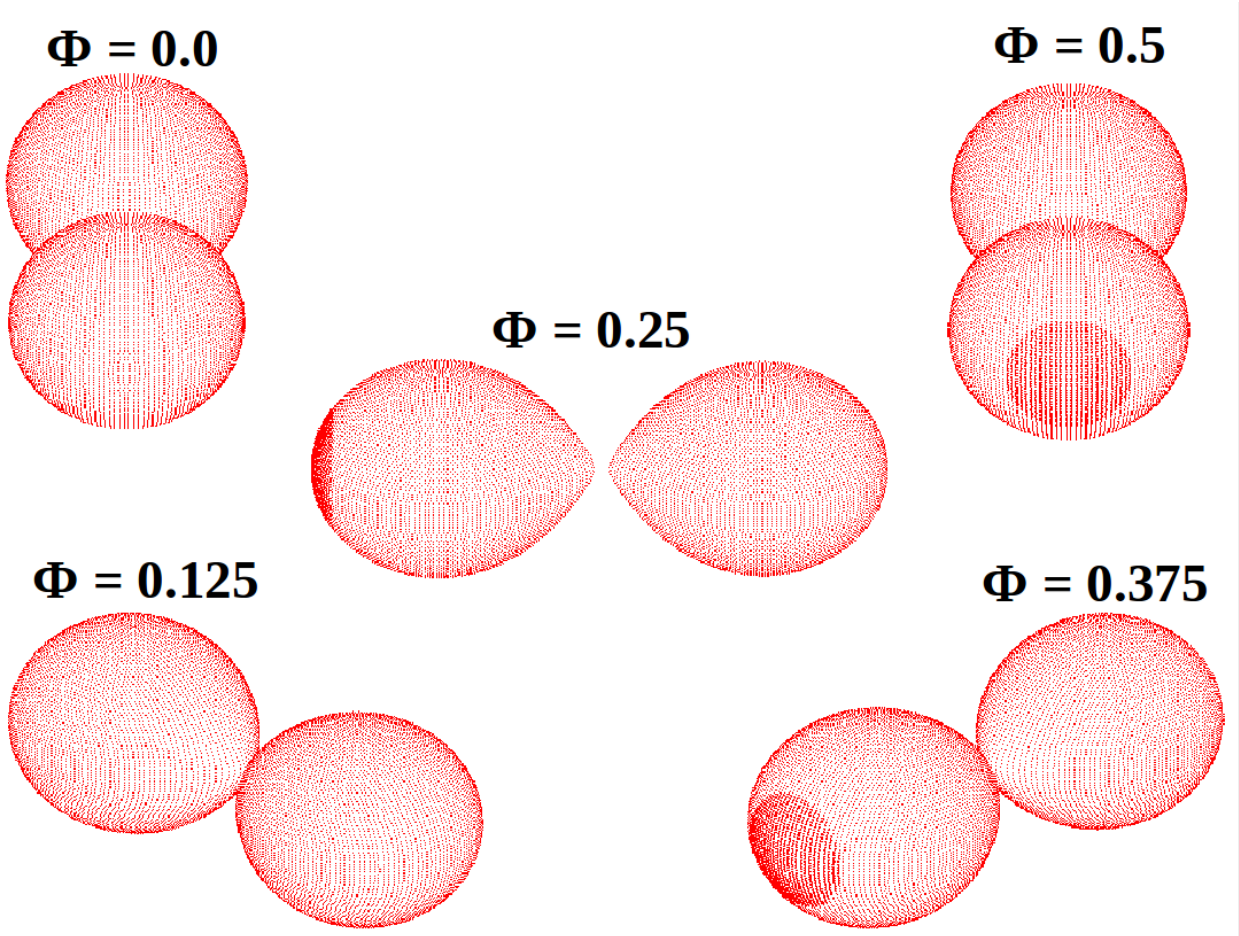

Figure 7.2: Morphological representation of the best-fit WD spot model fit for NSVS 7680691. Corresponding orbital phase is given in each panel. The darker region of the stellar surface is the stellar spot.

Appendix A

IRAF Parameters

A.1 Editing Image Header Parameters

Table A.1 shows an image header from an image taken with the 0.5m telescope located at the Ball Sate University Observatory. The telescope is fit with with a FLI PL16801 CCD camera. Images taken with different CCD cameras have different names for the parameters in the image headers. To add the parameter DATASEC with a value expression "[20:2065,12:2057]" to headers of all V-filter images in a directory, the command *eparam hedit* is entered at the command line prompt in IRAF. Table A.2 shows how to set the parameters in the hedit task. After the parameters are set, the task is executed with the colon command *:go*. To exit the parameter list without executing the task, the colon command *:quit* is used.

Parameter	Value	Definition
OBJECT	NSVS 7680691	Name of object observed
EXPTIME	6.00E+001	[sec] Duration of exposure
FILTER	Empty/R	Filter name
IMAGETYP	LIGHT	Type of image
OBSERVER	Gavel	Observer name
OBSERVAT	BSU	Observatory name

Table A.1: Sample from an image header. Image taken with FLI PL16801 CCD camera.

Image Reduction and Analysis Facility

Parameter	Value	Definition
images	VNSVS*fits	images to be edited
fields	DATASEC	fields to be edited
value	[20:2065,12:2057]	value expression
add	yes	add rather than edit fields
addonly	no	add only if field does not exist
delete	no	delete rather than edit fields
verify	no	verify each edit operation
show	yes	print record of each edit operation
update	yes	enable updating of the image header
mode	ql	

Table A.2: Parameter list to add the parameter DATASEC with its measured value to V-bandpass image headers. PACKAGE=imutil, TASK=hedit

A.2 Setting the Instrument

There are a few tasks to complete in IRAF before starting the reduction and photometry processes. Instrumentation files specific to the CCD imaging camera and the geometric location of the Ball State University Observatory (BSUO) must be placed in the IRAF Instrument Directory *ccddb$*. Dimensions of the data section (and bias section for 0.5m telescope data) are measured. Also, measured values pertaining to the CCD imaging camera such as read noise and gain must be specified. For each telescope-CCD combination at BSUO, there is a *cl* script saved in a file. The script is a list of commands that set selected parameters in IRAF upon startup. Each script calls upon two other files in the instument directory. One of the files is the BSUO subsets file. It assigns string variables used by the CCD imaging cameras to specify particular bandpass filters to the corresponding string variables used by IRAF. The other file called by the script is the data file for the CCD camera. Like the subsets file, it assigns string variables used by the CCD camera to the corresponding string variables used by IRAF. Table A.3 shows how to set the parameters in the setinstrument task for images taken with the 0.4m telescope. Executing the setinstrument task displays the parameter list for the ccdred task. The parameters of the ccdred task are not edited, the task is executed with the colon command, *:go*. This will display the parameter list for

the ccdproc task. At this point, the calibration frames can be generated.

Image Reduction and Analysis Facility

Parameter	Value	Definition
instrume	st-6303e	Instrument ID (type ? for a list)
site	BSUO	Site ID
directo	ccddb$	Instrument directory
review	yes	Review instrument parameters?
query	q	Instrument ID (type q to quit)
mode	ql	

Table A.3: PACKAGE=ccdred, TASK=setinstrument

A.3 Reduction

Parameters in ccdproc are split into four sections. The first section includes the images and ccdtype parameters and is shown in Table A.4. The second section includes the parameters that determine what corrections will be done to the specified images and is shown in Table A.5. The calibration frames used to make the corrections are specified in the third section of ccdproc. It is shown in Table A.6. The last section is used to interactivlely fit a function to the overscan strip. Table A.7 shows the parameters. After a cubic spline function has been fit to the overscan, the interactive mode is deactivated by setting interac = no. Parameters in ccdproc are edited before each step in the reduction process. The remaing tables in Appendix A.3 show what parameters are edited. Otherwise, the parameters keep the values shown in Table A.4, Table A.5, Table A.6 and Table A.7. Table A.8 shows how to set parameters in ccdproc before using zerocombine. Table A.9 shows how to set parameters in ccdproc before using darkcombine. Table A.10 shows how to set parameters in ccdproc before using flatcombine. Once the calibration frames have been created, ccdproc is used to apply corrections to the object images. Table A.11 shows how to set the parameters in ccdproc to process object images. To see what operations have been done to an image use the ccdlist task. At the command line prompt in IRAF, enter

```
ccdred> ccdlist *.fits | page
```

to see what processes have been done to each fits file in the directory.

Image Reduction and Analysis Facility

Parameter	Value	Definition
images	Bias*fts	List of CCD images to be correct
output		List of output CCD images
ccdtype	zero	CCD image type to correct
max cac	0	Maximum image caching memory (in Mbytes)
noproc	no	List processing steps only?

Table A.4: Parameter list (section 1 of 4). Parameters are set to fit a cubic spline function to the overscan data. Not all parameters are assigned values. PACKAGE=ccdred, TASK=ccdproc

Image Reduction and Analysis Facility

Parameter	Value	Definition
fixpix	no	Fix bad CCD lines and columns?
oversca	yes	Apply overscan strip correction?
trim	yes	Trim the image?
zerocor	no	Apply zero level correction?
darkcor	no	Apply dark count correction?
flatcor	no	Apply flat field correction?
illumco	no	Apply illumination correction?
fringec	no	Apply fringe correction?
readcor	no	Convert zero level image to readout correction?
scancor	no	Convert flat field image to scan correction?

Table A.5: Parameter list (section 2 of 4). Parameters are set to fit a cubic spline function to the overscan data. PACKAGE=ccdred, TASK=ccdproc

A.4 Measuring FWHM

The psfmeasure task is particularlly useful. It has the ability to automatically load images from a list one by one into the display window using one-letter keyboard commands. Table A.12 shows how to set task parameters for measuring the FWHM of the binary star

Image Reduction and Analysis Facility

Parameter	Value	Definition
readaxi	column	Read out axis (column|line)
fixfile		File describing the bad lines and columns
biassec	BIASSEC	Overscan strip image section
trimsec	DATASEC	Trim data section
zero		Zero level calibration image
dark		Dark count calibration image
flat		Flat field images
illum		Illumination correction images
fringe		Fringe correction images
minrepl	1.	Minimum flat field value
scantyp	shortscan	Scan type (shortscan|longscan)
nscan	1	Number of short scan lines

Table A.6: Parameter list (section 3 of 4). Parameters are set to fit a cubic spline function to the overscan data. Not all parameters are assigned values. PACKAGE=ccdred, TASK=ccdproc

Image Reduction and Analysis Facility

Parameter	Value	Definition
interac	yes	Fit overscan interactively?
functio	spline3	Fitting function
order	8	Number of polynomial terms or spline pieces
sample	*	Sample points to fit
naverag	1	Number of sample points to combine
niterat	1	Number of rejection iterations
low rej	3.	Low sigma rejection factor
high re	3.	High sigma rejection factor
grow	0.	Rejection growing radius
mode	ql	

Table A.7: Parameter list (section 4 of 4). Parameters are set to fit a cubic spline function to the overscan data. The number of spline pieces (order number) has been saved in the order parameter. PACKAGE=ccdred, TASK=ccdproc

Image Reduction and Analysis Facility

Parameter	Value	Definition
images	Bias*fts	List of CCD images to be correct
ccdtype	zero	CCD image type to correct
interac	no	Fit overscan interactively?

Table A.8: Parameter list before using zerocombine. PACKAGE=ccdred, TASK=ccdproc

Image Reduction and Analysis Facility

Parameter	Value	Definition
images	Dark*fts	List of CCD images to be correct
ccdtype	dark	CCD image type to correct
zerocor	yes	Apply zero level correction?
zero	Zero	Zero level calibration image
interac	no	Fit overscan interactively?

Table A.9: Parameter list before using darkcombine. PACKAGE=ccdred, TASK=ccdproc

Image Reduction and Analysis Facility

Parameter	Value	Definition
images	Flat*fts	List of CCD images to be correct
ccdtype	flat	CCD image type to correct
zerocor	yes	Apply zero level correction?
darkcor	yes	Apply dark count correction?
zero	Zero	Zero level calibration image
dark	Dark	Dark count calibration image
interac	no	Fit overscan interactively?

Table A.10: Parameter list before using flatcombine. PACKAGE=ccdred, TASK=ccdproc

Image Reduction and Analysis Facility

Parameter	Value	Definition
images	*NSVS*fts	List of CCD images to be correct
ccdtype	object	CCD image type to correct
zerocor	yes	Apply zero level correction?
darkcor	yes	Apply dark count correction?
flatcor	yes	Apply flat field correction?
zero	Zero	Zero level calibration image
dark	Dark	Dark count calibration image
flat	FlatB,FlatV,FlatR	Flat field images
interac	no	Fit overscan interactively?

Table A.11: Parameter list before processing object images. PACKAGE=ccdred, TASK=ccdproc

in every image in a directory. The image cursor input is a file named radec.coo that contains the right assention and declination of the binary star along with appropriate keyboard commands. The results are written to the Logfile. If the image cursor input parameter is left blank, the task will display one image (coords=MARK1) or each image in a list (coords=MARKALL) expecting the user to indicate star positions on the image(s) with the image cursor.

Image Reduction and Analysis Facility

Parameter	Value	Definition
images	*fits	List of Images
coords		Object coordinates
wcs	world	Coordinate system
display	no	Display images?
frame	1	Display frame to use
level	0.5	Measurement level
size	FWHM	Size to display
beta	INDEF	Moffat beta parameter
scale	1	Pixel scale
radius	5	Measurement radius (pixels)
sbuffer	5	Sky buffer (pixels)
dswidth	5	Sky width (pixels)
saturat	INDEF	Saturation level
ignore	no	Ignore objects with saturated pixels?
iterati	3	Number of radius adjustment iterations
xcenter	INDEF	X field center (pixels)
ycenter	INDEF	Y field center (pixels)
logfile	fwhm	Logfile
imagecu	radec.coo	Image cursor input
graphcu		Graphics cursor input
mode	q1	

Table A.12: Parameter list before measuring the FWHM of the binary star in every image in a list. PACKAGE=obsutil, TASK=psfmeasure

A.5 Rectifying Images

I followed documentation (Wells 1994) on general image processing found on the NOAO website. The imcentroid task will calculate x-shifts and y-shifts but it will fail if the

shifts are too large (as mine were). To overcome this, I had to supply the task with a file containing course x-shifts and y-shifts for each image. To create this file, I wrote a Python program called *shifts.py*. The input values for this program are taken from the first image in a batch, the last image in a batch and a few images in between. I call these images samples. The x and y coordinates of the same reference star in each of the samples is entered into the program. The first image in the batch is used as the reference image, its x-shift and y-shift are set to zero. The x-shifts and y-shifts for the other samples can be directly calculated from the inputed coordinate values of the reference star in those images. X-shifts and y-shifts for images that were taken in between the samples are estimated by linear interpolation. The shifts calculated by the imcentroid task are given to the imshift task. This task creates copies of each image, but each copy is shifted by a number of pixels in x and y. If the imshift task is successful, a star on one shifted image will have the same x and y location in all other shifted images. Thus, one coordinate file can be used for all images in the same observation night.

A.6 Creating a coordinate file

A coordinate file to be used by phot in batch mode is created with the rimcursor task. It works with an image that is displayed with XImtool. When the rimcursor task is executed, it waits for the user to activate (click on) the image display window. After activation, depressing any key on the keyboard will cause x and y coordinates to be read by the standard image cursor. Normally, the coordinates are read from the location of the image display cursor and then displayed in the terminal in a format chosen by the user. If the output coordinate system is set to world, the rimcursor task prints the Right Ascension and Declination of the location. To have the rimcursor task write the world coordinates (Right Ascension and Declination) to a coordinate file, the > character is used. To write a coordinate file named *radec.coo*, using the image named *image.fts*, the following command

is entered at the command prompt:

```
apphot> rimcursor image.fts wcs=world > radec.coo
```

The help page for the rimcursor task shows similar examples. To exit the rimcursor task, use CTRL-z. My technique is to execute the `center` task interactively on an image before using that image to create a coordinate file with rimcursor. The center task calculates accurate centers for the photometry stars in the image. In interactive mode, the center task also works with an image displayed with XImtool. The user moves the image cursor to a star and when the space-bar is depressed, x and y coordinates are read from the image cursor and displayed in the terminal. The advantage is that the calculated x-center and y-center for the star are also displayed. After the x-center and y-center of each photometry star is displayed, I set the IRAF environment variable *stdimcur* to *text* by entering the following command:

```
apphot> set stdimcur = text
```

This sets the standard image cursor to read from the keyboard instead of the image display. When I run rimcursor, I enter the calculated x-center and y-center of each photometry star using the keyboard and redirect the output to a coordinate file. This is much more precise than using the mouse to indicate star locations. Note, after making the coordinate file, make sure to set the image cursor input back to its default value.

A.7 Photometry

Table A.13 shows how to adjust the parameters in the datapars task before using the phot task in IRAF. Table A.14 shows how to set parameters in the phot task. The cl script I wrote to use with phot is shown in Table A.15. Phot.lis is a two column text file specifying the image name and the measured FWHM of the binary star in that image. The while loop cycles through each image in the list. For each image, the corresponding FWHM is used to

calculate five different apertures and one set of sky annuli. These values are imported to the phot task. It measures five different sets of values. A set is composed of instrumental magnitude and magnitude error measurements of the binary, comparison and check star extracted from each image. In the 1^{st} set, apertures are calculated as $1.5 \cdot FWHM$. In the 2^{nd} set, apertures are calculated as $1.6 \cdot FWHM$, etc. Only the data from the 5^{th} set kept for further analysis. While other sets have smaller magnitude errors, I assume the 5^{th} set is the most accurate. The variables, *list*, *s1* and x are declared by default in IRAF. All other variables must be declared as a float or string type variable before using the script.

Parameter	Value	Definition
scale	1.	Image scale in units per pixel
fwhmpsf	10.	FWHM of the PSF in scale units
emissio	yes	Features are positive ?
sigma	22.	Standard deviation of background in counts
datamin	INDEF	Minimum good data value
datamax	INDEF	Maximum good data value
noise	poisson	Noise model
ccdread	RDNOISE	CCD readout noise image header keyword
gain	EGAIN	CCD gain image header keyword
readnoi	10.	CCD readnoise in electrons
epadu	2.41	Gain in electrons per count
exposur	EXPTIME	Exposure time image header keyword
airmass		Airmass image header keyword
filter	FILTER	Filter image header keyword
obstime	HJD	Time of observation image header keyword
itime	50.	Exposure time
xairmas	INDEF	Airmass
ifilter	Empty/V	Filter
otime	2457495.89998131	Time of observation
mode	ql	

Table A.13: Parameters set for images taken with the 0.5m telescope. Several values listed for parameters such as readnoi, epadu and otime, are the data that was most recently pulled from the image header the last time the phot task was executed. The sigma parameter is set manually in the phot task, but it can also be set in datapars. PACKAGE=apphot, TASK=datapars

Parameter	Value	Definition
image	BNSVS*fts	The input image(s)
skyfile		The input sky file(s)
coords	radec.coo	The input coordinate files(s)
output	default	The output photometry file(s)
plotfil		The output plots metacode file
datapar		Data dependent parameters
centerp		Centering parameters
fitskyp		Sky fitting parameters
photpar		Photometry parameters
interac	no	Interactive mode ?
radplot	no	Plot the radial profiles in interactive mode ?
icomman		Image cursor: [x y wcs] key [cmd]
gcomman		Graphics cursor: [x y wcs] key [cmd]
wcsin	world	The input coordinate system
wcsout	wcsout	The output coordinate system
cache	cache	Cache the input image pixels in memory ?
verify	yes	Verify critical parameters...
update	update	Update critical parameters...
verbose	verbose	Print messages...
graphic	graphics	Graphics device
display		Display device
mode	ql	

Table A.14: Parameters are set to do photometry on all B filter images in a directory. The coordinate file created by the rimcursor task is *radec.coo*. The input coordinate system is set to world (Right Ascension-Declination). PACKAGE=apphot, TASK=phot

IRAF cl script for phot task

```
list = "phot.lis"
while (fscan (list, s1, x) !=EOF) {
    r1 = 1.5*x
    r2 = 1.6*x
    r3 = 1.7*x
    r4 = 1.8*x
    r5 = 2.0*x
    aps = r1//", "//r2//", "//r3//", "//r4//", "//r5
    a1 = 4.0*x
    a2 = 1.3*x
    phot (s1,
    "", coords="radec.coo", output="default", plotfile="", datapars="",
    centerpars="", fitskypars="", photpars="", interactive=no, radplots=yes,
    icommands="", gcommands="", wcsin="world", wcsout=")_.wcsout",
    cache=")_.cache", verify=no, update=")_.update", verbose=")_.verbose",
    graphics=")_.graphics", display="imdy", apertures=aps, annulus=a1,
    dannulus=a2)
}
```

Table A.15: The cl script calculates five photometry aperture radii and one set of sky annuli for each image based on the measured FWHM of the variable star in that image. The radii are merged into a single string variable before being passed to the phot task.

A.8 Processing magnitude files

The txconcat task combines all magnitude files of the same bandpass filter into the same file. The txdump task extracts data from this combined magnitude file. The data is extracted in a particular order so that it may be read by `process.py`, the Python program I wrote to caculate differential magnitudes and magnitude errors. An example of using the txdump task is shown below. Data in combined magnitude file B.mag.1 is collected then written to the ouput file, B.txt. The data is in four columns: HJD, magnitude, magnitude error and star identification. The task uses the boolean variable `expr` to filter what data is written to the output file. To extract only the data that have magnitude errors less than 0.01, I set the parameter `expr = merr<=0.01`.

```
ptools> txdump > B.txt
ptools> textfile = B.mag.1          # Combined magnitude file
ptools> fields = otime,mag,merr,id  # HJD, magnitude, error and star id
ptools> expr = merr<=0.01           # filter data by magnitude error
```

A.9 Period Analysis with pdm

The pdm task is used to quickly display a folded light curve and calculate the orbital period and ephemeris epoch. I do not keep these values, I use PERANSO to determine orbital periods. The parameter list for the pdm task is given below. The user chooses a time range in which to search by specifying the minimum period and maximum period. The user also specifies ntheta, the number of theta points in period window.

Image Reduction and Analysis Facility

Parameter	Value	Definition
infiles	B*txt	Input file template
metafil	pdmmeta	Metacode file
batchfi	pdmbatch	Batch text file
device	stdgraph	Graphics device
interac	yes	Use interactive graphics ?
flip	yes	Flip the y-axis ?
minp	0.23	Minimum period to search
maxp	0.33	Maximum period to search
ntheta	2000	Number of theta points in period window
pluspoi	50	Threshold number of data points...
autoran	no	Set ranges automatically
nsigma	3.	Number of standard deviations for autoranges
cursor		graphics cursor input
mode	ql	

Table A.16: PACKAGE=astutil, TASK=pdm

Bibliography

Aitken, R. G. 1918, *The Binary Stars*, (Douglas C. McMurtrie), New York.

Alton, K. B. 2016, *Journal of the American Association of Variable Star Observers (JAAVSO)*, **44**, 87.

Bradstreet, D. H. 2005, *Society for Astronomical Sciences Annual Symposium*, **24**, 23.

Carroll, B. W., and Ostlie, D. A. 2007, *An Introduction to Modern Astrophysics*, (Pearson Education).

CBA Belgium Observatory. 2011, PERANSO (v2.51) software, Flanders, Belgium (http://www.cbabelgium.com/).

Chang, S. W. and Byun, Y. I. and Hartman, J. D. 2015, *Astrophysical Journal*, **149**, 19.

Drake, A. J., *et al.* 2014, *The Astrophysical Journal Supplement Series*, **213**, 9.

Essam, A., and Nakhlawy, A., and Rassem, M. A. 2013, *NRIAG Journal of Astronomy and Geophysics*, **2**, 1-7.

Flower, P. J. 1996, *Astrophysical Journal*, **469**, 355.

Fitzgerald, M. P. 1970, *Astronomy and Astrophysics*, **4**, 234.

Fitzpatrick, E. L. 1999, *The Publications of the Astronomical Society of the Pacific*, **111**, 63-75.

Harmanec, P. 1988, *Bulletin of the Astronomical Institutes of Czechoslovakia*, **39**, 329-345.

Henden, A. A., and Kaitchuck, R. H. 1982, *Astronomical Photometry*, (Van Nostrand Reinhold Company).

Hoffman, D. I., Harrison, T. E., and McNamara, B. J. 2009, *The Astronomical Journal*, **138**, 466.

Howell S. B. 2006, *Handbook of CCD Astronomy*, (Cambridge University Press).

Høg, E., *et al.* 2000, *Astronomy and Astrophysics*, **355**, L27-L30.

Honeycutt, R. K. 1992, *Astronomical Society of the Pacific, Publications*, **104**, 435-440.

Hubscher, J. 2015, *Information Bulletin on Variable Stars: BAV-Results of observations*, **6152**, 10.

Janesick, J., and Blouke, M. 1987, *Sky and Telescope Magazine*, **74**, 238.

Kallrath J. and Milone E. F. 2009, *Eclipsing Binary Stars: Modeling and Analysis*, (Springer Science & Business Media).

Kopal, Z. 1943, *Proceedings of the American Philosophical Society*, **86**, 342-350.

Kwee, K. K., and van Woerden, H. 1956, *Bulletin of the Astronomical Institutes of the Netherlands*, **12**, 327.

Linnell, A. P. 1991, *Astrophysical Journal*, **383**, 330-335.

Lucy, L. B. 1968, *Astrophysical Journal*, **153**, 877.

Mallama, A. D. 1982, *International Amateur-Professional Photoelectric Photometry Communications*, **7**, 14.

O'Connell, D. J. K. 1951, *Publications of the Riverview College Observatory*, **2**, 85-100.

Plavec, M. 1968, *Advances in Astronomy and Astrophysics*, **6**, 201-278.

Prša, L. B., and Zwitter, T. 2005, *Astrophysical Journal*, **628**, 426.

Rucinski, S. M. 1969, *Acta Astronomica*, **19**, 245.

Rucinski, S. M., and Duerbeck, H. W. 1997, *Publications of the Astronomical Society of the Pacific*, **109**, 1340-1350.

Russell, H. N. 1946, *Popular Astronomy*, **54**, 162.

Reynolds, Mike D. 2005, *Binocular Stargazing*, (Stackpole Books).

Schlafly, E. F., and Finkbeiner, D. P. 2011, *Astrophysical Journal*, **737**, 103.

Schwarzenberg-Czerny, A. 1996, *Astrophysical Journal*, **460**, L107.

Stellingwerf, R. F. 1978, *Astrophysical Journal*, **224**, 953-960.

Terrell, D. 1992, *Binary Stars: a pictorial atlas*, (Malabar, Fla.: Krieger).

Tody, D. 1993, *Astronomical Data Analysis Software and Systems II*, **52**, 173.

Wilson, R. E., and Devinney, E. J. 1971, *Astrophysical Journal*, **166**, 605.

Winkler, L. 1967, *A new method for the determination of the epoch of minimum of binary star systems*, **72**, 226.

Woźniak, P. R., *et al.* 2004, *Astrophysical Journal*, **127**, 2436-2449.

van Hamme, W. 1993, *Astronomy Journal*, **106**, 2096.

Yuan, H. B., and Liu, X. W., and Xiang, M. S. 2013, *Monthly Notices of the Royal Astronomical Society*, **430**, 2188-2199.